Disorder-Enhanced Imaging with Spatially Controlled Light

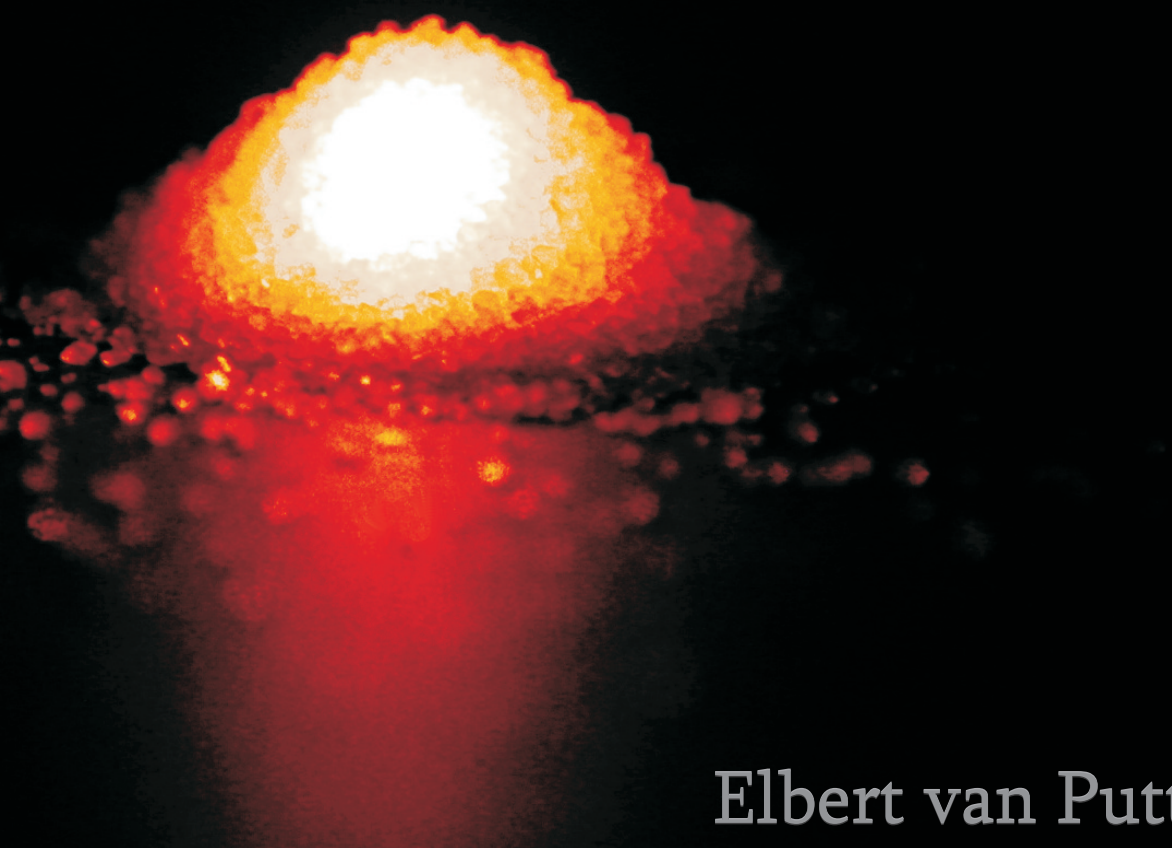

Elbert van Putten

DISORDER-ENHANCED IMAGING WITH SPATIALLY CONTROLLED LIGHT

Ongekend scherpe afbeeldingen door gecontroleerd verstrooid licht

Promotiecommissie

Promotores	Prof. Dr. A. Lagendijk Prof. Dr. A.P. Mosk
Overige leden	Prof. Dr. L. Kuipers Prof. Dr. C.W.J. Beenakker Prof. Dr. W.L. Vos Prof. Dr. V. Sandoghdar
Paranimfen	Drs. H. Vinke A.R. van der Velde, B.Sc.

The work described in this thesis is financially supported by the
'Nederlandse Organisatie voor Wetenschappelijk Onderzoek' (NWO).

It was carried out at the
Complex Photonic Systems Group,
Department of Science and Technology
and MESA+ Institute for Nanotechnology,
University of Twente, P.O. Box 217,
7500 AE Enschede, The Netherlands.

This thesis can be downloaded from
http://www.wavefrontshaping.com
ISBN: 978-90-365-3247-1

DISORDER-ENHANCED IMAGING WITH SPATIALLY CONTROLLED LIGHT

PROEFSCHRIFT

ter verkrijging van
de graad van doctor aan de Universiteit Twente,
op gezag van de rector magnificus,
prof. dr. H. Brinksma,
volgens besluit van het College voor Promoties
in het openbaar te verdedigen
op vrijdag 28 oktober 2011 om 16.45 uur

door

Eibert Gerjan van Putten

geboren op 16 november 1983
te Elburg

Dit proefschrift is goedgekeurd door:

Prof. Dr. A. Lagendijk en Prof. Dr. A.P. Mosk

Voor mijn ouders

"It turns out that an eerie type of chaos can lurk just behind a facade of order - and yet, deep inside the chaos lurks an even eerier type of order."

- Douglas R. Hofstadter

Contents

CHAPTER 1

Introduction

1.1 Optical imaging

The importance of light for mankind is reflected by the tremendous efforts to take control over its creation and propagation. Profiting from the interplay between light and matter, carefully designed optical elements, such as mirrors and lenses, have been successfully employed in the last centuries for light manipulation. Conventional macroscopic optics enable metrology with nanometric precision and communication across the world at light speed.

Perhaps the most vivid application of light is its use for optical imaging. The invention of the compound microscope by lens grinders Hans and Zacharias Janssen and later improvements by Hooke, Van Leeuwenhoek, and Abbe have revolutionized every aspect of science[1] by making microscopic objects visible that would normally be invisible for the naked eye. A second revolution in optical imaging came with the advent of digital imaging sensors, for which Boyle and Smith received the Nobel Prize in 2009. These sensors allow spatial optical information to be stored electronically and thereby completely transformed image processing. In modern society where we can digitize every moment of our life[1] with lens-based cameras that easily fit in our mobile phone, it is hard to imagine life without these groundbreaking inventions.

Despite their enormous advancements, conventional optical elements -no matter how well designed- can offer only a limited amount of control over light. In as early as 1873 Abbe[3] discovered that lens-based microscopes are unable to resolve structure smaller than half the light's wavelength. This restriction, commonly referred to as the diffraction limit, is due to the inability of conventional lenses to capture the exponentially decaying evanescent fields that carry the high spatial frequency information. For visible light, this limits the optical resolution to about 200 nm.

With fluorescence based imaging methods it is possible to reconstruct an image of objects that are a substantial factor smaller than the resolution by exploiting the photophysics of extrinsic fluorophores.[4–8] However, their resolution still strongly depends on the shape of the optical focus, which is determined by conventional lens systems and therefore subjected to the diffraction limit.

[1] See Ref. [2] for an extreme yet incredibly inspiring example of life digitization.

1.2 Nano-optics

Many of the limitations of conventional optics can be overcome by nano-optics[9]. In this field, nano structured optical elements are used to manipulate light on length scales that are much smaller than the optical wavelength. Analogies between the electromagnetic wave equation and the Schrödinger equation permit the field of nano-optics to profit from the rich field of mesoscopic electron physics [10, 11]. With the increasing accessibility of high quality nanoscience and nanotechnology, an incredible wide range of man-made nano elements have been fabricated ranging from high-Q cavities[12, 13] to optical nano antennas[14–16] and channel plasmon subwavelength waveguide components[17]. The advent of nano-optics thereby breached the way for exceptional experiments in emerging fields as plasmonics[18, 19], cavity optomechanics[20–23], and metamaterials[24–28].

Nano-optics is employed in different ways to improve the resolution in optical imaging. Near-field microscopes bring nano-sized scanning probes[29, 30], nano scatterers[31–33], or even antennas[34–36] in close proximity of an object to detect the exponentially decaying evanescent fields. These near field techniques enable unprecedented visualization of single molecules[37], propagation of light in photonic wave guides[38–40] as well as the magnetic part of optical fields[41].

Metamaterials, on the other hand, can be engineered to amplify evanescent waves rather than diminishing them. In 2000, Pendry predicted that such materials could form the perfect optical lens, not hindered by the diffraction limit.[42] A few years later several experimental demonstrations followed[43–45], showing exquisite images of nano sized objects.

1.3 Disorder to spoil the party?

All the aforementioned imaging techniques pose stringent quality restrictions on the optical components, as any deviation from the perfect structure will result in a deteriorated image. Especially in nano optics, where the components are strongly photonic and affect light propagation in an extreme way, structural imperfections are a huge nuisance[46, 47]. For that reason, meticulous manufacturing processes try to ensure quality perfection up to fractions of the optical wavelength.

Nevertheless, unavoidable fabrication imperfections cause disorder in optical components that affects the image quality. On top of that, disordered light scattering by the environment strongly limits imaging in turbid materials, such as biological tissue.[48, 49] Gated imaging methods, such as optical coherence tomography, quantum coherence tomography[50], time gated imaging[51], and polarization gated imaging[52] use the small amount of unscattered (ballistic) light to improve the imaging depth. As the fraction of ballistic light exponentially decreases with increasing depth, the use of these techniques is limited to a few mean free paths. Until very recently, optical imaging with scattered light seemed far out of reach.

First hints that scattering does not have to be detrimental came from the fields of acoustics and microwaves by the pioneering work done in the group of Fink,

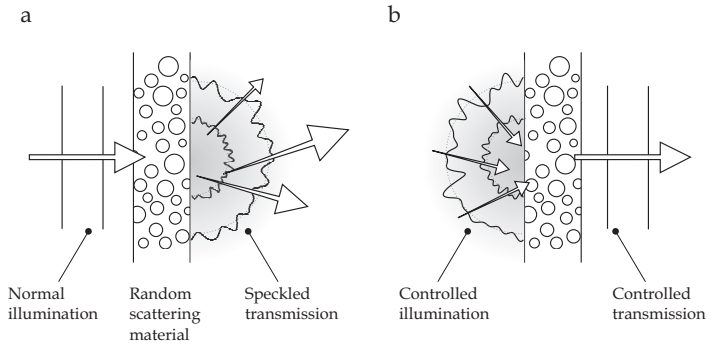

Figure 1.1: Principle of wave front shaping. **a:** A disordered scattering material scatters light into random directions thereby creating a random speckled transmission pattern under normal plane wave illumination. **b:** By illuminating the material by an especially designed wave front it is possible to control the light propagation and send light into a designated transmission direction.

where these classical waves shown to be a convenient testing ground of mesoscopic wave physics. By taking advantage of the time reversal invariance, they demonstrated that a pulse can be focussed back onto its source by reradiating a time reversed version of the scattered wave front.[53, 54] This powerful concept was used to focus waves through disordered barriers[55–57], increase the information density in communication[58–61], and even break the diffraction limit[61, 62] with the use of disordered scattering.

1.4 Controlled illumination for disordered nano-optics

In optics, the lack of adequate reversible sensor technology withholds the use of time reversal techniques. Nevertheless, it was shown in 2007 by Vellekoop and Mosk[63] that similar results can be obtained in the optical domain by combining spatial light modulators, which are computer controlled elements that control the phase in each pixel of a two-dimensional wave front, with algorithms[64] that measure the complex transfer function through disordered materials. This information was then used to control the propagation of scattered light by forming a complex wave front that, after being scattered, ends up in a single sharp focus[63, 65] (Fig. 1.1).

One of the big advantages of this approach, called wave front shaping, is that it does not require a source at the desired target point so that light could not only be focussed through but also deep inside a completely opaque material[66]. While the initial experiments required several minutes, impressive results by Cui[67] and Choi et al.[68] show that the measurement time can be pushed to well below one second, which is especially important for biomedical applications.

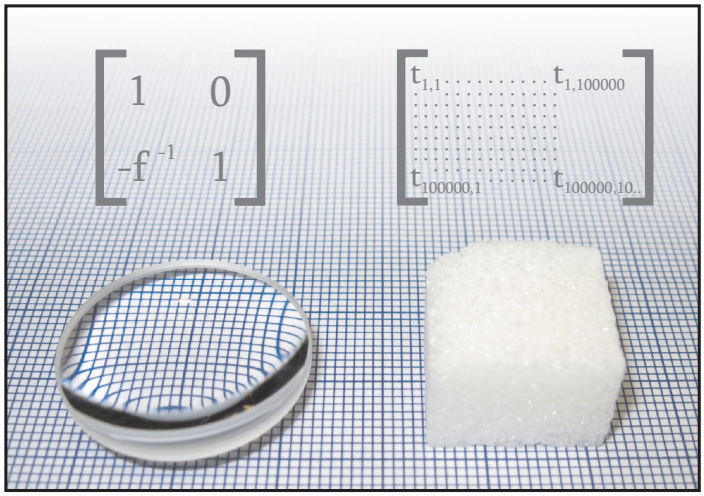

Figure 1.2: Two optical elements fully characterized by their transmission matrix, which relates the incident wave front to the transmitted one. In the case of a thin lens, the transformation of the wave front is described by a 2×2 matrix operating on a vector describing the wave front curvature[69]. For more complex elements such as a sugar cube the transmission matrix operates in a basis of transversal modes, which is very large. Full knowledge of the transmission matrix enables disordered materials to focus light as lenses.

By parallelizing the experiment of Vellekoop and Mosk, Popoff et al. extended wave front shaping to measure part of the complex transmission matrix[70]. In important earlier work, such a matrix was used to recover the polarization state of incident illumination.[71] Now, with knowledge of the transmission matrix, scattered light was focussed at several places and images were transmitted through opaque layers[68, 72]. When the information in the transmission matrix is fully known, any disordered system becomes a high-quality optical element (Fig. 1.2). From a technological point of view this has great promise: quite possibly disordered scattering materials will soon become the nano-optical elements of choice[73, 74]. With emerging applications in digital phase conjugation[75, 76], digital plasmonics[77], micromanipulation[78], and spatiotemporal control[79–81], wave front shaping is already causing a revolution in optics of scattering materials.

1.5 Outline of this thesis

In this thesis we pioneer the use of disordered nano-optical elements combined with controlled illumination for imaging purposes. With these 'scattering lenses' we achieve unprecedented resolutions and demonstrate imaging through opaque layers. Next to imaging, we also demonstrate the use of disordered nano-optics

for non-imaging displacement metrology.

In chapter 2 we introduce a framework of scattering and transmission matrices, show how spatial light control is used to measure elements of these matrices, and we study how this information can be used to control light propagation in disordered materials under experimental relevant conditions.

The fabrication and characterization of the disordered photonic structures we developed for our experiments are described in Chapter 3. First we discuss disordered zinc oxide samples that can be doped with fluorescent nano spheres. Then we detail the fabrication of high resolution scattering lenses out of gallium phosphide.

In chapter 4 we experimentally show that spatial wave front shaping can be used to focus and concentrate light to an optimal small spot *inside* a turbid material. Chapter 5 is dedicated to a non-imaging approach of displacement metrology for disordered materials that opens the way for high speed nanometer-scale position detection.

With scattering lenses made out of gallium phosphide it is possible to achieve sub-100 nm optical resolution at visible wavelengths using the high refractive index of the material; High Index Resolution Enhancement by Scattering (HIRES). In chapter 6 we combine such HIRES scattering lens with spatial wave front shaping to generate a small scanning spot with which we image gold nano spheres.

While the resolution of the HIRES scattering lens is very high, the obtained field of view is restricted by the optical memory effect to a few square micrometers. To use these scattering lens in wide field mode we developed a new imaging technique that exploits correlations in scattered light; Speckle Correlation Resolution Enhancement (SCORE). Chapter 7 starts with a theoretical consideration of SCORE supported by simulations. In the second part of that chapter we describe an experiment where SCORE is used to acquire high resolution wide field images of fluorescent nano spheres that reside in the object plane of a gallium phosphide scattering lens.

The developed imaging technique SCORE is more general applicable to scattering lenses. In chapter 8 we demonstrate that with a proof of principle of reference free imaging through opaque disordered materials. This technique promises to be of great relevance to biomedical imaging, transportation safety, and detection of concealed weapons.

Bibliography

[1] N. Zheludev, *What diffraction limit?*, Nat. Mater. **7**, 420 (2008). — p.11.

[2] D. Roy *et al.*, *The human speechome project*, Twenty-eighth Annual Meeting of the Cognitive Science Society (2006). — p.11.

[3] E. Abbe, *Beiträge zur theorie des mikroskops und der mikroskopischen wahrnehmung*, Archiv für Mikroskopische Anatomie **9**, 413 (1873), 10.1007/BF02956173. — p.11.

[4] S. W. Hell and J. Wichmann, *Breaking the diffraction resolution limit by stimulated emission: stimulated-emission-depletion fluorescence microscopy*, Opt. Lett. **19**, 780 (1994). — p.11.

[5] M. Dyba and S. W. Hell, *Focal spots of size λ/23 open up far-field florescence microscopy at 33 nm axial resolution*, Phys. Rev. Lett. **88**, 163901 (2002). — p.11.

[6] E. Betzig, G. H. Patterson, R. Sougrat, O. W. Lindwasser, S. Olenych, J. S. Bonifacino, M. W. Davidson, J. Lippincott-Schwartz, and H. F. Hess, *Imaging Intracellular Fluorescent Proteins at Nanometer Resolution*, Science **313**, 1642 (2006). — p.11.

[7] M. J. Rust, M. Bates, and X. Zhuang, *Sub-diffraction-limit imaging by stochastic optical reconstruction microscopy (storm)*, Nat. Meth. **3**, 793 (2006). — p.11.

[8] S. W. Hell, *Far-Field Optical Nanoscopy*, Science **316**, 1153 (2007). — p.11.

[9] L. Novotny and B. Hecht, *Principles of nano-optics* (Cambridge Univ. Press, Cambridge, U.K., 2006). — p.12.

[10] C. W. J. Beenakker, *Random-matrix theory of quantum transport*, Rev. Mod. Phys. **69**, 731 (1997). — p.12.

[11] E. Akkermans and G. Montambaux, *Mesoscopic physics of electrons and photons* (Cambridge Univ. Press, Cambridge, U.K., 2006). — p.12.

[12] D. K. Armani, T. J. Kippenberg, S. M. Spillane, and K. J. Vahala, *Ultra-high-q toroid microcavity on a chip*, Nature **421**, 925 (2003). — p.12.

[13] K. J. Vahala, *Optical microcavities*, Nature **424**, 839 (2003). — p.12.

[14] H. Gersen, M. F. García-Parajó, L. Novotny, J. A. Veerman, L. Kuipers, and N. F. van Hulst, *Influencing the angular emission of a single molecule*, Phys. Rev. Lett. **85**, 5312 (2000). — p.12.

[15] A. G. Curto, G. Volpe, T. H. Taminiau, M. P. Kreuzer, R. Quidant, and N. F. van Hulst, *Unidirectional emission of a quantum dot coupled to a nanoantenna*, Science **329**, 930 (2010). — p.12.

[16] L. Novotny and N. van Hulst, *Antennas for light*, Nat. Photon. **5**, 83 (2011). — p.12.

[17] S. I. Bozhevolnyi, V. S. Volkov, E. Devaux, J.-Y. Laluet, and T. W. Ebbesen, *Channel plasmon subwavelength waveguide components including interferometers and ring resonators*, Nature **440**, 508 (2006). — p.12.

[18] T. W. Ebbesen, H. J. Lezec, H. F. Ghaemi, T. Thio, and P. A. Wolff, *Extraordinary optical transmission through sub-wavelength hole arrays*, Nature **391**, 667 (1998). — p.12.

[19] W. L. Barnes, A. Dereux, and T. W. Ebbesen, *Surface plasmon subwavelength optics*, Nature **424**, 824 (2003). — p.12.

[20] S. Gigan, H. R. Bohm, M. Paternostro, F. Blaser, G. Langer, J. B. Hertzberg, K. C. Schwab, D. Bauerle, M. Aspelmeyer, and A. Zeilinger, *Self-cooling of a micromirror by radiation pressure*, Nature **444**, 67 (2006). — p.12.

[21] A. Schliesser, P. Del'Haye, N. Nooshi, K. J. Vahala, and T. J. Kippenberg, *Radiation pressure cooling of a micromechanical oscillator using dynamical backaction*, Phys. Rev. Lett. **97**, 243905 (2006). — p.12.

[22] T. J. Kippenberg and K. J. Vahala, *Cavity optomechanics: Back-action at the mesoscale*, Science **321**, 1172 (2008). — p.12.

[23] A. D. O´Connell *et al.*, *Quantum ground state and single-phonon control of a mechanical resonator*, Nature **464**, 697 (2010). — p.12.

[24] J. D. Joannopoulos, S. G. Johnson, J. N. Winn, and R. D. Meade, *Photonic crystals: Molding the flow of light* (Princeton University Press, 2008). — p.12.

[25] D. R. Smith, J. B. Pendry, and M. C. K. Wiltshire, *Metamaterials and negative refractive index*, Science **305**, 788 (2004). — p.12.

[26] U. Leonhardt, *Optical Conformal Mapping*, Science **312**, 1777 (2006). — p.12.

[27] J. B. Pendry, D. Schurig, and D. R. Smith, *Controlling Electromagnetic Fields*, Science **312**, 1780 (2006). — p.12.

[28] C. M. Soukoulis and M. Wegener, *Past achievements and future challenges in the development of three-dimensional photonic metamaterials*, Nat. Photon. **advance online publication**, (2011). — p.12.

[29] E. Betzig and J. K. Trautman, *Near-field optics: Microscopy, spectroscopy, and surface modification beyond the diffraction limit*, Science **257**, 189 (1992). — p.12.

[30] D. W. Pohl, *Optics at the nanometre scale*, Philosophical Transactions: Mathematical, Physical and Engineering Sciences **1817**, 701 (2004). — p.12.

[31] F. Zenhausern, Y. Martin, and H. K. Wickramasinghe, *Scanning interferometric apertureless microscopy: Optical imaging at 10 angstrom resolution*, Science **269**, 1083 (1995). — p.12.

[32] A. V. Zayats and V. Sandoghdar, *Apertureless near-field optical microscopy via local second-harmonic generation*, Journal of Microscopy **202**, 94 (2001). — p.12.

[33] Y. De Wilde, F. Formanek, R. Carminati, B. Gralak, P.-A. Lemoine, K. Joulain, J.-P. Mulet, Y. Chen, and J.-J. Greffet, *Thermal radiation scanning tunnelling microscopy*, Nature **444**, 740 (2006). — p.12.

[34] T. Kalkbrenner, U. Håkanson, A. Schädle, S. Burger, C. Henkel, and V. Sandoghdar, *Optical microscopy via spectral modifications of a nanoantenna*, Phys. Rev. Lett. **95**, 200801 (2005). — p.12.

[35] S. Kühn, U. Håkanson, L. Rogobete, and V. Sandoghdar, *Enhancement of single-molecule fluorescence using a gold nanoparticle as an optical nanoantenna*, Phys. Rev. Lett. **97**, 017402 (2006). — p.12.

[36] H. Eghlidi, K. G. Lee, X.-W. Chen, S. Gotzinger, and V. Sandoghdar, *Resolution and enhancement in nanoantenna-based fluorescence microscopy*, Nano Letters **9**, 4007 (2009), pMID: 19886647. — p.12.

[37] C. Hettich, C. Schmitt, J. Zitzmann, S. Kühn, I. Gerhardt, and V. Sandoghdar, *Nanometer resolution and coherent optical dipole coupling of two individual molecules*, Science **298**, 385 (2002). — p.12.

[38] M. L. M. Balistreri, H. Gersen, J. P. Korterik, L. Kuipers, and N. F. van Hulst, *Tracking femtosecond laser pulses in space and time*, Science **294**, 1080 (2001). — p.12.

[39] H. Gersen, T. J. Karle, R. J. P. Engelen, W. Bogaerts, J. P. Korterik, N. F. van Hulst, T. F. Krauss, and L. Kuipers, *Real-space observation of ultraslow light in photonic crystal waveguides*, Phys. Rev. Lett. **94**, 073903 (2005). — p.12.

[40] H. Gersen, T. J. Karle, R. J. P. Engelen, W. Bogaerts, J. P. Korterik, N. F. van Hulst, T. F. Krauss, and L. Kuipers, *Direct observation of bloch harmonics and negative phase velocity in photonic crystal waveguides*, Phys. Rev. Lett. **94**, 123901 (2005). — p.12.

[41] M. Burresi, D. van Oosten, T. Kampfrath, H. Schoenmaker, R. Heideman, A. Leinse, and L. Kuipers, *Probing the magnetic field of light at optical frequencies*, Science **326**, 550 (2009). — p.12.

[42] J. B. Pendry, *Negative refraction makes a perfect lens*, Phys. Rev. Lett. **85**, 3966 (2000). — p.12.

[43] R. J. Blaikie and D. O. S. Melville, *Imaging through planar silver lenses in the optical near field*, J. Opt. A **7**, s176 (2005). — p.12.

[44] N. Fang, H. Lee, C. Sun, and X. Zhang, *Sub-diffraction-limited optical imaging with a silver superlens*, Science **308**, 534 (2005). — p.12.

[45] Z. Liu, H. Lee, Y. Xiong, C. Sun, and X. Zhang, *Far-field optical hyperlens mag-*

nifying sub-diffraction-limited objects, Science **315**, 1686 (2007). — p.12.
[46] Y. A. Vlasov, V. N. Astratov, A. V. Baryshev, A. A. Kaplyanskii, O. Z. Karimov, and M. F. Limonov, *Manifestation of intrinsic defects in optical properties of self-organized opal photonic crystals*, Phys. Rev. E **61**, 5784 (2000). — p.12.
[47] A. Koenderink, A. Lagendijk, and W. Vos, *Optical extinction due to intrinsic structural variations of photonic crystals*, Phys. Rev. B **72**, (2005). — p.12.
[48] A. Ishimaru, *Limitation on image resolution imposed by a random medium*, Appl. Opt. **17**, 348 (1978). — p.12.
[49] P. Sebbah, *Waves and imaging through complex media* (Kluwer Academic Publishers, 1999). — p.12.
[50] M. B. Nasr, B. E. A. Saleh, A. V. Sergienko, and M. C. Teich, *Demonstration of dispersion-canceled quantum-optical coherence tomography*, Phys. Rev. Lett. **91**, 083601 (2003). — p.12.
[51] N. Abramson, *Light-in-flight recording by holography*, Opt. Lett. **3**, 121 (1978). — p.12.
[52] S. Mujumdar and H. Ramachandran, *Imaging through turbid media using polarization modulation: dependence on scattering anisotropy*, Optics Communications **241**, 1 (2004). — p.12.
[53] M. Fink, *Time reversed accoustics*, Phys. Today **50**, 34 (1997). — p.13.
[54] M. Fink, D. Cassereau, A. Derode, C. Prada, P. Roux, M. Tanter, J.-L. Thomas, and F. Wu, *Time-reversed acoustics*, Rep. Prog. Phys. **63**, 1933 (2000). — p.13.
[55] M. Fink, C. Prada, F. Wu, and D. Cassereau, *Self focusing in inhomogeneous media with time reversal acoustic mirrors*, IEEE Ultrason. Symp. Proc. **2**, 681 (1989). — p.13.
[56] C. Draeger and M. Fink, *One-channel time reversal of elastic waves in a chaotic 2d-silicon cavity*, Phys. Rev. Lett. **79**, 407 (1997). — p.13.
[57] G. Lerosey, J. de Rosny, A. Tourin, A. Derode, G. Montaldo, and M. Fink, *Time reversal of electromagnetic waves*, Phys. Rev. Lett. **92**, 193904 (2004). — p.13.
[58] S. H. Simon, A. L. Moustakas, M. Stoytchev, and H. Safar, *Communication in a disordered world*, Phys. Today **54**, 38 (2001). — p.13.
[59] A. Derode, A. Tourin, J. de Rosny, M. Tanter, S. Yon, and M. Fink, *Taking advantage of multiple scattering to communicate with time-reversal antennas*, Phys. Rev. Lett. **90**, 014301 (2003). — p.13.
[60] B. E. Henty and D. D. Stancil, *Multipath-enabled super-resolution for rf and microwave communication using phase-conjugate arrays*, Phys. Rev. Lett. **93**, 243904 (2004). — p.13.
[61] G. Lerosey, J. de Rosny, A. Tourin, and M. Fink, *Focusing beyond the diffraction limit with far-field time reversal*, Science **315**, 1120 (2007). — p.13.
[62] F. Lemoult, G. Lerosey, J. de Rosny, and M. Fink, *Resonant metalenses for breaking the diffraction barrier*, Phys. Rev. Lett. **104**, 203901 (2010). — p.13.
[63] I. M. Vellekoop and A. P. Mosk, *Focusing coherent light through opaque strongly scattering media*, Opt. Lett. **32**, 2309 (2007). — p.13.
[64] I. M. Vellekoop and A. P. Mosk, *Phase control algorithms for focusing light through turbid media*, Opt. Comm. **281**, 3071 (2008). — p.13.
[65] I. M. Vellekoop, A. Lagendijk, and A. P. Mosk, *Exploiting disorder for perfect focusing*, Nat. Photon. **4**, 320 (2010). — p.13.
[66] I. M. Vellekoop, E. G. van Putten, A. Lagendijk, and A. P. Mosk, *Demixing light paths inside disordered metamaterials*, Opt. Express **16**, 67 (2008). — p.13.
[67] M. Cui, *A high speed wavefront determination method based on spatial frequency modulations for focusing light through random scattering media*, Opt. Express **19**,

2989 (2011). — p.13.

[68] Y. Choi, T. D. Yang, C. Fang-Yen, P. Kang, K. J. Lee, R. R. Dasari, M. S. Feld, and W. Choi, *Overcoming the diffraction limit using multiple light scattering in a highly disordered medium*, Phys. Rev. Lett. **107**, 023902 (2011). — p.13, 14.

[69] H. Kogelnik and T. Li, *Laser beams and resonators*, Proc. IEEE **54**, 1312 (1966). — p.14.

[70] S. M. Popoff, G. Lerosey, R. Carminati, M. Fink, A. C. Boccara, and S. Gigan, *Measuring the transmission matrix in optics: An approach to the study and control of light propagation in disordered media*, Phys. Rev. Lett. **104**, 100601 (2010). — p.14.

[71] T. Kohlgraf-Owens and A. Dogariu, *Finding the field transfer matrix of scattering media*, Opt. Express **16**, 13225 (2008). — p.14.

[72] S. Popoff, G. Lerosey, M. Fink, A. C. Boccara, and S. Gigan, *Image transmission through an opaque material*, Nat. Commun. **1**, 81 (2010). — p.14.

[73] I. Freund, *Looking through walls and around corners*, Physica A: Statistical Mechanics and its Applications **168**, 49 (1990). — p.14.

[74] E. G. van Putten and A. P. Mosk, *The information age in optics: Measuring the transmission matrix*, Physics **3**, 22 (2010). — p.14.

[75] M. Cui and C. Yang, *Implementation of a digital optical phase conjugation system and its application to study the robustness of turbidity suppression by phase conjugation*, Opt. Express **18**, 3444 (2010). — p.14.

[76] C.-L. Hsieh, Y. Pu, R. Grange, and D. Psaltis, *Digital phase conjugation of second harmonic radiation emitted by nanoparticles in turbid media*, Opt. Express **18**, 12283 (2010). — p.14.

[77] B. Gjonaj, J. Aulbach, P. M. Johnson, A. P. Mosk, L. Kuipers, and A. Lagendijk, *Active spatial control of plasmonic fields*, Nat. Photon. **5**, 360 (2011). — p.14.

[78] T. Čižmár, M. Mazilu, and K. Dholakia, *In situ wavefront correction and its application to micromanipulation*, Nat. Photon. **4**, 388 (2010). — p.14.

[79] J. Aulbach, B. Gjonaj, P. M. Johnson, A. P. Mosk, and A. Lagendijk, *Control of light transmission through opaque scattering media in space and time*, Phys. Rev. Lett. **106**, 103901 (2011). — p.14.

[80] O. Katz, E. Small, Y. Bromberg, and Y. Silberberg, *Focusing and compression of ultrashort pulses through scattering media*, Nat. Photon. **5**, 372 (2011). — p.14.

[81] D. J. McCabe, A. Tajalli, D. R. Austin, P. Bondareff, I. A. Walmsley, S. Gigan, and B. Chatel, *Spatio-temporal focussing of an ultrafast pulse through a multiply scattering medium*, Nat. Commun. **2**, 447 (2011). — p.14.

CHAPTER 2

Control over Light Transport in Disordered Structures

2.1 Introduction

When light impinges onto disordered materials such as white paint, sea coral, and skin, microscopic particles strongly scatter light into random directions. Even though waves seemingly lose all correlation while propagating through such materials, elastic scattering preserves coherence and even after thousands of scattering events light still interferes. This interference manifests itself in spatiotemporal intensity fluctuations and gives rise to fascinating mesoscopic phenomena, such as universal conductance fluctuations[1, 2], enhanced backscattering[3, 4], and Anderson localization [5–9]. Since waves do not lose their coherence properties, the transport of light through a disordered material is not dissipative, but is coherent, with a high information capacity[10].

In a visionary work of Freund[11] from 1990 it was acknowledged for the first time that the information in multiple scattered light could potentially be used for high-precision optical instruments. For that, one would need to find the complex transfer function connecting the incident to the transmitted optical field. For materials of finite size under finite illumination this transfer function can be discretized and written as a matrix know as the optical transmission matrix.

In this chapter we introduce a framework of scattering and transmission matrices that we use to describe light transport in disordered structures. We show that with knowledge of the transmission matrix it is possible to control light propagation by spatially modulating the incident wave front. The influence of inevitable modulation errors on the amount of light control is theoretically analyzed for experimentally relevant situations. Then we study the important case of light control in which light is concentrated into a single scattering channel. The last part of this chapter is dedicated to angular positioning of scattered light by means of the optical memory effect.

The work in this chapter is partially based on and inspired by the review by Beenakker[12], the book by Akkermans and Montambaux[13], and the Ph.D. thesis of Vellekoop[14].

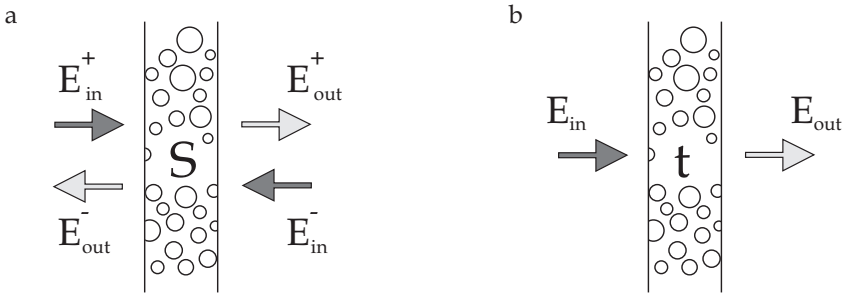

Figure 2.1: Schematic of light scattering in a random disordered slab. **a:** Incident electric fields are coupled to outgoing electric fields by the scattering in the slab. This coupling is described by the scattering matrix S. **b:** In a transmission experiment we illuminate the slab from one side and detect the transmission on the other side. For this process we only have to consider the transmission matrix t.

2.2 Scattering and Transmission Matrix

A propagating monochromatic light wave is characterized by the shape of its wave front. The wave front is a two dimensional surface that connects different positions of the wave that have an equal phase. In free space, any arbitrary wave front can be described by a linear combination of an infinite amount of plane waves. In a sample of finite size, only a limited number of propagating optical modes are supported. It is therefore possible to decomposed a wave impinging onto such a sample into a finite set of $2N$ orthogonal modes that completely describe the wave propagation. These propagating modes are defined as the scattering channels of the sample. We use a basis of these orthogonal channels to write a scattering matrix S that describes the coupling between propagating incident and outgoing waves, E_{in} and E_{out} respectively

$$E_{\text{out}} = SE_{\text{in}}. \tag{2.1}$$

In a sample with a slab geometry, as depicted in Fig. 2.1, where the width and height of the sample are much larger than its thickness, we have to consider only scattering channels on the left and the right side of the sample. For this geometry, the scattering matrix has a block structure describing the outgoing wave in term of the reflection r and transmission t of the incident wave

$$E_{\text{out}} = \begin{bmatrix} r^{-+} & t^{--} \\ t^{++} & r^{+-} \end{bmatrix} E_{\text{in}}. \tag{2.2}$$

Here the $-$ and $+$ reflect the propagation directions left and right respectively.

We now consider a transmission experiment with a one sided illumination from the left, as depicted in Fig. 2.1b. Under this condition we only have to take t^{++} into account, for which we now use the shorthand notation t. This matrix t is known as the optical transmission matrix and consist of NxN complex numbers.

A wave incident on the sample is then written as a vector of N coefficients

$$E_{\text{in}} \equiv (E_1, E_2, \ldots, E_N)\,. \tag{2.3}$$

When we use the subscripts a and b to refer to the channels on the left and right side of the sample respectively, the coefficients E_b of the transmitted wave E_{out} are conveniently written in terms of the matrix elements t_{ba} and the coefficients E_a of the incident wave E_{in} as

$$E_b = \sum_{a=1}^{N} t_{ba} E_a. \tag{2.4}$$

The coefficients E_a represent the modes of the light field coupled to the sample. Hence, the total intensity that impinges onto the sample is

$$I_{\text{in}} = \|E_{\text{in}}\|^2 = \sum_{a=1}^{N} |E_a|^2\,, \tag{2.5}$$

where the double bars denote the norm of the vector E_{in}.

The dimensionality of the transmission matrix is determined by the number of modes of the incident (and transmitted) light field coupled to the sample. This number of modes N is given by the amount of independent diffraction limited spots that fit in the illuminated surface area A

$$N = C\frac{2\pi A}{\lambda^2}. \tag{2.6}$$

where the factor 2 accounts for two orthogonal polarizations and C is a geometrical factor in the order of one. Hence, a 1-mm^2 sample supports about a million transverse optical modes.

Theoretical studies usually employ random matrix theory (RMT) to handle the enormous amount of data governed by the transmission matrix. RMT is a powerful mathematical approach that has been proven to be very successful in a many branches of physics and mathematics ranging from its starting point in nuclear physics[15] to wave transport in disordered structures[12][1]. The basic assumption underlying RMT is that due to the complexity of the system it can be described by a Hamiltonian composed out of completely random elements. It is then possible to infer statistical transport properties by concentrating on symmetries and conservation laws of the system. For example, the transmission matrix elements are correlated due to the fact that none of the matrix elements or singular values can ever be larger than unity, since in that case more than 100% of the incident power would be transmitted[17]. Another constraint on the matrix elements is imposed by time-reversal symmetry of the wave equations. However, such correlations are subtle and can only be observed if a large fraction of the transmission matrix elements is taken into account.

[1] For an introduction to random matrix theory see Ref. [16] and references therein

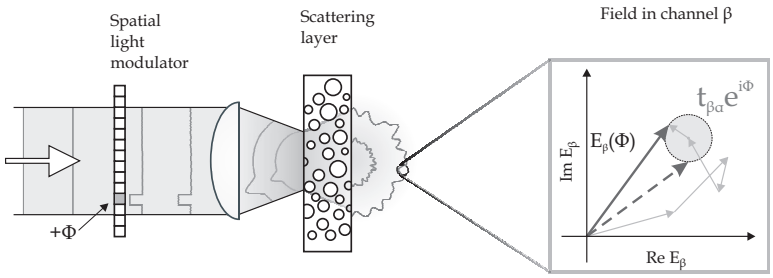

Figure 2.2: Method to measure transmission matrix element $t_{\beta\alpha}$. A spatial light modulator adds a phase Φ to the incident channel α. The modulated part of the wave front interferes with the unmodulated part thereby changing the field in scattering channel β. From a measurement of the intensity in β as function of Φ we can directly infer $t_{\beta\alpha}$ up to a constant phase offset ϕ_β.

2.3 Measuring Transmission Matrix Elements

The transmission matrix has played a less important role in experiments due to its enormously high dimensionality. Until recently it was beyond technological capabilities to measure a matrix with the corresponding large number of elements. Progress in digital imaging technology has now enabled measuring and handling such large amounts of data[18, 19]. In particular, spatial light modulators, which are computer-controlled elements that control the phase and amplitude in each pixel of a two-dimensional wave front, can be used to carefully shape light beams that reflect from it.

To see how such modulation of the light field can be used to measure the transmission matrix we write the field in a transmitted scattering channel $b = \beta$ in terms of the matrix elements $t_{\beta a}$ and the coefficients of the incident field E_a

$$E_\beta = \sum_{a=1}^{N} t_{\beta a} E_a. \tag{2.7}$$

When the incident light intensity I_{in} is equally distribute over all N incident channels, only the phase ϕ_a of E_a remains inside the summation

$$E_\beta = \sqrt{\frac{I_{\text{in}}}{N}} \sum_{a=1}^{N} t_{\beta a} e^{i\phi_a}. \tag{2.8}$$

By modulating the incident field we can change the individual phases ϕ_a. This modulation, together with a measurement of $|E_\beta|^2$, facilitates a evaluation of the individual matrix elements $t_{\beta a}$.

The method to measure transmission matrix element $t_{\beta\alpha}$ is depicted in Fig. 2.2. One pixel of the wave front, corresponding to incident channel $a = \alpha$, is modulated by a spatial light modulator before the light is projected onto the scattering

slab. This modulation changes the field in scattering channel β in a way that is proportional to $t_{\beta\alpha}$. More specifically, by adding a relative phase Φ to channel α the intensity in channel β changes to

$$I_\beta^\alpha(\Phi) = \frac{I_{\text{in}}}{N}\left|\sum_{a\neq\alpha}^{N-1} t_{\beta a} + t_{\beta\alpha}e^{i\Phi}\right|^2, \tag{2.9}$$

which is the result of an interference between the modulated channel α and a reference field created by all remaining unmodulated channels

$$E_{\beta,\text{ref}}^\alpha = \sqrt{\frac{I_{\text{in}}}{N}}\sum_{a\neq\alpha}^{N-1} t_{\beta a} \tag{2.10}$$

For large values of N, the single modulated channel has a negligible effect on the reference field in β. This reference field can therefore be considered constant for all $\alpha \in a$ so that

$$E_{\beta,\text{ref}}^\alpha \approx E_{\beta,\text{ref}} = \sqrt{\frac{I_{\text{in}}}{N}}\sum_{a=1}^{N} t_{\beta a} = \sqrt{I_\beta}e^{i\phi_\beta}, \tag{2.11}$$

where ϕ_β is the resulting phase of the reference field. Please note that reference field still fluctuates heavily between different transmitting channels.

Under the assumption of large N, the intensity in channel β is now written as

$$I_\beta^\alpha(\Phi) = I_\beta + |t_{\beta\alpha}|\sqrt{\frac{I_\beta I_{\text{in}}}{N}}\cos\left(\phi_\beta + \arg\left(t_{\beta\alpha}\right) - \Phi\right), \tag{2.12}$$

which is a sinosodual function with an amplitude proportional to $|t_{\beta\alpha}|$ and a relative phase shift $\arg\left(t_{\beta\alpha}\right)$. By measuring $I_\beta^\alpha(\Phi)$ for several values of Φ and fitting the result with a cosine function, the complex value of $t_{\beta\alpha}$ can be extracted up to a constant phase and amplitude offset. This measuring approach is easily extended with parallel detection of multiple channels b, using e.g. a CCD-camera, to measure multiple elements simultaneously.[19]

The expected intensity modulation in the modulation scheme outline in this section scales with $1/\sqrt{N}$. Under experimental conditions, where measurement noise becomes important, it might be worthwhile to work in a basis different from the canonical one, such as the Hadamard basis[19] or a completely random basis[20]. As more channels are modulated simultaneously, the resulting signal to noise ratio will improve.

2.4 Experimentally controlling light transport

The coherent relation between incident and transmitted light, as described by the transmission matrix t, opens opportunities to control light propagation in disordered structures. Knowledge of the transmission matrix, or a subset of it,

allows one to manipulate the incident light in order to steer the transmitted light in a predictable way.

To exploit the obtained information of the transmission matrix, we need to spatially modulate the wave front of the incident light. In an experimental environment, the generated wave front always deviate from its theoretically perfect counterpart. Here we will study the effect of experimental imperfections in the wave front on the control of light propagation. The results we obtain here are generally valid for wave front modulation techniques such as (digital) phase conjunction[21–23], holography[24, 25], and digital plasmonics[26].

In order to quantify the imperfections in modulation we calculate the normalized overlap of the experimentally realized field E with the desired field $\widetilde{E}$

$$\gamma \equiv \frac{\sum_{a=1}^{N} \widetilde{E}_a E_a^*}{\sqrt{\widetilde{I}_{\mathrm{in}} I_{\mathrm{in}}}}, \tag{2.13}$$

where the star denotes the complex conjugate and the tilde symbolizes the relation to the desired field. The parameter γ represents the quality of the modulation and its value ranges between 0 and 1. For a perfect modulation γ is equal to 1, while every imperfection inevitably reduces the value of γ. The parameter γ enables us to write the synthesized field as

$$E_a = \gamma \widetilde{E}_a + \sqrt{1 - |\gamma|^2}\, \Delta E_a, \tag{2.14}$$

where ΔE_a is an error term that is by definition orthogonal to $\widetilde{E}_a$.

We can identify several independent experimental factors that influence the quality of the wave front

$$|\gamma|^2 = |\gamma_{\mathrm{c}}|^2 \, |\gamma_{\mathrm{t}}|^2 \, |\gamma_{\mathrm{e}}|^2 \, . \tag{2.15}$$

First there is the amount of spatial control over the wave front that determines how many incident channels can be controlled independently (γ_{c}). Then there is temporal decoherence due to sample dynamics that change the transmission matrix in time (γ_{t}). The last factor consist of phase and amplitude modulation errors, which are either originating from the measurement of the matrix elements or introduced during the creation of the wave front (γ_{e}).

Besides these unintentional limitations, one might also deliberately choose to restrict the modulation to, e.g., phase or amplitude only. Although these two limitations can be seen as special cases of phase and/or amplitude errors, we will consider them separately due to their great experimental relevance.

2.4.1 Limited control

While an ideal wave front controls all incident channels individually, experimental conditions often limit the amount of available degrees of freedom in a synthesized wave front. Examples of such restrictions are the numerical aperture of the illumination optics or the amount of independent pixels in the wave front

synthesizer. As a result the N_s available degrees of freedom s of the wave front can only address a fraction N_s/N of the total amount of scattering channels.

To find the influence of a limited amount of control in the wave front on $\left\langle |\gamma|^2 \right\rangle$ we first define a set $\{a_s\}$ that contains all the N_s channels we can control. Because we have perfect control over the channels in $\{a_s\}$ and do not address the remaining ones we have

$$E_a = \begin{cases} \widetilde{E}_a & \text{if } a \in \{a_s\} \\ 0 & \text{otherwise.} \end{cases}$$

When these conditions are substituted into Eq. 2.13 we find

$$\gamma = \frac{1}{\sqrt{\widetilde{I}_{\text{in}} I_{\text{in}}}} \sum_{a \in \{a_s\}}^{N_s} \left| \widetilde{E}_a \right|^2 = \sqrt{\frac{I_{\text{in}}}{\widetilde{I}_{\text{in}}}} \tag{2.16}$$

To calculate $\left\langle |\gamma|^2 \right\rangle$ we only have to assume that there is no correlation between the illuminated channels and the transmission matrix elements, which is true as long as we do not selectively block certain channels based on their transmission properties. Under this assumption we have

$$\sqrt{\frac{I_{\text{in}}}{\widetilde{I}_{\text{in}}}} = \sqrt{\frac{N_s}{N}} \tag{2.17}$$

so that

$$\left\langle |\gamma|_{\text{c}}^2 \right\rangle = \frac{N_s}{N}. \tag{2.18}$$

2.4.2 Temporal decorrelation

In a scattering system, the transmitted light is very sensitive to changes in the sample. As light encounters a phase shift at each of the many scattering events, the total acquired phase in a transmitted channel depends on the exact configuration of the individual scatterers. Sample drifts or small changes in, for example, temperature, humidity, and pressure therefore make the transmission matrix time dependent.

To control light in a dynamic disordered system, the required optimized field $\widetilde{E}(t)$ is time dependent. However, we generate our field at time $t = 0$ and keep it constant so that

$$E = \widetilde{E}(0) \neq \widetilde{E}(t). \tag{2.19}$$

The overlap γ between the generated field and the required field will therefore change in time

$$\gamma(t) = \frac{1}{\widetilde{I}_{\text{in}}(0)} \sum_{a=1}^{N} \widetilde{E}_a(t) \widetilde{E}_a^*(0), \tag{2.20}$$

where we assumed that the dynamics in the system only introduce additional phase shifts so that $\widetilde{I}_{\rm in}(t) = \widetilde{I}_{\rm in}(0)$.

By multiplying all terms in Eq. 2.20 with the same time dependent transmission matrix $t(t)$ we calculate the overlap $\gamma^{\rm tr}$ of the fields transmitted through the sample

$$\begin{aligned}\gamma^{\rm tr}(t) &= \frac{1}{T\widetilde{I}_{\rm in}(0)} \sum_{b=1}^{N} \widetilde{E}_b(t)\widetilde{E}_b^*(0) \\ &= \frac{1}{T\widetilde{I}_{\rm in}(0)} \sum_{b=1}^{N} \left[\sum_{a=1}^{N} \widetilde{E}_a(t) t_{ba} \sum_{a=1}^{N} \widetilde{E}_a^*(0) t_{ba}^* \right] \\ &= \frac{1}{T\widetilde{I}_{\rm in}(0)} \sum_{b=1}^{N} \left[\sum_{a=1}^{N} \widetilde{E}_a(t)\widetilde{E}_a^*(0) \left|t_{ba}\right|^2 + \sum_{a=1}^{N}\sum_{a'\neq a}^{N} \widetilde{E}_a(t)\widetilde{E}_{a'}^*(0) t_{ba} t_{ba'}^* \right],\end{aligned} \tag{2.21}$$

where T is the total transmission. Under ensemble averaging the crossterms average out to zero so that we have

$$\begin{aligned}\left\langle \gamma^{\rm tr}(t) \right\rangle &= \frac{\sum_{b=1}^{N} \left\langle \left|t_{ba}\right|^2 \right\rangle}{\langle T \rangle \widetilde{I}_{\rm in}(0)} \sum_{a=1}^{N} \widetilde{E}_a(t)\widetilde{E}_a^*(0) \\ &= \frac{1}{\widetilde{I}_{\rm in}(0)} \sum_{a=1}^{N} \widetilde{E}_a(t)\widetilde{E}_a^*(0).\end{aligned} \tag{2.22}$$

From this result we see that the ensemble averaged overlap of two transmitted fields $\langle \gamma^{\rm tr}(t) \rangle$ is equivalent to their overlap $\gamma(t)$ before they reach the sample.

The overlap (or correlation) between transmitted fields in dynamic multiple scattering systems is a well-studied subject in a technique known as diffusing wave spectroscopy (DWS)[27, 28]. DWS is a sensitive tool to extract rheological properties from a wide variety of turbid systems such as sand[29], foam[30, 31], and more recently GaP nanowires[32]. A good introduction into this field is given by Ref. [33] and references therein.

In DWS, the overlap between the transmitted fields is usually denoted as $g^{(1)}(t)$ and is equal to[33]

$$\gamma(t) = \langle \gamma_{\rm tr}(t) \rangle \equiv g^{(1)}(t) = \int_{\ell}^{\infty} ds P(s) e^{-\frac{s}{\ell}\left\langle \delta\phi^2(t) \right\rangle}, \tag{2.23}$$

where $\left\langle \delta\phi^2(t) \right\rangle$ is the mean square phase shift per scattering event, ℓ the transport mean free path, and $P(s)$ the normalized probability that light takes a path of length s through the sample.

The precise form of $g^{(1)}(t)$ depends strongly on $P(s)$, which is determined by the geometry of the sample and the nature of the scatterers. Typical mechanisms that cause dephasing of the field are Brownian motion of the scatterers or temperature, humidity, and pressure fluctuations[34] of the environment. For a

slab of finite thickness L the integral in Eq. 2.23 can be calculate in terms of a characteristic time $t_c = (2\tau/3)(\ell/L)^2$ that depends on the dephasing time τ.[13] The resulting expression becomes

$$\left\langle \left|\gamma_t\right|^2 \right\rangle = \left\langle \left|g^{(1)}\right|^2 \right\rangle = \left| \frac{\sqrt{t/t_c}}{\sinh\sqrt{t/t_c}} \right|^2 . \tag{2.24}$$

Depending on the type of material there are different factors that influence the dephasing time. In tissue, for example, dephasing was observed at several distinct time scales that were attributed to bulk motion, microscale cellular motion, and Brownian motion in the fluidic environment of the tissue[35].

2.4.3 Phase and amplitude errors

In an experiment both the measurement of the transmission matrix elements t_{ba} or the synthesis of the wave front will introduce phase and amplitude errors; $\delta\phi_a$ and δA_a respectively. As a result of these errors we have

$$E_a = \widetilde{E}_a A_a e^{i\delta\phi_a}, \tag{2.25}$$

where $A_a \equiv 1 + \delta A_a / \left|\widetilde{E}_a\right|$ is the amplitude modulation due to the error δA_a. If we now calculate the overlap between the ideal field and this modulated field we get

$$\gamma = \frac{1}{\sqrt{\widetilde{I}_{\text{in}} I_{\text{in}}}} \sum_{a=1}^{N} \left|\widetilde{E}_a\right|^2 A_a e^{-i\delta\phi_a}, \tag{2.26}$$

$$\left|\gamma\right|^2 = \frac{1}{\widetilde{I}_{\text{in}} I_{\text{in}}} \left(\sum_{a=1}^{N} A_a^2 \left|\widetilde{E}_a\right|^4 + \sum_{a=1}^{N} \sum_{a'\neq a}^{N-1} A_a A_{a'} \left|\widetilde{E}_a\right|^2 \left|\widetilde{E}_{a'}\right|^2 e^{i\delta\phi_a} e^{-i\delta\phi_{a'}} \right). \tag{2.27}$$

By ensemble averaging $\left|\gamma\right|^2$ we arrive at

$$\left\langle \left|\gamma_e\right|^2 \right\rangle = \frac{N \left\langle \left|\widetilde{E}_a\right|^4 \right\rangle}{\left\langle \widetilde{I}_{\text{in}}^2 \right\rangle} + \frac{\left\langle \left|\widetilde{E}_a\right|^2 \right\rangle^2}{\overline{A_a^2} \left\langle \widetilde{I}_{\text{in}}^2 \right\rangle} \sum_{a=1}^{N} \sum_{a'\neq a}^{N-1} A_a A_{a'} e^{i\delta\phi_a} e^{-i\delta\phi_{a'}}, \tag{2.28}$$

where the horizontal bar represent an average over all incident channels. For large values of N, the sum over a equals the sum over a'. If there is furthermore no systematic offset in the phase errors so that its average is zero, we arrive at

$$\lim_{N\to\infty} \left\langle \left|\gamma_e\right|^2 \right\rangle = \frac{\overline{A_a}^2}{\overline{A_a^2}} \overline{\cos\delta\phi_a}^2. \tag{2.29}$$

Phase only modulation

A large and important class of commercially available spatial light modulators is only capable of phase modulation. It is therefore relevant to study the overlap between an ideal wave front and a phase-only modulated wave front.

We distribute the incident intensity I_{in} equally over the N incident channels, such that $|E_a| = \sqrt{I_{\text{in}}/N}$ for every incident channel. Assuming furthermore perfect phase modulation, we can now calculate

$$\gamma = \frac{1}{I_{\text{in}}} \sum_{a=1}^{N} \widetilde{E}_a E_a^* = \frac{1}{\sqrt{N I_{\text{in}}}} \sum_{a=1}^{N} \left| \widetilde{E}_a \right|, \tag{2.30}$$

and from here

$$\gamma^2 = \frac{1}{N I_{\text{in}}} \left(\sum_{a=1}^{N} \left| \widetilde{E}_a \right|^2 + \sum_{a=1}^{N} \sum_{a' \neq a}^{N-1} \left| \widetilde{E}_a \right| \left| \widetilde{E}_{a'} \right| \right). \tag{2.31}$$

Ensemble averaging this over all realizations of disorder results in

$$\left\langle \gamma_{\text{e}}^2 \right\rangle = \frac{1}{N I_{\text{in}}} \left(N \left\langle \left| \widetilde{E}_a \right|^2 \right\rangle + N(N-1) \left\langle \left| \widetilde{E}_a \right| \right\rangle^2 \right). \tag{2.32}$$

The amplitudes of the ideal wave front are proportional to the corresponding transmission matrix elements and therefore share the same distribution. The matrix elements can be assumed to have a circular Gaussian distribution[36] so that we arrive at

$$\left\langle \gamma_{\text{e}}^2 \right\rangle = \frac{\pi}{4} + \frac{1}{N} \left(1 - \frac{\pi}{4} \right). \tag{2.33}$$

which for large N converges to $\pi/4$. So even for a perfectly phase modulated wave front, $\langle \gamma^2 \rangle$ is smaller than 1.

Binary amplitude modulation

With the development of fast micro mirror devices that selectively block the reflection from certain pixels in order to modulate the wave front, it is interesting to consider the case where we allow only binary amplitude modulation.

We set the phase of the complete wave front to zero and distribute the incident intensity equally over a specific set of incident channels. Then we decide which channels should be illuminated. For this purpose we create a subset of incident channels based on the phase difference between $\widetilde{E}_a$ and E_a

$$a^+ \equiv \left\{ a \middle| \arg\left(\left| \widetilde{E}_a - E_a \right| \right) \leq \pi/2 \right\}. \tag{2.34}$$

The set a^+ contains all channels of which the illumination is less than $\pi/2$ out of phase with the desired field. Now that we have created this set, we modulate our field as

$$E_a = \begin{cases} \sqrt{I_{\text{in}}/N} & \text{if } a \in a^+ \\ 0 & \text{otherwise.} \end{cases}$$

As a result we have

$$\gamma = \frac{1}{\sqrt{NI_{\text{in}}}} \sum_{a \in a^+} \widetilde{E}_a, \tag{2.35}$$

$$\gamma^2 = \frac{1}{NI_{\text{in}}} \left(\sum_{a \in a^+} \left| \widetilde{E}_a \right|^2 + \sum_{a \in a^+} \sum_{a' \neq a} \widetilde{E}_a \widetilde{E}^*_{a'} \right). \tag{2.36}$$

$$\left\langle \gamma^2 \right\rangle = \frac{1}{NI_{\text{in}}} \left(M \left\langle \left| \widetilde{E}_a \right|^2 \right\rangle + M(M-1) \left\langle \widetilde{E}_a \right\rangle^2 \right), \tag{2.37}$$

where M is the cardinality of the set a^+. Normally $\left\langle \widetilde{E}_a \right\rangle$ would average out to zero, but due to the selective illumination this is no longer true. We find that

$$\left\langle \widetilde{E}_a \right\rangle = \frac{1}{\pi} \int_{-\pi/2}^{\pi/2} \cos\theta \left\langle \left| \widetilde{E}_a \right| \right\rangle d\theta = \frac{2}{\pi} \left\langle \left| \widetilde{E}_a \right| \right\rangle, \tag{2.38}$$

where we integrated over the relative phase $\theta \equiv \arg\left(\widetilde{E}_a - E_a \right)$. The ensemble averaged value of γ^2 then is

$$\left\langle \gamma^2 \right\rangle = \frac{M^2}{N^2} \frac{1}{\pi} + \frac{M}{N^2} \left(1 - \frac{1}{\pi} \right). \tag{2.39}$$

If we assume that the phase of $\widetilde{E}_a$ is homogenously distributed between $-\pi$ and π so that $M = N/2$ we arrive at

$$\left\langle \gamma_{\text{e}}^2 \right\rangle = \frac{1}{4\pi} + \frac{1}{2N} \left(1 - \frac{1}{\pi} \right), \tag{2.40}$$

which converges to $1/4\pi$ for large values of N. So by only selectively blocking parts of the incident wave front it is already possible to control a large fraction of the transmitted light.

2.5 Optimizing light into a single channel

The first experimental demonstration of light control in disordered systems using explicit knowledge of the transmission matrix elements was given by Vellekoop and Mosk in 2007[18]. In this pioneering experiment they demonstrated that a random scattering samples can focus scattered light by illuminating them with the correct wave front. The light, after being scattered thousands of times, interfered constructively into one of the transmitting channels, thereby creating a tight focus behind the sample. In this section we will study the intensity enhancement η in such a focus.

The enhancement in the focus is defined as

$$\eta \equiv \frac{\widetilde{I}_\beta}{\langle I_\beta \rangle}, \tag{2.41}$$

where $\widetilde{I}_\beta$ is the optimized intensity in in the focus and $\langle I_\beta \rangle$ the ensemble averaged intensity under normal illumination. First we will consider the expected enhancement under perfect modulation of the incident wave front and then we will look at realistic experimental conditions to estimate the enhancement we can expect in our experiments.

2.5.1 Enhancement under ideal modulation

To find the maximal intensity in β we use the Cauchy-Schwartz inequality to write

$$I_\beta = \left| \sum_{a=1}^{N} t_{\beta a} E_a^* \right|^2 \leq \sum_{a=1}^{N} |t_{\beta a}|^2 \sum_{a=1}^{N} |E_a|^2. \tag{2.42}$$

The left and right side are only equal if $E_a = A\sqrt{I_{\text{in}}} t_{\beta a}^*$ with $A \in \mathbb{C}$. This condition results in the exact phase conjugate of a transmitted field that would emerge if we illuminate only channel β.

We maximize the intensity in β by taking

$$\widetilde{E}_a = A\sqrt{I_{\text{in}}} t_{\beta a}, \text{ with } A \equiv \frac{1}{\sqrt{\sum_{a=1}^{N} |t_{\beta a}|^2}}, \tag{2.43}$$

where the value for A normalizes $\widetilde{E}$. The optimized intensity then becomes

$$\widetilde{I}_\beta = I_{\text{in}} \sum_{a=1}^{N} |t_{\beta a}|^2. \tag{2.44}$$

If we keep illuminating the sample with the same field we defined by Eq. 2.43 while changing the realization of disorder, we find a value for the unoptimized intensity. To describe this different realization we define a new transmission matrix ξ that is completely uncorrelated with the former matrix t. The unoptimized intensity I_β is now

$$\begin{aligned} I_\beta &= I_{\text{in}} \left| \sum_{a=1}^{N} \xi_{\beta a} A t_{\beta a}^* \right|^2 \\ &= I_{\text{in}} A^2 \left(\sum_{a=1}^{N} |\xi_{\beta a}|^2 |t_{\beta a}|^2 + \sum_{a=1}^{N} \sum_{a \neq a'}^{N-1} \xi_{\beta a} t_{\beta a}^* \xi_{\beta a}^* t_{\beta a} \right). \end{aligned} \tag{2.45}$$

To calculate the intensity enhancement, we have to be very careful how we ensemble average over disorder. To average $\widetilde{I}_\beta$ we should ensemble average the elements $t_{\beta a}$. For I_β however, the elements $t_{\beta a}$ are associated only with the illumination and do therefore not change under an ensemble average over disorder. In this case we should average the elements $\xi_{\beta a}$ that correspond to the sample

disorder. The intensity enhancement therefore is

$$\begin{aligned}\langle\eta\rangle &= \frac{\left\langle \widetilde{I}_\beta \right\rangle_t}{\langle I_\beta \rangle_\xi} \\ &= \frac{N \left\langle |t_{\beta a}|^2 \right\rangle_t \sum_{a=1}^{N} |t_{\beta a}|^2}{\left\langle |\xi_{\beta a}|^2 \right\rangle_\xi \sum_{a=1}^{N} |t_{\beta a}|^2 + \left\langle \sum_{a=1}^{N} \sum_{a\neq a'}^{N-1} \xi_{\beta a} t^*_{\beta a} \xi^*_{\beta a} t_{\beta a} \right\rangle_\xi},\end{aligned} \tag{2.46}$$

where we added subscripts to the angled brackets to clarify over which elements we average. Because the matrices t and ξ are uncorrelated while the average absolute squared value of both its elements are equal this equation simplifies to

$$\langle\eta\rangle = N. \tag{2.47}$$

So for a perfectly controlled wave front the intensity enhancement is equal to the total amount of channels.

2.5.2 Enhancement under experimental modulation

In an experimental environment, the ideal field can only be approximated. Any experimental limitations therefore lower the optimal intensity $\widetilde{I}_\beta$ with a factor $|\gamma|^2$. The experimental attainable enhancement is then

$$\langle\eta\rangle = \left\langle |\gamma|^2 \right\rangle N. \tag{2.48}$$

For our experiments, there are three main experimental factors that lower $\left\langle |\gamma|^2 \right\rangle$. First there is the limited amount of control caused by a grouping of individual modulator pixels into larger segments. By creating these segments, we require less time to generate our wave front at the cost of reduced control. Secondly we have a degradation of our wave front because we only modulate the phase while keeping the amplitude constant. The last contribution is due to a nonuniform illumination profile of the modulator which makes that not all addressed channels are illuminated equally.

Figure 2.3 shows typical results of an experiment where we optimized light into a single scattering channel through a disordered zinc oxide sample. In panel a we see a two dimensional map containing the illumination amplitudes A_a of the different segments of the light modulator. From this map we find $\overline{A_a}^2/\overline{A_a^2} = 0.94$ and $N_s = 133$. Combining these results with the results of Section 2.4 we find

$$\langle\eta\rangle \approx N_s \frac{\pi}{4} \frac{\overline{A_a}^2}{\overline{A_a^2}} = 98. \tag{2.49}$$

The measured intensity enhancements for 25 experimental runs are shown in panel b together with the average experimental enhancement (solid line) and the expected enhancement (dashed line). We see that our average enhancement of

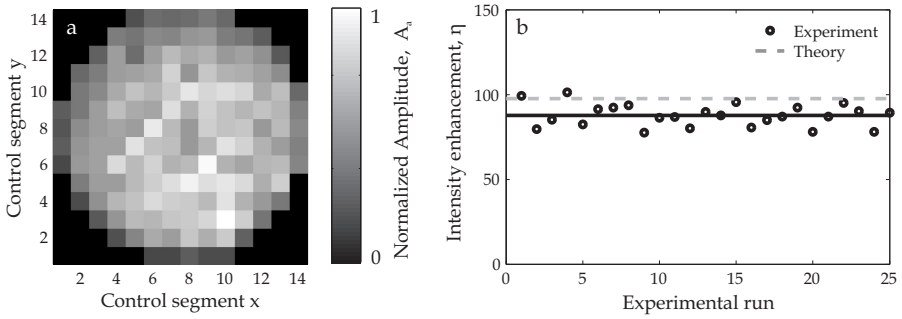

Figure 2.3: a: Two dimensional map containing the normalized incident amplitudes of every control segment on the modulator. **b:** Intensity enhancements by optimizing the wave front for 25 experimental runs at different positions on a disordered zinc oxide sample. Solid line: average enhancement, dotted line: theoretical expected enhancement.

88 ± 6 is in good agreement with the theoretical expected enhancement. The small difference between the two is most likely due to noise induced phase errors in the measurement of the matrix elements.

For experiments with high enhancements, the full $|\gamma|^2$ is reliable obtained from a comparison of the intensity enhancement with the background [37]. In that case one does not need any information on the individual contributions.

2.6 Angular positioning of scattered light

Although coherent wave propagation through disordered systems might seem completely random, there exist short-, long-, and infinite-range correlation in the scattered field[38]. Such correlations were initially derived for mesoscopic electron transport in disordered conductors[39] and later adopted to successfully describe correlations of optical waves in multiple scattering systems[40] where transmission takes over the role of conductivity.

In a typical optical experiment, the short-range correlations are most prominent as these are the cause of the granular intensity pattern known as speckle. Another striking feature caused by short range correlations is the so called angular memory effect. This effect makes that the scattered light 'remembers' the direction of the illumination. By tilting the incident beam is it possible to control the angular position of the speckle pattern. Combined with spatial wave front modulation, a precisely controlled scanning spot can be generated.[41–43]

In this section we first develop an intuitive picture of the origin of the optical memory effect and then we discuss the dependence of this correlation on several relevant experimental parameters on the basis of quantitative results obtained before[40, 44].

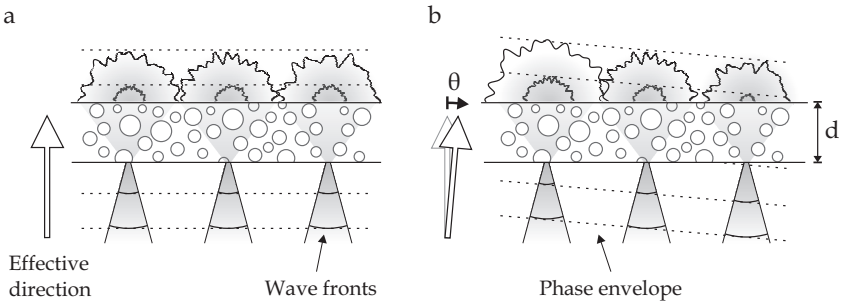

Figure 2.4: Schematic picture explaining the optical memory effect of scattered light in transmission. **a:** An array of spots that are imaged onto the surface of a disordered slab with thickness d. The spots are separated by a distance that is larger than the sample thickness and arrive with equal face at the surface of the slab. In transmission a complex field pattern arises from three independent areas. The dotted lines denote the baseline phase envelope. **b:** The relative phase between the three spots is changed to resemble a tilt θ of the phase envelope. As the relative phase of each of the transmission areas is directly related to the phase of the spot from which it emerges, the transmitted light encounters the same relative phase change.

2.6.1 Optical memory effect

At first sight the optical memory effect seems counterintuitive as multiple scattered light has seemingly lost all correlation with the original incident beam. A intuitively understanding of the memory effect can be gained by considering the geometry depicted in Fig. 2.4. A disordered slab of thickness d is illuminated by an array of light spots. The light that incidents on the slab diffuses and spreads over circular area with a radius of approximately d at the exit surface of the sample.

In Fig. 2.4a all the spots arrive at the slab with an equal phase as is seen by the horizontal phase envelope (dotted lines). The transmitted light fluctuates strongly as a result of the multiple scattering in the sample. These fluctuations make it elaborate to denote the phase envelope. However, as we are only interested in the relative phase changes we can define an effective phase envelope without loss of generality. We choose the baseline effective phase envelope horizontal.

Tilting of the incident wave front over an angle θ is accomplished by applying a linear phase gradient as is shown in Fig. 2.4b. In our geometry this gradient is reflected in relative phase shifts between the different incident spots. As long as the illuminated areas of the individual spots are well separated, the transmitted fields emerging from each of them are independent. Changing the phase of any of the incident spots will therefore only affect a confined region of the transmission. As a result the different transmitted fields encounter the same relative phase shifts resulting in a net tilt of the transmitted field over the same angle θ.

By increasing the thickness of the slab or by moving the incident spots closer to each other, the different transmitted areas will eventually overlap. Due to this overlap, a tilt in the wave front will also induce a loss of correlation in the transmitted field. In the limit where the incident spots are so close that they form a continuous illuminated area, the transmitted field will always decorrelate to some extent. The thickness of the sample then determines the angular scale on which the decorrelation takes place.

2.6.2 Short range correlation

Mathematically the memory effect is understood from a careful analysis of the scattering trajectories through the sample. Isolating the different combinations of trajectories in the correlation function that do not average out under ensemble averaging results directly in the short, long, and infinite range correlations.[13, 40] A thorough review by Berkovits and Feng[45] as well as the book of Akkermans and Montambaux[13] provide an insightful description of these correlations. Here we will only highlight the results relevant for the optical memory effect.

The memory effect is governed by the short range correlations, which are usually denoted by $C^{(1)}_{aba'b'}$ because they are the first order contributions to the total intensity-intensity correlation function $C_{aba'b'}$ between light in incident (a and a') and transmitted (b and b') scattering channels. Light that arrives at an angle θ with respect to the sample surface carries a transverse momentum

$$q = |\mathbf{k}| \sin\theta. \tag{2.50}$$

Short range correlations rely strongly upon the transverse momentum difference $\Delta q_a \equiv q_a - q_{a'}$ of the light in the different channels. Most generally these correlations are written as

$$C^{(1)}_{aba'b'} = g\left(\Delta q_a - \Delta q_b\right) \left(\frac{\Delta q_a d}{\sinh \Delta q_a d}\right)^2. \tag{2.51}$$

The function $g\left(\Delta q_a - \Delta q_b\right)$ depends on the geometry of the illumination. When an infinitely extended plane interface is illuminated by a plane wave this function becomes a Kronecker delta δ_{ab}. In an experiment where only a finite area is illuminated, the function takes a more complex form. For a circular illuminated area with a width W the function becomes[13]

$$g\left(\Delta q_a - \Delta q_b\right) = \left[\frac{2J_1\left(\left|\Delta q_a - \Delta q_b\right| W\right)}{\left|\Delta q_a - \Delta q_b\right| W}\right]^2, \tag{2.52}$$

where J_1 denotes a Bessel function of the first kind.

There are several important observations that can be made from Eq. 2.51. The function $g\left(\Delta q_a - \Delta q_b\right)$ depends only on the difference between Δq_a and Δq_b. An angular change $\Delta q_a \ll 1/d$ of the incident beam results therefore in an equal angular tilt of the transmitted field. For larger angles the second factor in Eq. 2.51 decreases the correlation, thereby restraining the angular memory range.

As can also be seen from the intuitive picture we developed in section 2.6.1, the memory angle scales with $1/kd$ and does not depend on the mean free path ℓ. In the case where $a' = a$, the angular correlation $C^{(1)}_{abab'}$ yields the typical width of a speckle and is given by the function g, which scales with $1/kW$. By choosing the width of the illumination beam larger than the sample thickness, it is possible to separate the two angular correlation scales.

2.7 Summary

In this chapter we discussed the concept of scattering and transmission matrices that can be used to describe complex wave transport in disordered materials. With spatial control over the wave front it is possible to measure a large amount of elements of these matrices. When this information is known, light propagation through disordered materials can be controlled by spatially manipulating the wave front of the light before it impinges onto the sample.

With spatial wave front shaping it is possible to direct scattered light into a designated transmission direction to create a sharp and intense focus. Angular correlations in scattered light can then be exploited to steer this focus around. In this chapter we studied this special case of wave front shaping and developed an intuitive picture for the angular correlations. As experimental factors always limit the amount of control over the light field, we furthermore investigated the influence of imperfect modulation for several important experimental limitations.

Bibliography

[1] J. F. de Boer, M. C. W. van Rossum, M. P. van Albada, T. M. Nieuwenhuizen, and A. Lagendijk, *Probability distribution of multiple scattered light measured in total transmission*, Phys. Rev. Lett. **73**, 2567 (1994). — p.21.

[2] F. Scheffold and G. Maret, *Universal conductance fluctuations of light*, Phys. Rev. Lett. **81**, 5800 (1998). — p.21.

[3] M. P. van Albada and A. Lagendijk, *Observation of weak localization of light in a random medium*, Phys. Rev. Lett. **55**, 2692 (1985). — p.21.

[4] P.-E. Wolf and G. Maret, *Weak localization and coherent backscattering of photons in disordered media*, Phys. Rev. Lett. **55**, 2696 (1985). — p.21.

[5] P. W. Anderson, *Absence of diffusion in certain random lattices*, Phys. Rev. **109**, 1492 (1958). — p.21.

[6] D. S. Wiersma, P. Bartolini, A. Lagendijk, and R. Righini, *Localization of light in a disordered medium*, Nature **390**, 671 (1997). — p.21.

[7] F. J. P. Schuurmans, M. Megens, D. Vanmaekelbergh, and A. Lagendijk, *Light scattering near the localization transition in macroporous gap networks*, Phys. Rev. Lett. **83**, 2183 (1999). — p.21.

[8] M. Störzer, P. Gross, C. M. Aegerter, and G. Maret, *Observation of the critical regime near Anderson localization of light*, Phys. Rev. Lett. **96**, 063904 (2006). — p.21.

[9] A. Lagendijk, B. van Tiggelen, and D. S. Wiersma, *Fifty years of Anderson localization*, Phys. Today **62**, 24 (2009). — p.21.

[10] S. E. Skipetrov, *Information transfer through disordered media by diffuse waves*, Phys. Rev. E **67**, 036621 (2003). — p.21.
[11] I. Freund, *Looking through walls and around corners*, Physica A: Statistical Mechanics and its Applications **168**, 49 (1990). — p.21.
[12] C. W. J. Beenakker, *Random-matrix theory of quantum transport*, Rev. Mod. Phys. **69**, 731 (1997). — p.21, 23.
[13] E. Akkermans and G. Montambaux, *Mesoscopic physics of electrons and photons* (Cambridge Univ. Press, Cambridge, U.K., 2006). — p.21, 29, 36.
[14] I. Vellekoop, *Controlling the propagation of light in disordered scattering media*, Ph.D. thesis, University of Twente, 2008. — p.21.
[15] E. P. Wigner, *On the statistical distribution of the widths and spacings of nuclear resonance levels*, Mathematical Proceedings of the Cambridge Philosophical Society **47**, 790 (1951). — p.23.
[16] P. J. Forrester, N. C. Snaith, and J. J. M. Verbaarschot, *Developments in random matrix theory*, Journal of Physics A: Mathematical and General **36**, R1 (2003). — p.23.
[17] J. Pendry, A. MacKinnon, and A. Pretre, *Maximal fluctuations – a new phenomenon in disordered systems*, Physica A: Statistical Mechanics and its Applications **168**, 400 (1990). — p.23.
[18] I. M. Vellekoop and A. P. Mosk, *Focusing coherent light through opaque strongly scattering media*, Opt. Lett. **32**, 2309 (2007). — p.24, 31.
[19] S. M. Popoff, G. Lerosey, R. Carminati, M. Fink, A. C. Boccara, and S. Gigan, *Measuring the transmission matrix in optics: An approach to the study and control of light propagation in disordered media*, Phys. Rev. Lett. **104**, 100601 (2010). — p.24, 25.
[20] I. M. Vellekoop and A. P. Mosk, *Phase control algorithms for focusing light through turbid media*, Opt. Comm. **281**, 3071 (2008). — p.25.
[21] E. N. Leith and J. Upatnieks, *Holographic imagery through diffusing media*, J. Opt. Soc. Am. **56**, 523 (1966). — p.26.
[22] Z. Yaqoob, D. Psaltis, M. S. Feld, and C. Yang, *Optical phase conjugation for turbidity suppression in biological samples*, Nat. Photon. **2**, 110 (2008). — p.26.
[23] M. Cui and C. Yang, *Implementation of a digital optical phase conjugation system and its application to study the robustness of turbidity suppression by phase conjugation*, Opt. Express **18**, 3444 (2010). — p.26.
[24] D. Gabor, *A new microscopic principle*, Nature **161**, 777 (1948). — p.26.
[25] M. Ozaki, J.-i. Kato, and S. Kawata, *Surface-plasmon holography with white-light illumination*, Science **332**, 218 (2011). — p.26.
[26] B. Gjonaj, J. Aulbach, P. M. Johnson, A. P. Mosk, L. Kuipers, and A. Lagendijk, *Active spatial control of plasmonic fields*, Nat. Photon. **5**, 360 (2011). — p.26.
[27] G. Maret and P. E. Wolf, *Multiple light scattering from disordered media. the effect of brownian motion of scatterers*, Zeitschrift fr Physik B Condensed Matter **65**, 409 (1987), 10.1007/BF01303762. — p.28.
[28] M. Rosenbluh, M. Hoshen, I. Freund, and M. Kaveh, *Time evolution of universal optical fluctuations*, Phys. Rev. Lett. **58**, 2754 (1987). — p.28.
[29] N. Menon and D. J. Durian, *Diffusing-wave spectroscopy of dynamics in a three-dimensional granular flow*, Science **275**, 1920 (1997). — p.28.
[30] D. J. Durian, D. A. Weitz, and D. J. Pine, *Multiple light-scattering probes of foam structure and dynamics*, Science **252**, 686 (1991). — p.28.
[31] A. D. Gopal and D. J. Durian, *Fast thermal dynamics in aqueous foams*, J. Opt. Soc. Am. A **14**, 150 (1997). — p.28.

[32] M. Abb, E. P. A. M. Bakkers, and O. L. Muskens, *Ultrafast dephasing of light in strongly scattering GaP nanowires*, Phys. Rev. Lett. **106**, 143902 (2011). — p.28.
[33] G. Maret, *Diffusing-wave spectroscopy*, Current Opinion in Colloid & Interface Science **2**, 251 (1997). — p.28.
[34] S. Faez, P. M. Johnson, and A. Lagendijk, *Varying the effective refractive index to measure optical transport in random media*, Phys. Rev. Lett. **103**, 053903 (2009). — p.28.
[35] M. Cui, E. J. McDowell, and C. Yang, *An in vivo study of turbidity suppression by optical phase conjugation (tsopc) on rabbit ear*, Opt. Express **18**, 25 (2010). — p.29.
[36] J. Goodman, *Statistical optics* (Wiley, New York, 2000). — p.30.
[37] I. Vellekoop and A. Mosk, *Universal optimal transmission of light through disordered materials*, Phys. Rev. Lett. **101**, 120601:1 (2008). — p.34.
[38] S. Feng and P. A. Lee, *Mesoscopic conductors and correlations in laser speckle patterns*, Science **251**, 633 (1991). — p.34.
[39] S. Datta, *Electronic transport in mesoscopic systems* (Cambridge University Press, Cambridge, 2007). — p.34.
[40] S. Feng, C. Kane, P. A. Lee, and A. D. Stone, *Correlations and fluctuations of coherent wave transmission through disordered media*, Phys. Rev. Lett. **61**, 834 (1988). — p.34, 36.
[41] I. Vellekoop and C. Aegerter, *Scattered light fluorescence microscopy: imaging through turbid layers*, Opt. Lett. **35**, 1245 (2010). — p.34.
[42] C.-L. Hsieh, Y. Pu, R. Grange, G. Laporte, and D. Psaltis, *Imaging through turbid layers by scanning the phase conjugated second harmonic radiation from a nanoparticle*, Opt. Express **18**, 20723 (2010). — p.34.
[43] E. G. van Putten, D. Akbulut, J. Bertolotti, W. L. Vos, A. Lagendijk, and A. P. Mosk, *Scattering lens resolves sub-100 nm structures with visible light*, Phys. Rev. Lett. **106**, 193905 (2011). — p.34.
[44] I. Freund, M. Rosenbluh, and S. Feng, *Memory effects in propagation of optical waves through disordered media*, Phys. Rev. Lett. **61**, 2328 (1988). — p.34.
[45] R. Berkovits and S. Feng, *Correlations in coherent multiple scattering*, Physics Reports **238**, 135 (1994). — p.36.

CHAPTER 3
Disordered Photonic Structures

3.1 Introduction

For the study and control of light propagation in disordered photonic structures we designed and fabricated several suitable samples. To maximize the light matter interaction, low absorption and strong scattering are desired. These conditions are met by creating inhomogeneous structures with wavelength-scale refractive index fluctuations out of transparent materials. Porous gallium phosphide[1], ensembles of polystyrene spheres[2–4], and powders made out of titanium dioxide[5, 6], gallium arsenide[7], gallium nitride[8], and zinc oxide[9] are all known to strongly scatter light. In our experiments we used zinc oxide (ZnO) pigment and porous gallium phosphide (GaP) as scattering materials.

Zinc oxide is an ideal material to be used in combination with common red fluorescent dyes, such as Rhodamine 6G, as it does not show any significant autofluorescence in the spectral range where these dyes emit. In high resolution imaging experiments, the refractive index n of the material plays a large role as the resolution improves with increasing n. In this case gallium phosphide is an excellent candidate, which provides a high refractive index while being transparent in a large part of the visible spectrum.

In this chapter we detail the fabrication and characterization of two types of samples. The first type are disordered layers of zinc oxide which are combined with fluorescent emitters. The second type of samples are high resolution scattering lenses made out of gallium phosphide.

3.2 Disordered zinc oxide layers

To conveniently create scattering layers from powders we developed a versatile spray painting method. The method is easily extended to include a controlled density of nano scale emitters into the layer. With this technique we created turbid ZnO layers combined with dye doped polystyrene nano spheres in different geometries. Aside from our own experiments, we provided these samples for several other experiments in our own[10, 11] and in other groups[12, 13].

3.2.1 Fabrication

We created ZnO samples in four different configurations, which are shown in Fig. 3.1. The fabrication of these disordered samples can be divided into four

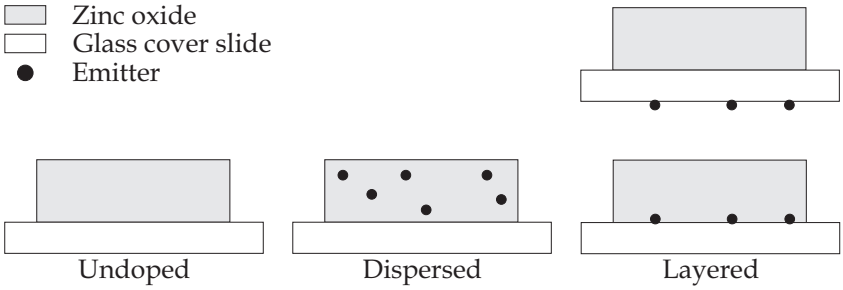

Figure 3.1: Schematic representation of disordered zinc oxide samples in different geometries. The undoped samples, only consist of a disordered layer of ZnO pigment on top of a glass cover slide. The samples that are doped with emitters were fabricated in three geometries. The dispersed samples contain a random configuration of emitters inside the disordered layers. The layered samples have emitters in a single plane, either on top or below the glass cover slide.

basis steps. Depending on the specific sample configuration some of these steps have to be combined or some can be omitted. We first describe the fabrication of the undoped ZnO layers and then detail the different doped geometries.

Undoped samples

We start by cleaning the sample substrates to get rid of any surface contaminations. For our samples we use standard 40x24 mm^2 microscope cover glasses with a thickness of 160 µm. The cover glasses are first washed with acetone to remove organic residuals. Then we rinse them with isopropanol and water to prevent the formation of drying stains. We leave the cover glasses to dry for approximately half an hour at room temperature.

In the mean time, we prepare a suspension of ZnO out of a commercially available ZnO nano powder (Aldrich Zinc Oxide < 1 µm 99.9%) with an average grain size of 200 nm. By testing different concentrations of ZnO in demineralized water we found that approximately 5 volume percent results in the optimal viscosity to spray paint it. To achieve this concentration, 10 g ZnO powder is mixed with 35 ml H_2O. The suspension is placed on a roller bank for an hour to ensure that it is thoroughly mixed. Finally we put the suspension for 15 minutes in the ultrasonic bath to prevent clustering of the ZnO grains.

The glass substrates are mounted on a holder under an angle of approximately 45 degrees. We use a professional airbrush (Evolution Silverline) to spray paint the ZnO suspension onto the substrates. The sprayed samples are placed horizontally for half a day at room temperature. During this time, the water evaporates and a strongly disordered structure remains. The thickness of the layer is controlled by changing the spray time. With the current ZnO suspension it is possible to create layer thicknesses up to approximately 30 µm before the suspension starts to drip from the substrate. This thickness is more than enough to

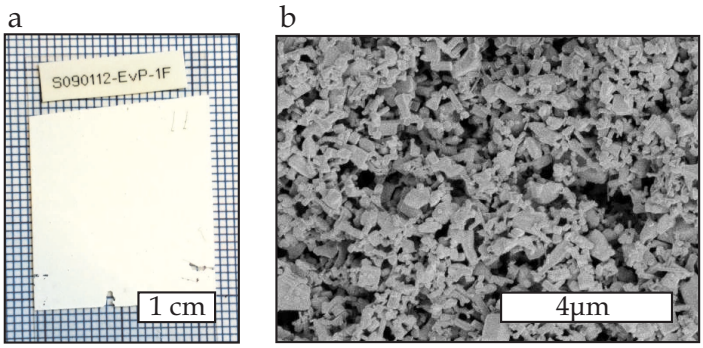

Figure 3.2: a: Photograph of a ZnO layer spray painted on top of a microscope cover glass. **b:** Scanning electron micrograph of the cross section of a typical disordered ZnO layer.

make the samples fully opaque. If thicker layers are required, it is possible to first dry the first layer and then spray a second layer on top of it. Figure 3.2 shows a photograph of the top the dried sample and a scanning electron micrograph detailing the cross section of the disordered layer.

Doped samples

In several of our experiments we use dye doped polystyrene spheres of different sizes as emitters. The spheres are produced by Duke Scientific (now Thermo Scientific) and are available in a wide range of sizes. They are doped with dye molecules that have their absorption peak at 542 nm and their emission peak at 612 nm. The polymer matrix of the sphere rigidly holds the dye molecules and protects them from the chemical environment.

To use the dye doped spheres, we prepare a suitable concentration of these emitters in demineralized water. The supplied spheres are already suspended in water. The particle concentration C is easily calculated from the specified particle diameter D, the specified mass fraction of particles w_p, the densities of the water ρ_w and the particles ρ_p as[14]

$$C = \frac{w_p \rho_w}{\frac{\pi}{6} D^3 \left[w_p (\rho_w - \rho_b) + \rho_b \right]}. \tag{3.1}$$

The desired particle concentration C_d depends on the required density of spheres in our sample. This concentration is usually much lower than the supplied concentration C so that we have to dilute the supplied suspension

$$M \equiv C/C_d \tag{3.2}$$

times. Both before and after the dilution process we ensure a homogeneous distribution of the spheres in the suspension by placing it for half an hour on a roller bank and immersing in an ultrasonic bath for 15 seconds.

For the dispersed samples we use the sphere suspension instead of water to prepare the ZnO suspension. We choose the particle concentration $C_d \approx 5 \cdot 10^6$ particles/mL, such that in the resulting sample the average spacing between two spheres is in the order of 100 µm. At this concentration, the spheres are well separated so that the diffusing emission of every sphere inside the scattering layer can be measured individually from outside the sample. For our experiments we prepared samples with two different sphere sizes D. To get the desired concentrations, the dilution factors M are in the order of

$$M = \begin{cases} 8.8 \cdot 10^5 & \text{for D = 160 nm} \\ 1.3 \cdot 10^5 & \text{for D = 300 nm.} \end{cases}$$

In the layered samples, the emitters are positioned directly on the glass cover slide. For the experiments described in Chapter 4 we required the emitters to be in between the glass and the ZnO. The experiments in Chapter 8 required slightly different layered geometry where the emitters were at a fixed distance from the scattering layer. Both these layered geometries are fabricated in an almost identical way, with only the spray painted side of the glass cover slides differently chosen.

We place the cleaned glass cover slides on the bottom of a petri dish. The spheres suspension is poured into the petri dish. The height level of the suspension has to be approximately 3 mm to completely cover the glass cover slides. In our samples, we want the average distance between two dyed spheres to be in the order of 10 µm resulting in a desired concentration $C_d = 3.3 \cdot 10^6$ particles/mL. The required dilution factors M are

$$M = \begin{cases} 1.3 \cdot 10^6 & \text{for D = 160 nm} \\ 2.0 \cdot 10^5 & \text{for D = 300 nm.} \end{cases}$$

We place the petri dish in an oven at a temperature of 40 $^\circ C$ until all the water is evaporated. The dyed spheres remain on the glass cover glasses, creating a random distribution of fluorescent probes. Now we spray paint either the front or the back of the cover slides with the ZnO suspension.

3.2.2 Characterization

In this subsection we carefully study the light transport properties of the fabricated ZnO samples by means of an escape function and a total transmission measurement. With these measurements we are able to find the effective refractive index and the transport mean free path of the disordered layers. In both experiments we use a broadband light source so that the samples are characterized for a wide range of wavelengths.

Effective refractive index

The refractive index defines the phase velocity of a propagating wave in a homogeneous material. For heterogeneous structures, in which the refractive index is

strongly position dependent, it is better to adopt an effective refractive index to characterize the material.

The effective refractive index n_e of a strongly scattering material can be found by measuring the angular resolved transmission of light.[15] In the diffusion approximation, the angular resolved transmission probability $P(\mu_e)$ is equal to[16]

$$\frac{P(\mu_e)}{\mu_e} = \left(\frac{n_e}{n_0}\right)^2 \left(\frac{1+\overline{R}}{1-\overline{R}} + \frac{3}{2}\mu\right) [1 - R(\mu)], \tag{3.3}$$

where $\mu = \cos\theta$ and $\mu_e = \cos\theta_e$ are the projections of the incident angle θ and the transmitted angle θ_e perpendicular to the sample surface. The specific and angle averaged reflectivity at the surface, $R(\mu)$ and $\overline{R}$, are directly calculated from the Fresnel coefficients. These reflectivities solely depend on the refractive index contrast n_e/n_0 between the interior and the exterior of the sample and the polarization. An experimentally acquired $P(\mu_e)$ for a fixed polarization can therefore be used to determine the refractive index contrast.

We use a broadband angle-dependent light scattering setup equivalent to the apparatus that is described in Ref. [17]. The setup is placed in transmission mode to measure the angular resolved transmission through our ZnO samples. The sample is illuminated by a supercontinuum light source, which enables a measurement of the effective refractive index over a wavelength range from 500 nm up to 900 nm.

The experimental results are shown in Fig. 3.3. In panel a we see the spectrally resolved transmission as function of the outgoing angle θ_e. This data is the p-polarized transmission averaged over 6 measurements on different sample positions. We plotted $P(\mu_e)/\mu_e$ for a wavelength of 532 nm in panel b. By fitting this data with the refractive index contrast as the only free parameter, we find $n_e = 1.34$. We repeated this procedure for all measured wavelengths to determine the spectral dependence of n_e, which is shown in panel c. The gray area denotes the error that we estimated by comparing the fits to the data for different values of the refractive index.

Transport mean free path

In heterogeneous structures light is scattered as it propagates. The average distance light travels before it completely looses direction is defined as the transport mean free path ℓ. In our samples that consist of isotropic scatterers, the transport mean free path is equal to the scattering mean free path. The amount of unscattered transmitted light reduces as $e^{-L/\ell}$, where L is the layer thickness. Therefore, a sample with a thickness of at least a few times the mean free path is optically thick and opaque.

The transport mean free path can be obtained from a measurement of the total diffusive transmission T as function of the layer thickness L. The total transmission is inversely proportional to[18]

$$\frac{1}{T} = \frac{L + z_{e1} + z_{e2}}{\ell + z_{e1}}, \tag{3.4}$$

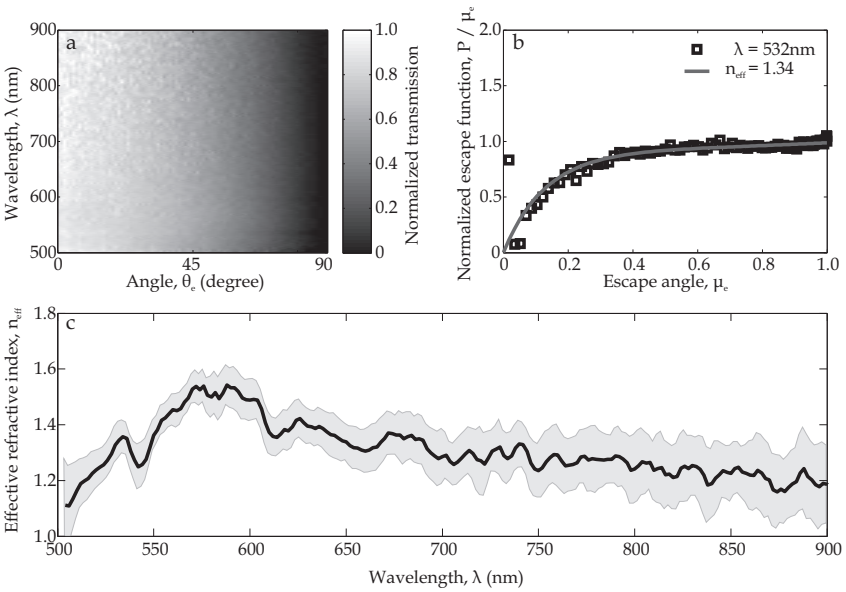

Figure 3.3: Results of angular resolved measurements of the transmission through a ZnO sample. **a:** The spectrally resolved normalized transmission as a function of the outgoing angle θ_e. This transmission is averaged over 6 different positions on the sample. **b:** Normalized escape function $P(\mu_e)/\mu_e$ as function of the escape angle μ_e for a wavelength of 532 nm. From a fit to the data we find that at this wavelength, the effective refractive index $n_{\text{eff}} = 1.34$. **c:** Spectrally resolved effective refractive index obtained from the transmission data in panel a. The gray area indicates the error that we estimated by using different values of n_{eff} as fit parameter.

where z_{e1} and z_{e2} are the extrapolation lengths resulting from boundary effects at the front and the back of the sample[19, 20]. The effective refractive index n_e of the sample determines the value of the extrapolation lengths[16].

We created a batch of 18 ZnO samples with different thicknesses ranging from 3 µm up to 32 µm. For each of these samples we measured the spectrally resolved total diffusive transmission with an integrating sphere and a spectrometer. The total transmission for a wavelength of 532 nm is shown in Fig. 3.4a. The error bars denote the standard deviation in the measured sample thickness and of the total transmission measured at four different sample positions. From the linear fit to the data points we find the transport mean free path to be $\ell = 0.6 \pm 0.2$ µm for this wavelength.

The spectrally resolved transport mean free path is plotted in Fig. 3.4b. The gray areas indicate the error that is deduced from the measurements at different positions on the samples. For the measured spectral region the transport mean free path depends approximately linearly on the wavelength as $\ell = 0.73\lambda + 170$.

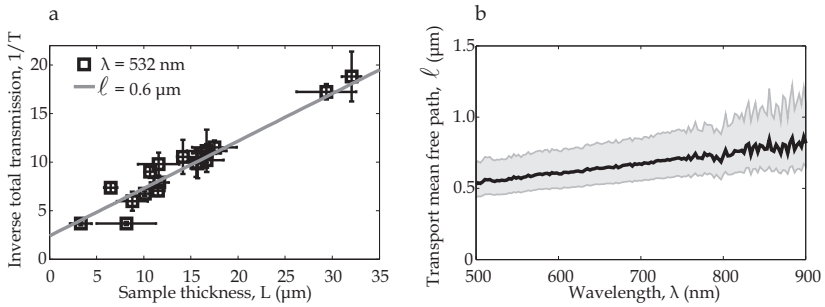

Figure 3.4: Results on total transmission measurements through ZnO slabs. **a:** Inverse total transmission through a set of 18 ZnO samples with different thicknesses for a wavelength of $\lambda = 532$ nm. From a linear fit through the data points we find the transport mean free path $\ell = 0.6$ µm. **b:** Spectrally resolved transport mean free path obtained from the total transmission measurements. For the measured spectral region the transport mean free path depends approximately linearly on the wavelength as $\ell = 0.73\lambda + 170$.

3.3 Gallium phosphide scattering lens

For the experiments in Chapters 6 and 7 we require transparent samples with a high refractive index that we use as high resolution scattering lenses. One side of these lenses need to be strongly scattering while the rest of the sample has to remain homogeneous. For our experimental realization of these lenses we choose gallium phosphide (GaP). GaP is transparent in a large part of the visible spectrum ($\lambda_0 > 550$ nm) and has a maximum refractive index of n=3.41, higher than any other transparent material in this wavelength range[21]. Electrochemically etching GaP with sulfuric acid (H_2SO_4) creates disordered macroporous networks resulting in one of the strongest scattering photonic structures ever observed[1].

3.3.1 Porous layer

We start with a 400 µm thick n-type single crystalline GaP wafer. The double side polished wafer is diced into square pieces of 9x9 mm^2. One of these pieces is sandwiched between a copper plate electrode and a teflon cover. A circular opening in the teflon cover with a radius of 3.7 mm allows exposure of the GaP to the electrolyte. We added a small droplet of silver epoxy between the copper plate electrode and the GaP to ensure good electrical contact. The mounted piece of GaP is placed into a solution of 0.5 M H_2SO_4 together with a platinum counter electrode. During the etching process, the formation of pores is initiated at a few pits in the surface. From these starting points, the pores expand into the wafer leaving behind a relatively flat and highly reflective top layer. Underneath this top layer the different etched domains approach each other and create a bulk porous structure. We use a three-step etching process[22] which creates a uniform porous layer and removes the top layer thereby directly exposing the bulk porous

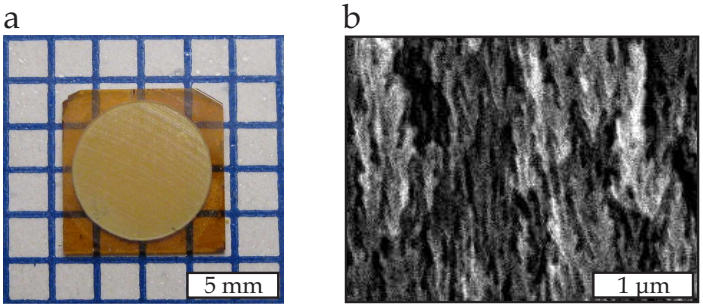

Figure 3.5: Experimental realization of a scattering lens out of gallium phosphide (GaP). **a:** Photograph of a GaP scattering lens on top of 2.5 mm paper. The center area of the GaP is electrochemically etched to create a strongly photonic porous layer. **b:** Cross section of the porous layer visualized by a scanning electron microscope. The micrograph reveals the random macroporous networks structured on a sub wavelength scale. These networks are responsible for a strong, random photonic interaction.

surface.

In the first step we apply a voltage of 11 V until an anodic charge of 7.5 C/cm^2 has passed through the sample. Next, we increase the voltage to 16 V for 900 seconds. For the last step we set the voltage back to 11 V. We continue this step until 6 C/cm^2 has passed through the GaP. Afterwards the top layer is easily washed off with some water, leaving a 2.6 µm thick porous layer.

The result of the etching process is shown in Fig. 3.5. Panel a contains a photograph of the etched wafer on top of 2.5-mm paper. The center of the wafer was exposed to the electrolyte resulting in a strongly scattering opaque layer. The edges of the wafer, which were covered during the etching, are unaffected and still transparent. In panel b we show a cross section of the porous layer. This scanning electron micrograph reveals the random macroporous networks structured on a sub wavelength scale. Due to these disordered sub wavelength pores the layer interacts very strongly with light.

3.3.2 Anti-internal-reflection coating

Due to the high refractive index contrast at the GaP/air interface, a large fraction of the light is internally reflected thereby decreasing the optical memory range. We developed an anti internal-reflection (AIR) coating to suppress these interfering reflections. The coating consists of an approximately 200 nm thick layer of amorphous silicon (Si) deposited on top of the scattering lens by electron-gun evaporation in the MESA+ cleanroom. Amorphous Si, which has a tabulated refractive index of $n = 4.8$ and an absorption length of $\ell_{\mathrm{abs}} = 0.94$ µm, is close to index matched with the GaP and strongly absorbs the light that would otherwise be internally reflected.

To test how well our AIR coating functions, we monitor the correlation of the scattered field while we rotate the beam incident on the porous layer. For this

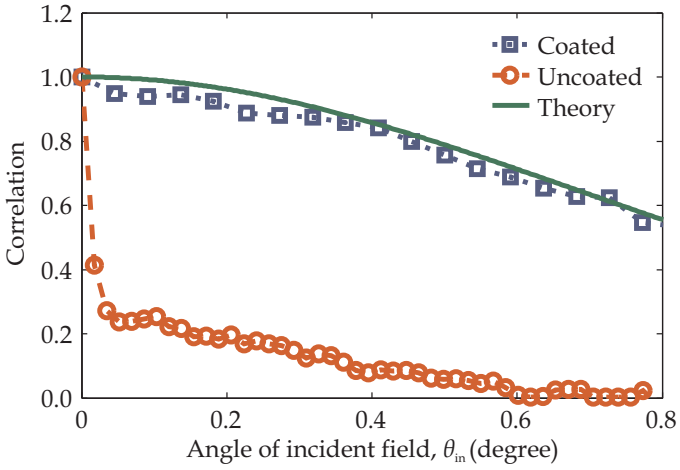

Figure 3.6: Influence of a Si anti internal-reflection coating on the correlation range of scattered light inside a GaP scattering lens when we change the angle θ_{in} under which the beam incidents. The correlation range determines the field of view of the lens and should therefore be as large as possible. In an uncoated GaP scattering lens internal reflections significantly reduce the correlations. By coating the lens with a thin layer of amorphous Si these reflections are suppressed resulting in a much larger correlation range. The green solid line represents theoretical loss of correlation due to the optical memory effect.

experiment we removed the light stop from the setup, enabling a direct recording of a speckle pattern on the CCD camera. In Fig. 3.6 we show the results for both an uncoated and a coated GaP scattering lens. For the uncoated case, a large correlation loss of 76% is seen for a small angular change of the incident field. After the initial decline, the correlation continues to decrease according to a functional form predicted by the optical memory effect[23]. When we measure the correlation loss in a coated scattering lens, we see that decrease is almost completely governed by the memory effect. The large loss seen in the uncoated lens is now reduced to a marginal 4%. The solid line represents the theoretical expected decorrelation. These results show that the AIR coating is capable of properly eliminating the unwanted internal reflections inside the GaP scattering lens.

By placing a small droplet of photoresist (Olin 908/35) on top of GaP before the Si AIR coating is deposited, is it possible to lift off an area of the coating afterwards. These areas will be used as windows to place objects onto the scattering lens. We used a sharp syringe with an opening of 150 µm to create the droplets of photoresist. The smallest droplets we managed to create with this process had a diameter in the order of 100 µm. After the Si coating is deposited, the samples are placed in a solution of acetone and submerged into an ultrasonic

bath to lift off part of the coating. In this lift off process not only the prepared areas that contained photoresist are removed, but we also observed several cracks in the coating. These cracks are in the order of several tens of micrometers and were also used as object window.

3.3.3 Imaging objects

As a test sample we have placed several objects in the window on top of the scattering lens. For the experiments in Chapter 6 we used gold nano particles. These particles were deposited by placing 5 µL of solution, which contained 50-nm diameter gold nanoparticles (BBInternational GC 50). After the solvent evaporated, a random collection of gold nanoparticled with a density of approximately 1 sphere/µm^2 was left on the object plane of the scattering lens.

The experiments described in Chapter 7 require fluorescent emitters as imaging objects. For this, we first prepare a solution containing dye doped polystyrene spheres with a diameter of $D = 62$ nm by diluting the original suspension with a factor $M = 1 \cdot 10^5$ (see Section 3.2.1). Then we place 5 µL of this solution at the object plane of the lens and let the water evaporate resulting in a random configuration of the dyed spheres.

3.4 Summary

In this chapter we discussed the fabrication and characterization of the samples that were used in our experiments.

First we described a versatile technique to create opaque disordered layers with the possibility for inclusion of nano emitters. With this method we created scattering layers out of zinc oxide pigment in several geometries, both with and without dye doped polystyrene spheres. Through a thorough spectrally resolved characterization, the layers were found to be strongly scattering with $k\ell \approx 2\pi$ over the entire measured spectrum.

Secondly we detailed the fabrication of a strongly scattering lens made out of gallium phosphide. This lens is ideal for high resolution imaging due to its high refractive index and its high transparency across a large part of the visible spectrum. By electrochemical etching we created a thin but strongly scattering layer at the surface of a homogenous wafer. An anti-internal-reflection layer was developed to suppress the high amount of light that is normally reflected at the surface of the wafer due to the high refractive index contrast. Both gold nano particles and dyed polystyrene spheres were used as test objects for the lens. These particles were placed in small object windows that were especially created in the anti-internal-reflection layer.

Bibliography

[1] F. J. P. Schuurmans, D. Vanmaekelbergh, J. van de Lagemaat, and A. Lagendijk, *Strongly photonic macroporous gallium phosphide networks*, Science **284**,

141 (1999). — p.41, 47.
[2] M. P. van Albada and A. Lagendijk, *Observation of weak localization of light in a random medium*, Phys. Rev. Lett. **55**, 2692 (1985). — p.41.
[3] P.-E. Wolf and G. Maret, *Weak localization and coherent backscattering of photons in disordered media*, Phys. Rev. Lett. **55**, 2696 (1985). — p.41.
[4] G. Maret and P. E. Wolf, *Multiple light scattering from disordered media. the effect of brownian motion of scatterers*, Zeitschrift fr Physik B Condensed Matter **65**, 409 (1987), 10.1007/BF01303762. — p.41.
[5] M. B. van der Mark, M. P. van Albada, and A. Lagendijk, *Light scattering in strongly scattering media: Multiple scattering and weak localization*, Phys. Rev. B **37**, 3575 (1988). — p.41.
[6] J. M. Drake and A. Z. Genack, *Observation of nonclassical optical diffusion*, Phys. Rev. Lett. **63**, 259 (1989). — p.41.
[7] D. S. Wiersma, P. Bartolini, A. Lagendijk, and R. Righini, *Localization of light in a disordered medium*, Nature **390**, 671 (1997). — p.41.
[8] H. Cao, Y. G. Zhao, S. T. Ho, E. W. Seelig, Q. H. Wang, and R. P. H. Chang, *Random laser action in semiconductor powder*, Phys. Rev. Lett. **82**, 2278 (1999). — p.41.
[9] H. Cao, Y. G. Zhao, H. C. Ong, S. T. Ho, J. Y. Dai, J. Y. Wu, and R. P. H. Chang, *Ultraviolet lasing in resonators formed by scattering in semiconductor polycrystalline films*, Appl. Phys. Lett. **73**, 3656 (1998). — p.41.
[10] I. Vellekoop and A. Mosk, *Universal optimal transmission of light through disordered materials*, Phys. Rev. Lett. **101**, 120601:1 (2008). — p.41.
[11] M. D. Birowosuto, S. E. Skipetrov, W. L. Vos, and A. P. Mosk, *Observation of spatial fluctuations of the local density of states in random photonic media*, Phys. Rev. Lett. **105**, 013904 (2010). — p.41.
[12] S. Smolka, A. Huck, U. L. Andersen, A. Lagendijk, and P. Lodahl, *Observation of spatial quantum correlations induced by multiple scattering of nonclassical light*, Phys. Rev. Lett. **102**, 193901 (2009). — p.41.
[13] W. Choi, Y. Park, E. G. van Putten, A. P. Mosk, and M. S. Feld, (unpublished). — p.41.
[14] T. Scientific, Technical report, Thermo Scientific (unpublished). — p.43.
[15] J. G. Rivas, D. Dau, A. Imhof, R. Sprik, B. Bret, P. Johnson, T. Hijmans, and A. Lagendijk, *Experimental determination of the effective refractive index in strongly scattering media*, Optics Commun. **220**, 17 (2003). — p.45.
[16] M. U. Vera and D. J. Durian, *Angular distribution of diffusely transmitted light*, Phys. Rev. E **53**, 3215 (1996). — p.45, 46.
[17] O. Muskens and A. Lagendijk, *Broadband enhanced backscattering spectroscopy of strongly scattering media*, Opt. Express **16**, 1222 (2008). — p.45.
[18] J. Gómez Rivas, R. Sprik, C. M. Soukoulis, K. Busch, and A. Lagendijk, *Optical transmission through strong scattering and highly polydisperse media*, Europhys. Lett. **48**, 22 (1999). — p.45.
[19] A. Lagendijk, R. Vreeker, and P. de Vries, *Influence of internal reflection on diffusive transport in strongly scattering media*, Phys Lett A **136**, 81 (1989). — p.46.
[20] J. X. Zhu, D. J. Pine, and D. A. Weitz, *Internal reflection of diffusive light in random media*, Phys. Rev. A **44**, 3948 (1991). — p.46.
[21] D. E. Aspnes and A. A. Studna, *Dielectric functions and optical parameters of Si, Ge, GaP, GaAs, GaSb, InP, InAs, and InSb from 1.5 to 6.0 eV*, Phys. Rev. B **27**, 985 (1983). — p.47.
[22] K. L. van der Molen, R. W. Tjerkstra, A. P. Mosk, and A. Lagendijk, *Spatial extent*

of random laser modes, Phys. Rev. Lett. **98**, 143901 (2007). — p.47.

[23] S. Feng, C. Kane, P. A. Lee, and A. D. Stone, *Correlations and fluctuations of coherent wave transmission through disordered media*, Phys. Rev. Lett. **61**, 834 (1988). — p.49.

CHAPTER 4

Optimal Concentration of Light in Turbid Materials

In turbid materials it is impossible to concentrate light into a focus with conventional optics. Recently it has been shown that the intensity on a dye doped probe inside a turbid material can be enhanced by spatially shaping the wave front of light before it enters a turbid medium. Here we show that this enhancement is due to concentration of light energy to a spot much smaller than a wavelength. We focus light on a dye doped probe sphere that is hidden by an opaque layer. The light ($\lambda = 532$ nm) is optimally concentrated to a focal area smaller than 0.037 μm^2. The focus can be substantially smaller than the used probe. We use a comparison between the emission and excitation intensity to show the light is concentrated to a spot below the resolution of our oil immersion microscope objective. The results are in good agreement with an optimal concentration of linearly or elliptically polarized light.

4.1 Introduction

In turbid materials such as white paint, biological tissue, and paper, spatial fluctuations in refractive index cause light to be scattered. Scattering is seen as a huge vexation in classical imaging techniques where it degrades the resolving power.[1] This decrease in resolution is caused by the fact that light carrying information about the fine spatial details of a structure has to travel further through the medium than the light carrying low spatial frequency information.[2] Due to the importance of imaging inside turbid materials, many researchers are trying to suppress turbidity.[3–8]

Although light scattering is detrimental to imaging, it is recently shown that scattering can be exploited to increase the amount of light energy deep inside turbid materials.[9] By spatially shaping the wave front of the incident light, the emission of a small dye doped probe sphere hidden inside the turbid layer was strongly enhanced proving an increase of excitation intensity at the probe position. No information was obtained about the spatial distribution of the

This chapter has been published as: E.G. van Putten, A. Lagendijk, and A.P. Mosk, J. Opt. Soc. Am. B **28**, 1200–1203 (2011)

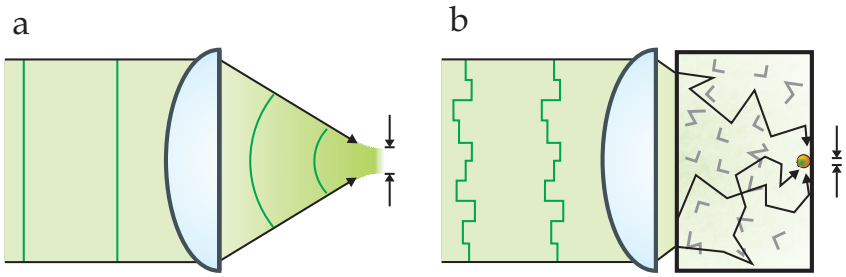

Figure 4.1: Principle of the experiment. **a:** A positive lens focusses a plane wave to a spot which is limited in size by the numerical aperture (NA) of the lens. **b:** A strongly turbid material behind the lens scatters the light so that no focus is formed. By matching the incident wave front to the scattering sample, we force constructive interference at a target position inside the sample. The light now arrives from all directions at the target position, significantly increasing the NA of the system.

excitation light. It was shown experimentally in the related field of time reversal for ultrasound[10] and microwaves[11] that a system completely surrounded by scatterers is able to focus waves down to an optimal spot whose spatial profile is equal to the intensity correlation function[12].

The goal of this chapter is to experimentally show that spatial wave front shaping can be used to focus and concentrate light to an optimal small spot *inside* a turbid material. We find that the size of the focal spot can only be understood if the vector nature of light is taken into account.

4.2 Experiment

Figure 4.1 shows the principle of our experiment. (a) Ordinarily a positive lens focusses an incident plane wave to a spot with a size that is limited by the numerical aperture (NA) of the lens. (b) A strongly turbid material behind the lens scatters the light so that no focus is formed. By matching the incident wave front to the scattering sample, we force constructive interference at a target position inside the sample. At this position multiple scattered light arrives from all angles, significantly increasing the NA of the system. We observe that the focal size is no longer limited by the original lens; an effect that was also seen in a related experiment where light was focussed far behind an opaque sample using direct feedback of the laser intensity[13]. Here the focus is created on a nano-sized fluorescent probe sphere hidden inside a strongly scattering layer by using the emission from the probe sphere as a feedback signal to synthesize the wave front.

Our experiments are performed on opaque layers of strongly scattering zinc oxide (ZnO) pigment sprayed on top of a low concentration of dye doped polystyrene spheres that will act as local intensity probes. We used probe spheres with a radius of R = 80 nm and R = 150 nm with a fluorescent emission peak at

$\lambda = 612$ nm. At the back of the sample the probes are directly visible which allows us to monitor the excitation intensity at their position. ZnO is one of the most strongly scattering materials known and shows no fluorescence in the spectral region where our probes emit. The scattering layer ranges between 7.5 ± 1 µm and 25 ± 4 µm in thickness and has a mean free path of $\ell = 0.7 \pm 0.2$ µm. By measuring the angular resolved transmission through the ZnO layers[14] we determined their effective refractive index n_{eff} to be 1.35 ± 0.15.[15, 16]

Using a wave front synthesizer, similar to the one discussed in Ref. [9], we spatially divide a monochromatic laser beam ($\lambda = 532$ nm) into up to 640 square segments of which we individually control the phase. The shaped beam is focussed onto our sample using a microscope objective (NA = 0.95). The same microscope objective is used to capture the fluorescence from a probe hidden under the scattering layer. At the back of the sample we use an oil-immersion microscope objective (NA = 1.49) to directly image both the excitation and emission light at the probe on two separate cameras. A digital feedback system that monitors the amount of fluorescence, tailors the wave front to maximize the emission of a probe sphere hidden by the scattering layer using a pixel by pixel optimization method[17] that effectively inverts the transmission matrix[18].

4.3 Results and Discussion

In Fig. 4.2 we see a typical result of the experiment. When we illuminate the sample with a focussed plane wave, we measure a low fluorescence response from a R = 150 nm probe (a) and we see a speckle pattern in the excitation light (b). Nothing in the speckle pattern reveals the position of the probe. If a shaped wave, created to maximize the fluorescent emission, is focussed onto the sample we measure an intensity enhancement of the emission (c) and we see a sharp focus of excitation light at the position of the probe (d). It is surprising to see that the dimensions of the probe sphere do not confine the focal size because the created focus is noticeably smaller than the used probe.

The radial intensity profile in the focus is shown in Fig. 4.3 together with the speckle correlation functions (SCFs) measured through both the illumination and the imaging microscope objective. The SCF is equal to the point spread function (PSF) of an optical system[19–21], thereby giving the resolution limit of the illumination and imaging optics. The SCF is defined as

$$C(\Delta x, \Delta y) \equiv \frac{\langle I(x,y) I(x-\Delta x, y-\Delta y)\rangle}{\langle I(x,y)\rangle \langle I(x-\Delta x, y-\Delta y)\rangle} - 1, \tag{4.1}$$

where $\langle \cdot \rangle$ is a spatial average over all speckles. In order to acquire the SCF one can image a random speckle pattern through both microscope objectives and calculate the autocorrelation function of these images. In practice we cross-correlated two subsequently taken images of the same speckle pattern to prevent that any noise would correlate, which would otherwise result in a false correlation value at $\Delta x = 0, \Delta y = 0$. The solid lines through the SCFs are Gaussian fits and serve as a guide to the eye.

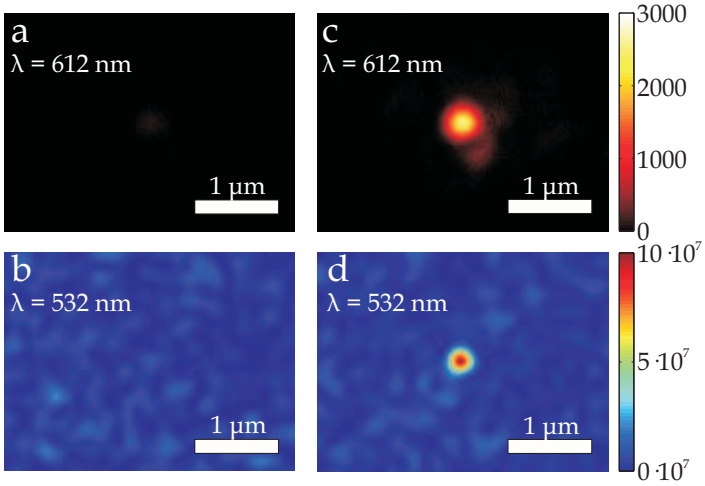

Figure 4.2: Fluorescence **(a, c)** and excitation **(b, d)** images taken at the position of a probe sphere hidden under a layer of zinc oxide. The probe sphere has a radius of R = 150 nm. The images are taken at the back of the sample where the sphere is directly visible. In panels a and b we focus a plane wave onto the sample. Scattering creates a random specular pattern of excitation light resulting in a small amount of fluorescent response of the probe sphere. In panels c and d we illuminate the sample with a shaped wave, which is created to maximize the fluorescent emission. Aside from the fluorescent emission enhancement we see a sharp focus of excitation light. All intensities are in counts/second.

The peak intensity of the focus is 32.1 times the average speckle background intensity. The measured intensity profile has a half width at half max of 108 ± 5 nm resulting in a focal area of 0.037 ± 0.003 µm^2. The size of the created spot is substantially smaller than the measured illumination SCF because the scattering layer effectively increases the NA. We also see that the measured spot is equal to the SCF of the imaging system, meaning that the formed spot must be smaller than or equal to the resolution limit of our oil immersion microscope objective.

To further investigate the focus, we compare the intensity enhancements of the emission η^{em} and excitation η^{ex}. For the excitation intensity, the enhancement is defined as the ratio between the peak intensity of the focus and the average diffusive background intensity. The diffusive background intensity is determined by averaging the intensity at the probe sphere over 100 random realizations of the incoming wave front. The emission intensity enhancement is defined as the total emission for an optimal wave front divided by the average emission during the reference measurement. In Fig. 4.4 we have plotted the measured enhancements for (a) $R = 80$ nm and (b) $R = 150$ nm probe spheres. The number of control segments was varied to create a large spread in enhancements without changing the width of the focus[13]. In some measurements the imaging microscope objective might be slightly defocussed, introducing asymmetric error bars

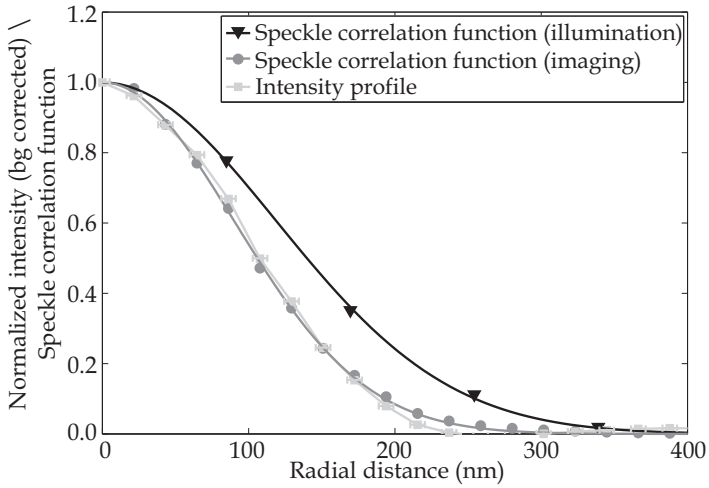

Figure 4.3: The measured radial intensity profile of the generated spot (squares) and the speckle correlation functions of the illumination (NA = 0.95, triangles) and the imaging (NA = 1.49, dots) microscope objectives. We corrected the intensity profile of the focus by subtracting the speckle background on which it resides.

in the observed excitation enhancement. In the figure we see that for the same probe size the emission enhancements η^{em} are proportional to η^{ex}. From a linear regression to the data points (solid lines) we extract the proportionality constants $C_{80} = 0.72 \pm 0.07$ and $C_{150} = 0.50 \pm 0.07$ for the R= 80 nm and the R= 150 nm probe spheres.

We now theoretically investigate the relation between η^{em} and η^{ex}. The emission power caused by a focused excitation field is proportional to the focus intensity integrated over the probe sphere volume. The reference emission power scales with the volume of the probe sphere. On the contrary, the excitation enhancement is independent of the probe volume and is determined by dividing the peak intensity of the focus by the reference speckle intensity. The enhancements for a probe sphere with radius R are therefore given by

$$\eta^{\mathrm{em}} = \int_0^R \int_0^{\pi} \int_0^{2\pi} \frac{I(\phi,\theta,r)}{I_{\mathrm{ref}} V} r^2 \sin\theta d\phi d\theta dr, \quad \eta^{\mathrm{ex}} = \frac{I_{\mathrm{peak}}}{I_{\mathrm{ref}}}, \tag{4.2}$$

so that their ratio, C_R, becomes

$$C_R \equiv \frac{\eta^{\mathrm{em}}}{\eta^{\mathrm{ex}}} = \frac{1}{V} \int_0^R \int_0^{\pi} \int_0^{2\pi} \frac{I(\phi,\theta,r)}{I_{\mathrm{peak}}} r^2 \sin\theta d\phi d\theta dr, \tag{4.3}$$

where V is the volume of the probe sphere and I/I_{peak} is the position dependent focus intensity $I(\phi,\theta,r)$ of the excitation light normalized by its peak intensity I_{peak}. We assume that the emission intensity scales linearly with the excitation intensity. From Eq. 4.3 we see that C_R can be interpreted as the overlap between the normalized intensity of the created focus and the probe sphere.

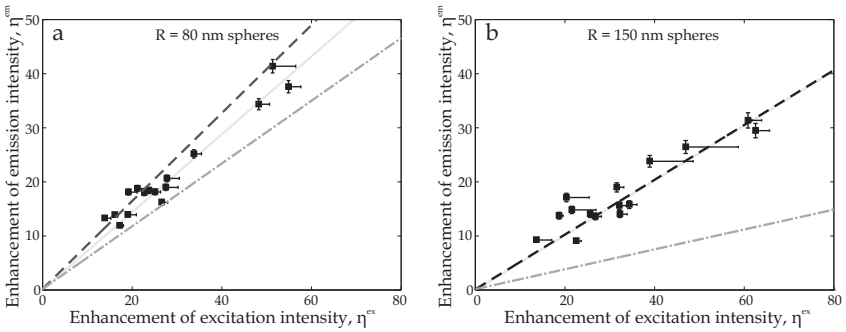

Figure 4.4: Measured enhancements of the excitation and emission intensity for spheres with a radius of **(a)** $R = 80$ nm and **(b)** $R = 150$ nm. The solid lines indicate the linear regression of the data points. We show the expected regression for light that is optimally concentrated to the center of the probe using a vector theory (dashed lines) and a scalar approximation (semi-dashed lines).

Based on the observation that the focus can be smaller than the resolution of our microscope objective we formulate the hypothesis that it has the same profile as a focus created with a high-NA lens with an acceptance angle of 90 degrees. To correctly compute the intensity profile $I(\phi, \theta, r)$ we have to take the vectorial nature of light into account as a scalar based approach underestimates the focal volume (if we neglect the vectorial nature of light the spot size is calculate using a plane wave decomposition of the contributing wave vectors[22] resulting in the semi-dashed lines in Fig. 4.4). The polarization in our focus will be a combination of linear polarizations (in general elliptic) because the feedback in our experiment is provided by the emission of the probe sphere, which has no preference for a specific polarization. By observing the development of the focus in the plane perpendicular to the sample surface we ruled out the possibility that the focus is the result of radially polarized light. As the time integrated overlap of the electric field with the fluorescent sphere is independent of the elipticity, we are free to choose the polarization as linear in our calculations. Using the focus intensity profile from Ref. [23] we find an elliptical focal area of $0.048\pi\lambda^2/n^2$. For our system where the light is optimally concentrated into the center of a polystyrene sphere ($n = 1.60$) this results in a focal area of 0.02 µm^2 with the HWHM of the two axes 110 nm and 67 nm. We use the intensity profile of the focus to calculate the overlap integral in Eq. 4.3. From these calculations we find that $C_{80} = 0.82$ for the 80 nm spheres and $C_{150} = 0.51$ for the 150 nm spheres (dashed lines in Fig. 4.4) being in good agreement with the experimental values. This data therefore supports our hypothesis and leads to the conclusion that the light is being optimally concentrated.

The area of the generated focus inside the scattering material lies far into the sub-µm^2 regime yielding exciting opportunities. In biological imaging, for example, selective illumination of fluorescent areas with high resolution is highly desirable. The position of the illuminated area could then be recovered by mea-

suring the diffusive spot of emitted light at the surface of the sample[9]. Several imaging techniques using turbidity have already been demonstrated in the last year[24–26]. These techniques would directly benefit from the generation of a small focus. The efficient light delivery to places inside scattering materials might also be used to study fundamental properties of light transport in both ordered and disordered structures. Furthermore we foresee important implications of our work to recent results in particle trapping[27] using opaque materials.

Our experimental apparatus is currently not able to detect near field effects. Expanding the setup with a scanning near field probe would allow for direct imaging of the focus. Furthermore, such a setup could use measured evanescent waves as a feedback signal to generate the focus. It would be interesting to see if evanescent waves could be coupled to a focus, which are known to influence the spatial correlations in the near field of disordered samples[28–30].

4.4 Conclusions

In conclusion, we have focused light onto fluorescent probes hidden by a strongly scattering layer of zinc oxide. We studied the shape and dimensions of the created focus. We found that the light is optimally concentrated to a focal area of at most 0.037 μm^2 which is smaller than some of the used probe spheres. A study of the intensity enhancements of both the fluorescence and excitation, performed on different probe sizes, supports the conclusion of optimal light concentration.

Bibliography

[1] P. Sebbah, *Waves and imaging through complex media* (Kluwer Academic Publishers, 1999). — p.53.

[2] A. Ishimaru, *Limitation on image resolution imposed by a random medium*, Appl. Opt. **17**, 348 (1978). — p.53.

[3] D. Huang *et al.*, *Optical coherence tomography*, Science **254**, 1178 (1991). — p.53.

[4] J. Schmitt, *Optical coherence tomography (oct): a review*, IEEE Journal of Selected Topics in Quantum Electronics **5**, 1205 (1999). — p.53.

[5] W. Denk, J. H. Strickler, and W. Webb, *Two-photon laser scanning fluorescence microscopy*, Science **248**, 73 (1990). — p.53.

[6] F. Helmchen and W. Denk, *Deep tissue two-photon microscopy*, Nat. Meth. **2**, 932 (2005). — p.53.

[7] E. N. Leith and J. Upatnieks, *Holographic imagery through diffusing media*, J. Opt. Soc. Am. **56**, 523 (1966). — p.53.

[8] Z. Yaqoob, D. Psaltis, M. S. Feld, and C. Yang, *Optical phase conjugation for turbidity suppression in biological samples*, Nat. Photon. **2**, 110 (2008). — p.53.

[9] I. M. Vellekoop, E. G. van Putten, A. Lagendijk, and A. P. Mosk, *Demixing light paths inside disordered metamaterials*, Opt. Express **16**, 67 (2008). — p.53, 55, 59.

[10] C. Draeger and M. Fink, *One-channel time reversal of elastic waves in a chaotic 2d-silicon cavity*, Phys. Rev. Lett. **79**, 407 (1997). — p.54.

[11] B. E. Henty and D. D. Stancil, *Multipath-enabled super-resolution for rf and microwave communication using phase-conjugate arrays*, Phys. Rev. Lett. **93**, 243904 (2004). — p.54.

[12] B. Shapiro, *Large intensity fluctuations for wave propagation in random media*, Opt. Lett. **57**, 2168 (1986). — p.54.

[13] I. M. Vellekoop, A. Lagendijk, and A. P. Mosk, *Exploiting disorder for perfect focusing*, Nat. Photon. **4**, 320 (2010). — p.54, 56.

[14] O. Muskens and A. Lagendijk, *Broadband enhanced backscattering spectroscopy of strongly scattering media*, Opt. Express **16**, 1222 (2008). — p.55.

[15] M. U. Vera and D. J. Durian, *Angular distribution of diffusely transmitted light*, Phys. Rev. E **53**, 3215 (1996). — p.55.

[16] J. G. Rivas, D. Dau, A. Imhof, R. Sprik, B. Bret, P. Johnson, T. Hijmans, and A. Lagendijk, *Experimental determination of the effective refractive index in strongly scattering media*, Optics Commun. **220**, 17 (2003). — p.55.

[17] I. M. Vellekoop and A. P. Mosk, *Phase control algorithms for focusing light through turbid media*, Opt. Comm. **281**, 3071 (2008). — p.55.

[18] S. M. Popoff, G. Lerosey, R. Carminati, M. Fink, A. C. Boccara, and S. Gigan, *Measuring the transmission matrix in optics: An approach to the study and control of light propagation in disordered media*, Phys. Rev. Lett. **104**, 100601 (2010). — p.55.

[19] P. H. van Cittert, *Die wahrscheinliche schwingungsverteilung in einer von einer lichtquelle direkt oder mittels einer linse beleuchteten ebene*, Physica **1**, 201 (1934), as discussed by Goodman [21]. — p.55.

[20] F. Zernike, *The concept of degree of coherence and its application to optical problems*, Physica **5**, 785 (1938), as discussed by Goodman [21]. — p.55.

[21] J. Goodman, *Statistical optics* (Wiley, New York, 2000). — p.55, 60.

[22] J. Goodman, *Introduction to fourier optics* (Roberts & Company, Englewood, 2005). — p.58.

[23] B. Richards and E. Wolf, *Electromagnetic diffraction in optical systems. ii. structure of the image field in an aplanatic system*, Proceedings of the Royal Society of London. Series A, Mathematical and Physical Sciences **253**, 358 (1959). — p.58.

[24] I. Vellekoop and C. Aegerter, *Scattered light fluorescence microscopy: imaging through turbid layers*, Opt. Lett. **35**, 1245 (2010). — p.59.

[25] S. Popoff, G. Lerosey, M. Fink, A. C. Boccara, and S. Gigan, *Image transmission through an opaque material*, Nat. Commun. **1**, 81 (2010). — p.59.

[26] C.-L. Hsieh, Y. Pu, R. Grange, G. Laporte, and D. Psaltis, *Imaging through turbid layers by scanning the phase conjugated second harmonic radiation from a nanoparticle*, Opt. Express **18**, 20723 (2010). — p.59.

[27] T. Čižmár, M. Mazilu, and K. Dholakia, *In situ wavefront correction and its application to micromanipulation*, Nat. Photon. **4**, 388 (2010). — p.59.

[28] V. Emiliani, F. Intonti, M. Cazayous, D. S. Wiersma, M. Colocci, F. Aliev, and A. Lagendijk, *Near-field short range correlation in optical waves transmitted through random media*, Phys. Rev. Lett. **90**, 250801 (2003). — p.59.

[29] A. Apostol and A. Dogariu, *Spatial correlations in the near field of random media*, Phys. Rev. Lett. **91**, 093901 (2003). — p.59.

[30] R. Carminati, *Subwavelength spatial correlations in near-field speckle patterns*, Phys. Rev. A **81**, 053804 (2010). — p.59.

CHAPTER 5

Non-Imaging Speckle Interferometry for High Speed Nanometer-Scale Position Detection

5.1 Introduction

Light is an ideal tool to perform contact free, non-destructive, and high-precision metrology.[1] For this reason optical positioning techniques have proven themselves indispensable in various branches of science and many important industrial processes, including the fabrication of semi-conductor-based circuits with features on the nanometer regime. Fast feedback is essential in these high-precision positioning systems as high frequency vibrational motion can limit the level of precision that these techniques offer.

In smooth reflecting systems, laser interferometry[2] combined with high speed detectors offers precise displacement measurements with a large bandwidth. For disordered and rough materials, where conventional laser interferometry is not applicable, several speckle based metrology techniques such as speckle photography[3, 4] and speckle interferometry[5, 6] were developed in the late 1960s and 1970s.[7] These techniques spatially image speckle patterns to offer versatile measurements of material parameters such as strain, displacement, and rotation.[8] In the pioneering experiments photographic films, which required an inconvenient development step, were used to record the speckle patterns. Nowadays, high resolution cameras enable direct digital processing of the speckle patterns.[9, 10] Although these cameras improved the detection speed of these methods significantly, they are still orders of magnitude slower than non-imaging detectors such as photodiodes. Since these fast detectors cannot provide the required spatial information they are, so far, not suitable in speckle interferometry.

Here we describe and experimentally demonstrate a non-imaging approach to displacement metrology for disordered materials. Our approach makes use of the possibility to concentrate scattered light into a focus by spatially controlling the wave front of the light that incidents onto the sample[11]. In a disordered system, which by definition lacks translational invariance, this wave front acts as an unique optical fingerprint of the illuminated part of the sample. Any displacement between the illumination and the system reduces the overlap of the fingerprint with the system, thereby inevitably decreasing the intensity in the constructed focus. This dependence opens the possibility to exploit such optical fingerprints for position detection of an illuminated sample at resolutions in the order of 1 nm. As spatial information of the scattered field is no longer required,

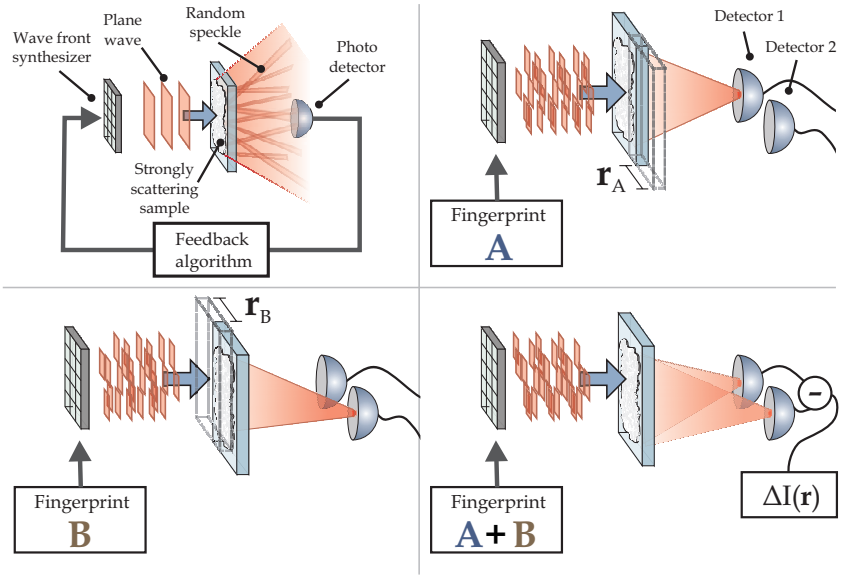

Figure 5.1: Method to detect sample displacements. Light modulated by a wave front synthesizer incidents on a scattering sample. A detector coupled to the wave front synthesizer monitors the scattered light. Two optical fingerprints are generated for two sample positions. Each of the fingerprints redirects the scattered light onto one of the detectors. The sample position $\mathbf{r}$ is then determined by illuminating the sample with a superposition of the two fingerprints and monitoring the intensity difference ΔI between the two detectors. While this figure shows a horizontal displacement, the method is more generally valid and works in all directions.

this method enables the use of fast detectors.

5.2 Principle

In Fig. 5.1 we have depicted our method to detect sample displacements. With a wave front synthesizer we spatially control the phase of a light beam. A detector behind a scattering sample combined with a feedback based algorithm finds the optical fingerprint that focusses the transmitted light onto the detector.[12] We use this system to find the fingerprints A and B corresponding to two different sample positions; $\mathbf{r}_A$ and $\mathbf{r}_B$. Fingerprint A focusses the light onto the first detector when the sample is positioned at $\mathbf{r}_A$, while fingerprint B is constructed to concentrate the light onto the second detector when the sample is at $\mathbf{r}_B$. When we now position the sample in between $\mathbf{r}_A$ and $\mathbf{r}_B$ while illuminating it with a superposition of fingerprints A and B, the sample position can be interpolated from the intensity difference of the two detectors. This method can be easily extended to detect displacements in multiple directions by generating multiple optical fingerprints at different sample positions.

5.3 In-plane sensitivity

The sensitivity of this detection method and the corresponding smallest measurable displacement $\delta\mathbf{r}$ are determined by way the intensities I_A and I_B in the two foci change under a sample displacement. The focus intensity is given by

$$I(\mathbf{r}) = \eta \langle I_{\mathrm{bg}} \rangle \left\langle |\gamma(\Delta\mathbf{r})|^2 \right\rangle, \tag{5.1}$$

where $\Delta\mathbf{r} \equiv \mathbf{r} - \mathbf{r}_0$ is the sample displacement with respect to the original position $\mathbf{r}_0$. The enhancement factor η is defined as the ratio between the optimal intensity $I(\mathbf{r}_0)$ and the ensemble averaged background intensity $\langle I_{\mathrm{bg}} \rangle$. The achievable enhancement linearly depends on the amount of degrees of freedom in the wave front. The value of $\left\langle |\gamma(\Delta\mathbf{r})|^2 \right\rangle$ accounts for the loss in overlap between the sample and the optical fingerprint under sample displacement. This overlap only equals unity for $\Delta\mathbf{r} = 0$ and is smaller for any nonzero displacement.

When the range of disorder in the sample is on a sub wavelength scale, the overlap of the optical fingerprint with the sample depends solely on the illumination optics. In our experiment the pixels of the wave front synthesizer are projected onto the back aperture of an infinity corrected microscope objective. In this geometry, the overlap for an in-plane displacement $\Delta\mathbf{r}$ is given by

$$\left\langle |\gamma(\Delta\mathbf{r})|^2 \right\rangle = \left[\frac{2J_1(k_{\max} |\Delta\mathbf{r}|)}{k_{\max} |\Delta\mathbf{r}|} \right]^2, \tag{5.2}$$

where the maximum contributing transversal wave vector $k_{\max}$ is given by the numerical aperture NA of the microscope objective, $k_{\max} = 2\pi\mathrm{NA}/\lambda$. The derivation of this overlap is found in Appendix 5.A.

The difference signal of the two detectors is

$$\Delta I(\mathbf{r}) = \eta \langle I_{\mathrm{bg}} \rangle \left(\left[\frac{2J_1(k_{\max} |\mathbf{r} - \mathbf{r}_A|)}{k_{\max} |\mathbf{r} - \mathbf{r}_A|} \right]^2 - \left[\frac{2J_1(k_{\max} |\mathbf{r} - \mathbf{r}_B|)}{k_{\max} |\mathbf{r} - \mathbf{r}_B|} \right]^2 \right). \tag{5.3}$$

The highest sensitivity of the system is found by maximizing $d\Delta I(\mathbf{r})/d\mathbf{r}$. The maximum value of this gradient lies exactly in between $\mathbf{r}_A$ and $\mathbf{r}_B$ when the distance between them is

$$|\mathbf{r}_A - \mathbf{r}_B|_{\mathrm{opt}} = 2.976/k_{\max}. \tag{5.4}$$

For these conditions the resulting sensitivity is

$$\frac{d\Delta I(\mathbf{r})}{d\mathbf{r}} = 0.92 k_{\max} \eta \langle I_{\mathrm{bg}} \rangle = \frac{5.8\mathrm{NA}\eta}{\lambda} \langle I_{\mathrm{bg}} \rangle. \tag{5.5}$$

In an experiment the signal to noise ratio $\mathrm{SNR} = \eta \langle I_{\mathrm{bg}} \rangle / \delta I$, with δI the amount of noise, determines eventually the achievable sensitivity. The smallest measurable sample displacement $\delta\mathbf{r}$ is equal to

$$\delta\mathbf{r} = \frac{\lambda}{5.8\mathrm{NA}\ \mathrm{SNR}}. \tag{5.6}$$

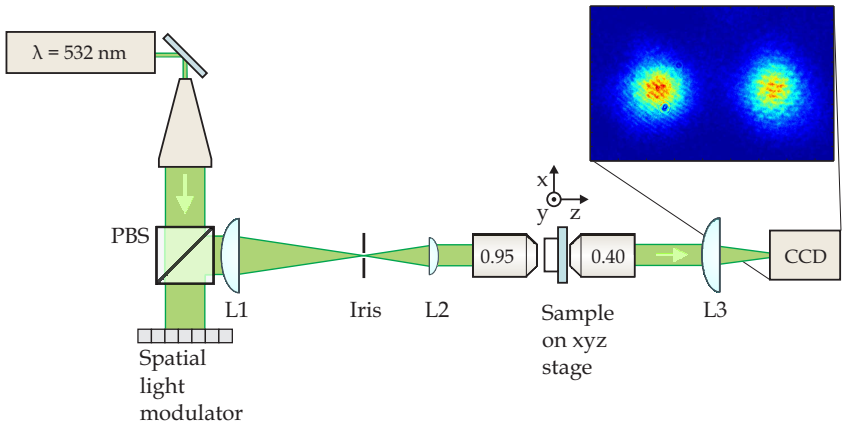

Figure 5.2: Experimental setup. Light with a wavelength of $\lambda = 532$ nm is expanded and illuminates a spatial light modulator (SLM). The light reflected from the SLM is spatially filtered and then projected onto the back pupil of a 63x microscope objective (NA = 0.95). A disordered sample, mounted onto an xyz-nano positioning stage, is placed in the focal plane of the microscope objective. At the back of the sample the transmitted light is projected onto a CCD camera. PBS; polarizing beam splitter cube; L1, L2, L3, lenses with focal distances of 200 mm, 100 mm, and 150 mm respectively. The inset shows the intensity pattern on the camera while the sample is illuminated with a superposition of two optical fingerprints.

By changing the enhancement (and with it the SNR), the wavelength, and the NA of the objective it is possible to tune the sensitivity over a wide range of distances.

5.4 Experimental implementation

To test our position detection method we built the setup that is schematically depicted in Fig. 5.2. An expanded beam from a continuous wave laser (Coherent Compass M315-100, $\lambda = 532$) illuminates a Holoeye LC-R 2500 spatial light modulator (SLM) that we use as a wave front synthesizer. A spatial filter together with a modulation scheme enables phase only modulation without any residual amplitude modulation.[13] The pixels of the SLM are projected onto the back aperture of a microscope objective, which has a specified numerical aperture (NA) of 0.95. In the focal plane of the microscope objective we have placed a strongly scattering sample on top of a high precision positioning xyz-stage (Physik Instrumente P-611.3S NanoCube). The sample is composed of zinc oxide (ZnO) powder on top of a glass cover slide (see chapter 3 for fabrication details). At the back of the sample we collect the transmitted light and image it onto a CCD camera (Dolphin F-145B). Because there is no fundamental need for a spatially imaging detector, the camera can also be replaced with two photo diodes.

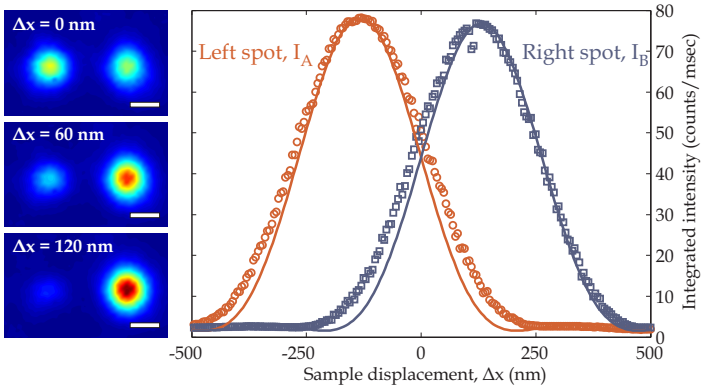

Figure 5.3: Spot intensities as function of the sample displacement. On the left there are three camera images for different values of the sample displacement Δx. As Δx increases the intensity I_A in the left spot decreases while the intensity I_B in the right spot increases. The scale bars denote 1 mm. The graph on the right shows the measured spot intensities (circles I_A, squares I_B) as function of the sample displacement. The solid lines denote the theoretical expected behavior.

5.5 Displacement measurement

Using Eq. 5.4, the optimal distance between sample position $\mathbf{r}_A$ and $\mathbf{r}_B$ in this system is calculated to be 265 nm. Without loss of generality, we consider only translations in the x-direction. The original sample position can then be defined as $x_0 = 0$ nm. The sample is translated towards $x_A = -132.5$ nm. A feedback based algorithm finds the optical fingerprint for which the scattered light is focussed on the left side of the camera. Then we position the sample at $x_B = +132.5$ nm and repeat the procedure to create a focus on the right side of the camera. The two fingerprints are superimposed on the SLM. When we move the sample back to the original position x_0, the two spots become visible on the camera.

In Fig. 5.3 the intensity in the two spots as a function of the sample displacement $\Delta x \equiv x - x_0$ is plotted together with camera images for three different values of Δx. The two lines denote the intensity behavior predicted by Eqs. 5.1 and 5.2 without free parameters. Starting from $\Delta x = 0$ where the intensity in both spots is equal, I_A and I_B change differently under sample displacement. Moving the sample in the positive x-direction results in a decreasing I_A while I_B increases for $\Delta x < x_B$. The experimental data is in good agreement with theory although the measured intensity dependence is slightly wider. This small deviation is likely to be caused by abberations in the optics that illuminate the sample.

Subtracting the intensities in both spots result in the data plotted in Fig. 5.4. For $x_A > \Delta x > x_B$ (gray area) the function is bijective resulting in a unique mapping between the difference signal and the sample position. Over a large

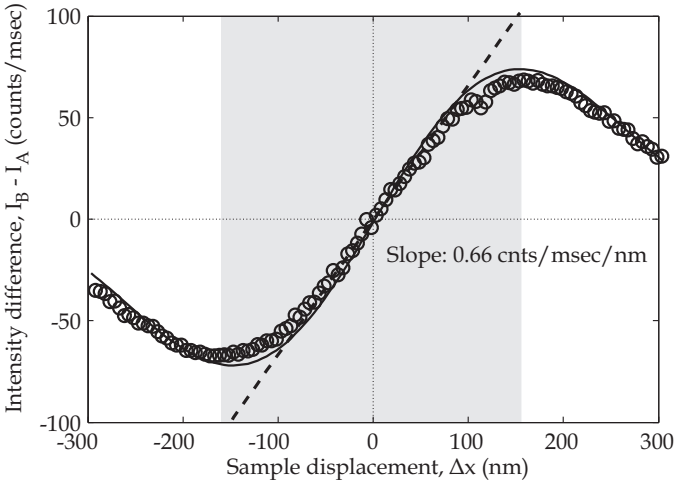

Figure 5.4: Intensity difference $I_B - I_A$ as function of the sample displacement Δx. The circles denote the measured intensity difference, while the solid line represents the theoretical intensity difference. Within the gray area the function is bijective. The steepest position of the function is found at $\Delta x = 0$. The dotted line is a linear fit to the data points close to $\Delta x = 0$. From the fit we find that the slope equals 0.66 counts/msec/nm.

distance, the function is linear and only close to the displacements $\Delta x = -x_A$ and $\Delta x = x_B$ the function starts to curve. The highest sensitivity is found at $\Delta x = 0$ where the slope has a maximum value of 0.66 counts/msec/nm, close to the theoretical limit for this system of 0.80 counts/msec/nm that we calculated using Eq. 5.5. The noise level in our setup is found to be 1.42 counts/msec, so that the displacement resolution is 2.1 nm. By increasing the enhancement factor η the sensitivity could be increased further to yield sub-nm resolution.

5.6 Conclusions

In this chapter we demonstrated a new approach to speckle interferometry that does not require any spatial recording of the speckle pattern. We use spatially controlled light to direct scattered light into designated spots. This approach opens the way for high speed metrology by use of fast non-imaging detectors such as photodiodes.

The sensitivity of the method depends solely on the spatially modulated illumination. We theoretically derived the in-plane sensitivity for the case where the modulated pixels of the wave front are focussed onto a sample. An experimental implementation of the method confirmed the theoretical prediction and resulted in a lateral displacement resolution of 2.1 nm, limited by the noise in our system. A higher resolution is possible by increasing the signal-to-noise ratio in the system by, e.g., increasing the intensity enhancement in the spots.

By employing more than two detectors and generating multiple optical fingerprints, the method can be expanded in a straightforward way to simultaneously detect displacements in multiple directions. Similarly, the optical fingerprints can also be configured to detect other sample movements, such as rotations. This flexibility makes our technique very suitable for high speed and high precision position monitoring.

5.A Overlap under sample displacement

In this appendix we calculate the overlap between a modulated field and a displaced sample. The modulated field $E(\mathbf{r})$ at a position $\mathbf{r}$ on the sample surface is written in terms of the N modulated pixels as

$$E(\mathbf{r}) = \sum_{a=1}^{N} E_a G_a(\mathbf{r}). \tag{5.7}$$

Here $G_a(\mathbf{r})$ is the Green's function that describes the propagation from pixel a towards the position $\mathbf{r}$ at the sample surface. The pixels of the modulator are imaged onto the back aperture of the microscope objective. Therefore we describe the field entering the microscope objective as plane waves with a wave vectors $\mathbf{k}$ that are projected onto the sample. In this case, the Green's function $G_a(\mathbf{r})$ is given by

$$G_a(\mathbf{r}) = \iint_{S_a} d\mathbf{k} e^{i\mathbf{k}\cdot\mathbf{r}}, \tag{5.8}$$

where the integration is over the area S_a covered by pixel a at the back aperture of the microscope objective. The wave vector $\mathbf{k}_a$ corresponds to the center of this area. As all pixels have the same size, we can write the Green's function in a more concise way by defining $\mathbf{k}' \equiv \mathbf{k} - \mathbf{k}_a$ and performing a change of variables

$$G_a(\mathbf{r}) = \iint_{S} d\mathbf{k}' e^{i(\mathbf{k}'+\mathbf{k}_a)\cdot\mathbf{r}} = e^{i\mathbf{k}_a\cdot\mathbf{r}} \mathcal{F}\{S(\mathbf{k})\}. \tag{5.9}$$

The two dimensional Fourier transform $\mathcal{F}\{S\}$ of the pixel area S acts as an envelope that defines the spatial extend in the focal plane. As a result the field is

$$E(\mathbf{r}) = \left[\sum_{a=1}^{N} E_a e^{i\mathbf{k}_a\cdot\mathbf{r}}\right] \mathcal{F}\{S\}, \tag{5.10}$$

where $\mathbf{k}_a$ denotes the wave vector in the center of pixel a.

When we move the sample over a distance $\Delta\mathbf{r}$, the original wave front only overlaps partially with the required field. The overlap is found by calculating

$$\begin{aligned}\gamma(\Delta\mathbf{r}) &= \frac{1}{I_{\text{in}}} \int_{-\infty}^{\infty} E(\mathbf{r}) E^*(\mathbf{r}-\Delta\mathbf{r}) d\mathbf{r} \\ &= \frac{1}{I_{\text{in}}} \left[\sum_{a=1}^{N} |E_a|^2 e^{i\mathbf{k}_a\cdot\Delta\mathbf{r}}\right] |\mathcal{F}(S)|^2, \end{aligned} \tag{5.11}$$

where we used Eq. 5.10 and exploited the orthogonality of the different incident plane waves in the last step.

The loss in overlap results in a decreasing focus intensity proportional to $|\gamma|^2$, which under ensemble averaging is equal to

$$\left\langle |\gamma(\Delta\mathbf{r})|^2 \right\rangle = \frac{1}{N^2} \left| \sum_{a=1}^{N} e^{i\mathbf{k}_a\cdot\Delta\mathbf{r}} \right|^2 |\mathcal{F}(S)|^4. \tag{5.12}$$

In this result we recognize the discrete Fourier transform of a plane wave for the limited range of wave vectors that are supported by the microscope objective. The term $|\mathcal{F}(S)|^4$ can be approximated to yield one inside the field of view of the microscope objective and zero outside. Under that assumption, we find in the image plane

$$\left\langle |\gamma(\Delta\mathbf{r})|^2 \right\rangle = \left[\frac{2J_1(k_{\max} |\Delta\mathbf{r}|)}{k_{\max} |\Delta\mathbf{r}|} \right]^2 , \tag{5.13}$$

which is an Airy disk with dimensions determined by the maximum contributing transversal wave vector $k_{\max}$. This maximum wave vector is directly related to the numerical aperture NA of the microscope objective as $k_{\max} = |\mathbf{k}|\,\mathrm{NA}$.

Bibliography

[1] K. J. Gåsvik, *Optical metrology* (Wiley, 2002). — p.61.

[2] N. Bobroff, *Recent advances in displacement measuring interferometry*, Meas. Sci. Technol. **4**, 907 (1993). — p.61.

[3] J. Burch and J. Tokarski, *Production of multiple beam fringes from photographic scatterers*, Optica Acta: International Journal of Optics **15**, 101 (1968). — p.61.

[4] E. Archbold, J. M. Burch, and A. E. Ennos, *Recording of in-plane surface displacement by double-exposure speckle photography*, Optica Acta: International Journal of Optics **17**, 883 (1970). — p.61.

[5] J. A. Leendertz, *Interferometric displacement measurement on scattering surfaces utilizing speckle*, J. Phys. E: Sci. Instrum. **3**, (1970). — p.61.

[6] J. Butters and J. Leendertz, *Speckle pattern and holographic techniques in engineering metrology*, Optics & Laser Technology **3**, 26 (1971). — p.61.

[7] J. W. Goodman, *Speckle phenomena in optics* (Roberts & Company, Englewood, 2006). — p.61.

[8] *Advances in speckle metrology and related techniques*, edited by G. H. Kaufmann (John Wiley & Sons, 2011). — p.61.

[9] A. Macovski, S. D. Ramsey, and L. F. Schaefer, *Time-lapse interferometry and contouring using television systems*, Appl. Opt. **10**, 2722 (1971). — p.61.

[10] O. Lekberg, *Electronic speckle pattern interferometry*, Physics in Technology **11**, 16 (1980). — p.61.

[11] I. M. Vellekoop and A. P. Mosk, *Focusing coherent light through opaque strongly scattering media*, Opt. Lett. **32**, 2309 (2007). — p.61.

[12] I. M. Vellekoop and A. P. Mosk, *Phase control algorithms for focusing light through turbid media*, Opt. Comm. **281**, 3071 (2008). — p.62.

[13] E. G. van Putten, I. M. Vellekoop, and A. P. Mosk, *Spatial amplitude and phase modulation using commercial twisted nematic lcds*, Appl. Opt. **47**, 2076 (2008). — p.64.

CHAPTER 6

Scattering Lens Resolves sub-100 nm Structures with Visible Light

The smallest structures that conventional lenses are able to optically resolve are of the order of 200 nm. We introduce a new type of lens that exploits multiple scattering of light to generate a scanning nano-sized optical focus. With an experimental realization of this lens in gallium phosphide we imaged gold nanoparticles at 97 nm optical resolution. Our work is the first lens that provides a resolution better than 100 nm at visible wavelengths.

Many essential structures in nanoscience and nanotechnology, such as cellular organelles, nanoelectronic circuits, and photonic structures, have spatial features in the order of 100 nm. The optical resolution of conventional lenses is limited to approximately 200 nm by their numerical aperture and therefore they cannot resolve nanostructure. With fluorescence based imaging methods it is possible to reconstruct an image of objects that are a substantial factor smaller than the focus size by exploiting the photophysics of extrinsic fluorophores.[1–5] Their resolution strongly depends on the shape of the optical focus, which is determined by conventional lens systems. This dependence makes them vulnerable to focal distortion by scattering. Moreover, its not always feasible to dope the object under study. Other imaging methods reach high resolution by reconstructing the evanescent waves that decay exponentially with distance from the object. Near field microscopes[6] reach a very high resolution by bringing nano-sized scanning probes or even antennas[7] in close proximity of the object to detect the evanescent field. A drawback is that the scanning probe may interact with some samples and perturb their structure. Metamaterials, which are meticulously nanostructured artificial composites, can be engineered to access the evanescent waves and image sub-wavelength structures[8] as demonstrated with superlenses[9] and hyperlenses[10] for ultraviolet light. These materials physically decrease the focus size, which will lead to improvement of linear and non-linear imaging techniques. In the especially important visible range of the spectrum, plasmonic metamate-

This chapter has been published as: E.G. van Putten, D. Akbulut, J. Bertolotti, W.L. Vos, A. Lagendijk, and A.P. Mosk, Phys. Rev. Lett. **106**, 193905 (2011)

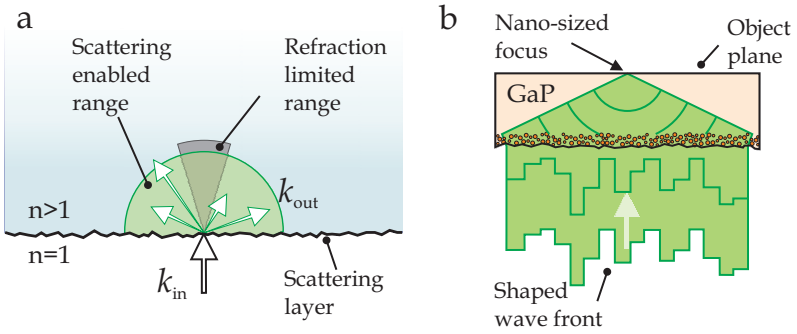

Figure 6.1: **a:** Principle of light coupling to high transversal k-vectors into a high-index material. Without scattering refraction would strongly limit the angular range to which light could be coupled. By exploiting strong scattering at the interface, incident light k_{in} is coupled to all outgoing angles k_{out} in the high index material. **b:** Schematic of a HIRES-lens that uses light scattering to achieve a high optical resolution. This HIRES-lens consists of a slab of gallium phosphide (GaP) on top of a strongly scattering porous layer. By controlling the incident wave front, a small focus is made in the object plane of the HIRES-lens.

rials can be used to produce nano-sized isolated hot spots[11–13] but the limited control over their position makes their use for imaging a challenge. So far, a freely scannable nano-sized focus of visible light has not been demonstrated.

Here we introduce a new type of lens that generates a scanning sub-100 nm optical focus. We used this lens to image a collection of gold nanoparticles at 97 nm optical resolution. The lens exploits multiple scattering of light in a porous high refractive index material to increase the numerical aperture of the system; a principle we name High Index Resolution Enhancement by Scattering (HIRES).

A HIRES-lens consists of a homogeneous slab of high-index material on top of a strongly disordered scattering layer. The disordered layer breaks the translational invariance of the interface, which enables incident light to be coupled to all propagating angles inside the high-refractive-index material as shown in Fig. 6.1a. Yet multiple scattering also scrambles the wave front creating a speckle-like pattern on the object plane that itself cannot be used for imaging. Therefore we manipulate the incident wave front in order to force constructive interference of the scattered light at a position in the object plane of our HIRES-lens. The wave front is controlled using a feedback based method[14] that is conceptually related to phase conjugation[15] and time reversal[16]. As a result, a perfectly spherical wave emerges from the porous layer and converges towards the object plane to form a sharp optical focus (Fig. 6.1b). Whereas in conventional optics (e.g. solid immersion lenses[17] or total internal reflection microscopes[18]) any inevitable surface roughness causes a distortion of the wave front and a concomitant loss of resolution, the inherent random nature makes a HIRES-lens robust for these aberrations. Any wave front error is distributed randomly over all out-

going directions, reducing the contrast but not the resolution[19]. Therefore, a HIRES lens reaches the resolution of an ideal GaP solid immersion lens, which is much better than the resolution reached by even the best GaP solid immersion lenses[17] so far. In order to use the HIRES-lens for high resolution imaging, the focus is moved around in the object plane by steering the incident wave front, directly exploiting the angular correlations in the scattered light known as the optical memory effect.[20–22] By raster scanning the focus across an object we acquire an aberration-free high-resolution image. The robust scanning high resolution focus makes the HIRES-lens excellently suited for optical imaging of nanostructures.

To demonstrate an experimental implementation of our HIRES-lens we fabricate it in gallium phosphide (GaP). GaP is transparent in a large part of the visible spectrum ($\lambda_0 > 550$ nm) and has a maximum refractive index of n=3.41, higher than any other transparent material in this wavelength range.[23] Electrochemically etching GaP with sulfuric acid (H_2SO_4) creates macroporous networks resulting in one of the strongest scattering photonic structures ever observed.[24] Using this etching process we create a $d = 2.8$ µm thick porous layer on one side of a crystalline GaP wafer. This layer is thick enough to completely randomize the incident wave front and to suppress any unscattered background light.

The memory effect allows us to shift the scattered light in the object plane of the HIRES-lens over a distance $r \approx 1.8L\lambda/(2\pi n^2 d)$ before the intensity correlation decreases to $1/e$[20], where $L = 400$ µm is the thickness of the wafer. The loss of correlation only affects the intensity in the focus (not its shape) making it easy to correct for this effect without losing resolution. Due to the high refractive index contrast on the flat GaP-air interface, a large fraction of the light is internally reflected. The reflected light interferes with the light that comes directly from the porous layer. This interference causes a background signal that is 3 times larger than the focus intensity. To strongly suppress the internal reflections we have deposited an approximately 200 nm thick anti-internal-reflection coating of amorphous silicon on the surface. The amorphous silicon is nearly index matched with the GaP and strongly absorbs the light that would otherwise be internally reflected. As a result of this layer, the background signal is reduced to only 0.04 times the focus intensity. The resulting field of view of our coated HIRES-lens is measured to be $r = 1.7 \pm 0.1$ µm in radius; 85% of the theoretical limit determined by the optical memory effect. In the center of the surface we created a small window of about 10 µm in diameter by locally removing the anti-internal-reflection coating. We use this window to place objects onto our HIRES-lens. As a test sample we have deposited a random configuration of gold nanoparticles with a specified diameter of 50 nm inside this window. More details on the fabrication of the HIRES-lens are found in Section 3.3.

An overview of our setup is shown in Fig. 6.2 (for a more detailed description of the setup see Section 6.A.1). We use a continuous wave laser with a wavelength of $\lambda_0 = 561$ nm just below the GaP bandgap of 2.24 eV (550 nm) where the refractive index is maximal and the absorption is still negligible.[23] We spatially partition the wave front into square segments of which we independently control the phase using a spatial light modulator (SLM). The SLM is first imaged onto a

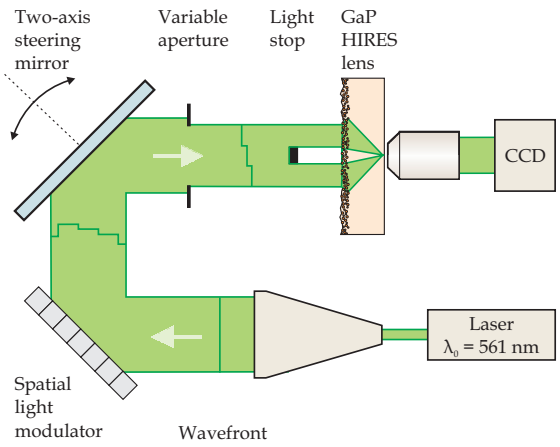

Figure 6.2: Overview of the setup. A $\lambda_0 = 561$ nm laser beam is expanded and illuminates a phase-only spatial light modulator. The modulated reflected beam is first imaged onto a two-axis steering mirror and then onto the porous surface of the GaP HIRES-lens. A variable aperture controls the extent of the illuminated area and a light stop places the setup in a dark field configuration by blocking the center of the light beam. We image the object plane onto a CCD camera using an oil immersion microscope objective.

two-axis fast steering mirror and then onto the porous surface of the HIRES-lens. With a variable aperture we set the radius $R_{\max}$ of the illuminated surface area between 0 µm and 400 µm. The visibility of the gold nanoparticles is maximized by blocking the central part of the illumination ($R < 196$ µm), placing the system in a dark field configuration. At the back of the HIRES-lens a high-quality oil immersion microscope objective (NA = 1.49) images the object plane onto a CCD camera. This objective is used to efficiently collect all the light scattered from the object plane and to obtain a reference image.

We first synthesize the wave front that, after being scattered, creates a focus in the object plane. We use light scattered from one of the gold nanoparticles in the object plane as a feedback signal to obtain a set of complex amplitudes that describe the propagation from different incident positions on the porous layer towards the nanoparticle[14], which can be interpreted as transmission matrix elements[25]. By reversing the phase of these complex amplitudes we force the light waves to interfere constructively at the exact location of the nanoparticle. The focus is moved around in the image plane by rotating every contributing k-vector over a corresponding angle. We apply these rotations by adding a deterministic phase pattern to the incident wave front. In the paraxial limit, a simple tilt of the wave front would suffice to displace the focus.[22, 26] For our high resolution focus, which lies beyond this limit, an additional position dependent phase correction is required that we apply using the SLM. The total phase ϕ re-

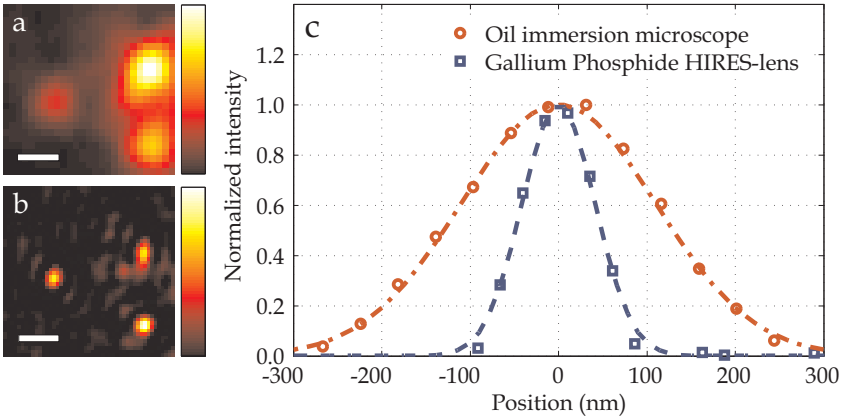

Figure 6.3: Experimental imaging demonstration with a GaP HIRES-lens. **a:** A reference image taken with conventional oil immersion microscope (NA = 1.49). The image shows a blurred collection of gold nanoparticles. The scale bar represents 300 nm. **b:** A high resolution image acquired with our GaP HIRES-lens. The image was obtained by scanning a small focus over the objects while monitoring the amount of scattered light and deconvoluted with Eq. 6.1. Details about the deconvolution can be found in Section 6.B. **c:** A vertical cross section through the center of the left sphere in panel a and panel b shows the increase in resolution. The dashed lines are Gaussian fits to the data points.

quired at position (x, y) to move the focus towards position (u_0,v_0) in the object plane is given by (see Section 6.A.2)

$$\phi(x,y)_{u_0,v_0} = -\left[\frac{xu_0}{\sqrt{x^2+L^2}} + \frac{yv_0}{\sqrt{y^2+L^2}}\right] k + \mathcal{O}(u_0^2, v_0^2).$$

The addition of this correction is essential for a proper displacement of the focus.

In Fig. 6.3 we show the imaging capabilities of the GaP HIRES-lens. First a reference image was acquired with the high-quality microscope behind the HIRES-lens (Fig. 6.3a). Because the gold nanoparticles are much smaller than the resolution limit of this conventional oil immersion microscope the image of the nanoparticles is blurred. Next we used our HIRES-lens to construct a high-resolution image. By manipulating the wave front a focus was generated on the leftmost nanoparticle. We raster scanned the focus across the object plane while we recorded the amount of scattered light. In Fig. 6.3b the result of the scan is shown. A cross section through the center of the left sphere (Fig. 6.3c) clearly shows the improvement in resolution we obtained with our HIRES-lens, confirming our expectations that the resolution of this image is far better than that of the conventional high-quality detection optics.

For a more quantitative study of the obtained resolution, we study the shape of the focus in the HIRES-lens. The radial intensity distribution of the focus is

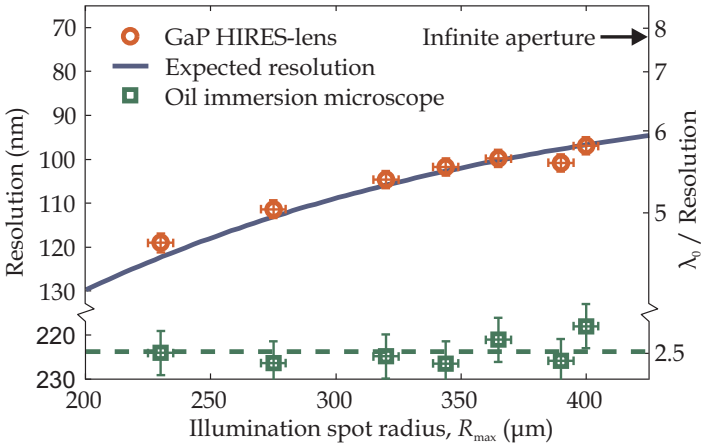

Figure 6.4: Optical resolution of a GaP HIRES-lens for different radii, $R_{\max}$, of the illumination area. Red circles: measured resolutions of the HIRES-lens. Solid blue line: expected theoretical resolution deduced from Eq. 6.1. Green squares: measured resolution of the oil immersion microscope. Dashed green line: mean measured resolution. Black arrow: expected resolution for an infinitely large illumination area.

directly calculated from a plane wave decomposition of the contributing waves,

$$I(r) = I_0 \left[k_{\max}^2 \frac{J_1(k_{\max} r)}{k_{\max} r} - k_{\min}^2 \frac{J_1(k_{\min} r)}{k_{\min} r} \right]^2 , \tag{6.1}$$

where J_1 is a Bessel function of the first kind. The minimum and maximum coupled transversal k-vectors, $k_{\min}$ and $k_{\max}$, are directly related to the inner and outer radius, $R_{\min}$ and $R_{\max}$, of the illuminated area: $k_{\max} = nk_0 \left(1 + L^2/R_{\max}^2\right)^{-\frac{1}{2}}$ (and similar for $k_{\min}$). To confirm this dependence, we imaged the objects for different values of the illumination radius $R_{\max}$. For each measurement the resolution is determined by modeling the resulting image of a single 50 nm gold nanoparticle with Eq. 6.1. Since it is hard to quantify the resolution from the width of a non-Gaussian focal shape we use Sparrow's criterion which defines the resolution as the minimal distance at which two separate objects are still discernible, see e.g. [27]. In Fig. 6.4 the measured resolution versus $R_{\max}$ is shown. As a reference we also plotted the measured resolution of the oil immersion microscope. We see that the resolution improves as we increase the illuminated area. The measured resolutions are in excellent correspondence with the expected resolution obtained from the calculated intensity profile. The resolution of the HIRES-lens is much better than the high-quality conventional oil immersion microscope. The highest resolution we measured is 97 ± 2 nm, which demonstrates imaging in the nanometer regime with visible light.

Conventional GaP solid immersion lenses (SILs) should, at least in theory, be able to reach similar resolutions as our HIRES-lens. Nevertheless, the highest reported resolution obtained with SILs is 139 nm[17] (measured at a comparable

wavelength of 560 nm), mainly limited by surface roughness and the limited coupling to high transversal wavevectors inside the lens. While quite possibly such SILs could benefit from wave front correction techniques like adaptive optics[28] to overcome the inevitable surface imperfections, the limited numerical aperture with which light is coupled into such a hemispherical lens unavoidably restricts their achievable resolution. A HIRES-lens does not suffer from this restriction as it used random scattering to couple light with high transversal wavevectors into the lens.

A GaP HIRES-lens has the potential to reach even better optical resolutions then we demonstrated, up to 72 nm. It is then possible to resolve objects placed in each others near field at distances of $\lambda_0/2\pi$. To achieve these resolutions a wider area of the scattering porous layer has to be illuminated and as a result light has to be scattered at increasingly higher angles from the porous layer. Here advances could benefit from investigations in the field of thin film solar cells where high angle scattering is beneficial for optimal light harvesting[29].

Our results promise to improve resolution in a wide range of optical imaging techniques. The robustness of a HIRES-lens against distortion and aberration, together with its ease to manufacture, makes it ideal for the imaging of fluorescent labeled biological samples or for the efficient coupling to metamaterials[9, 10] and plasmonic nanostructures[11–13]. Recent developments in spatio-temporal control of waves in disordered materials[30–32] indicate the possibility for HIRES-lenses to create ultrashort pulses in a nano-sized focus. Since a HIRES-lens is a linear and coherent optical element it is possible to combine it with interferometric methods for high precision field measurements [33, 34] and to use it for resolution improvement of a large range of imaging techniques, such as confocal microscopy, STED[2], PALM[3], and STORM[4].

6.A Experimental details

6.A.1 Apparatus

The purpose of the experimental setup is twofold. Incipiently we want it to illuminate a HIRES-lens in such a way that light scattered from the porous part of the lens focusses at a controlled position in the object plane. Secondly, we want to detect any light scattered from objects placed in the object plane of the HIRES-lens. We use a spatial light modulator combined with a two-axis steering mirror to gain spatial control over the wave front and a high resolution microscope at the back of HIRES-lens to collect the light scattered from the object plane. In Fig. 6.5 a detailed schematic of the experimental apparatus is shown. Light from a diode pumped solid state laser (Cobolt Jive, 100 mW continuous wave at 561 nm) is expanded by a 20x beam expander. With a variable aperture we control the beam size before it illuminates a phase-only Hamamatsu X10468-04 spatial light modulator (SLM) under an angle of 10 degrees. This angle is large enough to spatially separate the incident and reflected beam. At the same time the angle is small enough so that the SLM still operates within specifications. Any diffraction from the edges of the pixels on the SLM is blocked by an iris. The SLM is imaged onto a two-axis steering mirror. A polarizing beam splitter cube (PBS) combined with a quarter wave plate ($\lambda/4$) ensures that all the reflected light is directed towards the HIRES-lens. A set of relay lenses image the steering mirror onto a metal light stop to place the setup in a dark field configuration. Another lens and a microscope objective (Nikon; 20x, NA= 0.45) then demagnify the plane of the light stop onto the porous surface of the GaP HIRES-lens. At the back of the HIRES-lens we build a microscope containing an oil immersion microscope objective (Nikon; 60x, NA = 1.49). This detection path collects the light scattered from objects, by imaging the object plane of the HIRES-lens onto a CCD camera (Allied Vision Technologies Dolphin F-145B).

In order to create an initial focus in the object plane of the HIRES-lens we need to manipulate the incident wave front. We employ a feedback-based algorithm to find the wave front that forces the scattered light to interference constructively at a chosen position[14]. Once this wave front is constructed, the focus can be moved around in the object plane. This scanning does not require any additional feedback but is accomplished by adding a given spatial phase profile to the wave front using the steering mirror and the SLM.

6.A.2 Light steering

After a focus is generated it can be easily moved around in the object plane of the HIRES lens. To steer the focus to a new position, we have to add an additional phase to the incident wave front. A schematic representation of the HIRES-lens is given in Fig. 6.6. We will first derive the required phase in one dimension which then is easily generalized for the two-dimensional case.

When the initial focus is created, we force light coming from every illuminated position x on the porous layer to arrive with the same phase at position $u = 0$. If we now want to move the focus to $u = u_0$, we need to compensate the phase

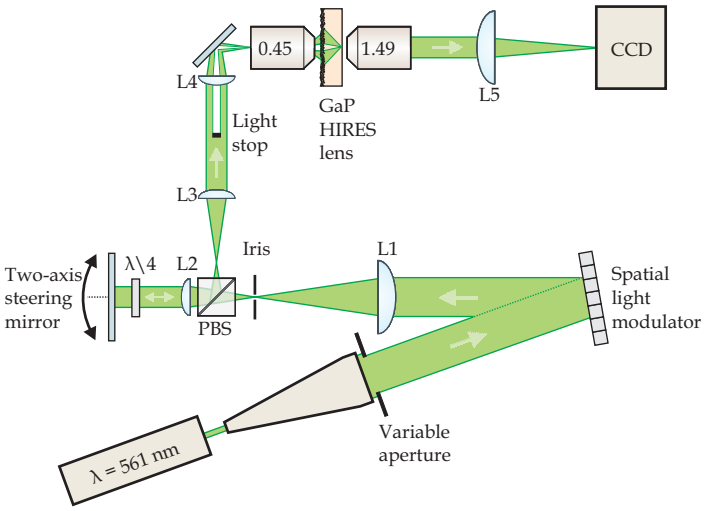

Figure 6.5: Detailed schematic of the experimental apparatus. An expanded CW laser is modulated by a phase only spatial light modulator (SLM) and a two-axis steering mirror. The iris blocks higher diffraction orders that appear due to the pixelation of the SLM. A polarizing beam splitter cube (PBS) and a quarter wave plate ($\lambda/4$) ensure that all the reflected light is directed towards the HIRES-lens. The modulated beam is first imaged onto a metal light stop and then demagnified onto the porous surface of the gallium phosphide (GaP) HIRES-lens. Light scattered from objects placed in the object plane is collected by a microscope at the back of the HIRES-lens. L1, L2, L3, L4, L5, lenses with a focal distance of 200 mm, 100 mm, 100 mm, 50 mm, and 500 mm, respectively.

for the path length difference between the original and the new position. The required phase ϕ depends on the position on the porous layer x and is given by

$$\begin{aligned} \phi(x)_{u_0} &= \left[\sqrt{(x-u_0)^2+L^2} - \sqrt{x^2+L^2}\right] k \\ &= -\frac{xu_0}{\sqrt{x^2+L^2}} k + \mathcal{O}(u_0^2), \end{aligned} \tag{6.2}$$

where L is the thickness of the homogenoous layer and k is the wave number of the light. The final result is obtained by a Taylor expansion around the original focus position $u = 0$. Generalizing Eq. 6.2 to two dimensions results in the required phase offset at position (x,y) to move the focus in the object plane towards position (u_0,v_0)

$$\phi(x,y)_{u_0,v_0} \approx -\left[\frac{xu_0}{\sqrt{x^2+L^2}} + \frac{yv_0}{\sqrt{y^2+L^2}}\right] k. \tag{6.3}$$

When the illuminated surface area is much smaller than the thickness of the HIRES-lens, the required phase reduces to a linear phase gradient. For our

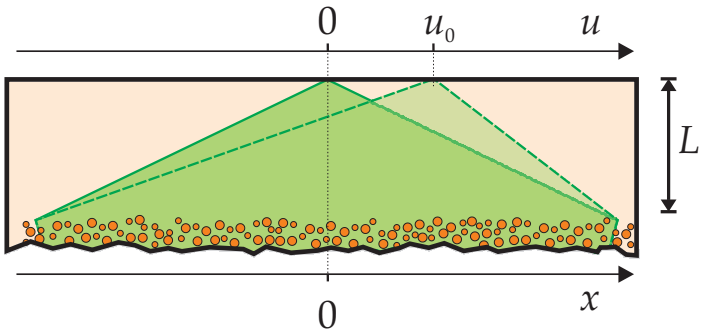

Figure 6.6: Schematic representation of light steering in a HIRES-lens. The vertical position on the porous layer is defined as x and the vertical position in the object plane of the lens is defined as u. The homogeneous part of the HIRES-lens has a thickness L. The focus, which is initially created on position $u = 0$, is scanned towards $u = u_0$.

experiments however, the illuminated surface area is of the same order as the thickness L making it necessary to use Eq. 6.3.

6.B Image processing

The shape of the focus generated in our HIRES-lens is related directly to the illuminated area of the porous layer. In the main text we show that we image gold nanoparticles with an optical resolution of 97 nm. To maximize the contrast of the nanoparticles, we blocked the central part of the illumination beam. As a result the sidelobes of our focus become more pronounced as is shown in Fig. 6.7a. By scanning this focus over the gold nanoparticles in the object plane of the HIRES-lens, we acquire an image that is the convolution of the focus with the structure (Fig. 6.7b). In this raw scan result we see the influence of the sidelobes as rings around the nanoparticles. To remove these rings, we divide the spectral spatial components of the image with the calculated spatial spectrum of the focus. The spectral contributions of the transversal k-vectors k_{trans} of both the focus intensity and the image intensity are shown in Fig. 6.7c. The maximal contributing transversal k-vector $k_{\mathrm{max}} \approx 8/2\pi$ suggest an even higher possible resolution than we obtained.

Bibliography

[1] S. W. Hell and J. Wichmann, *Breaking the diffraction resolution limit by stimulated emission: stimulated-emission-depletion fluorescence microscopy*, Opt. Lett. **19**, 780 (1994). — p.71.

[2] M. Dyba and S. W. Hell, *Focal spots of size $\lambda/23$ open up far-field florescence microscopy at 33 nm axial resolution*, Phys. Rev. Lett. **88**, 163901 (2002). — p.71, 77.

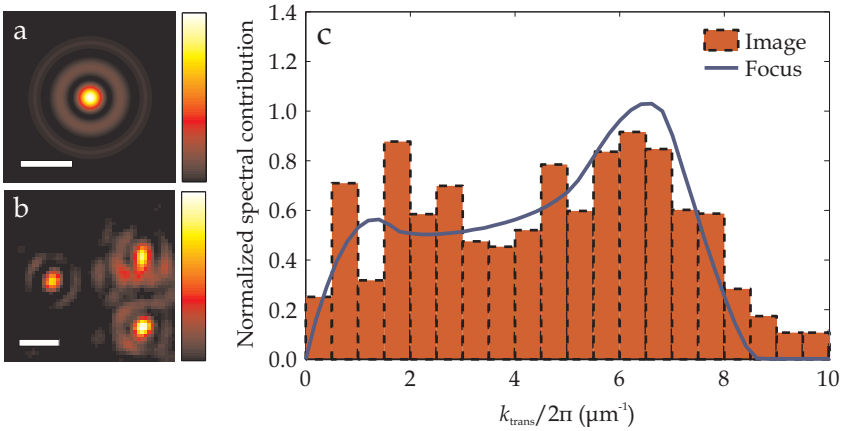

Figure 6.7: **a:** The calculated intensity profile of the focus. **b:** A collection of gold nanoparticles imaged with the GaP HIRES-lens. The image contains the scattering intensity as a function of the focus position. Due to the profile of the focus, sidelobes are visible around the nanoparticles. **c:** Spectral contributions of the transversal k-vectors k_{trans} of the calculated focus intensity (blue line) and the acquired intensity image (red bars). The scale bars represent 300 nm.

[3] E. Betzig, G. H. Patterson, R. Sougrat, O. W. Lindwasser, S. Olenych, J. S. Bonifacino, M. W. Davidson, J. Lippincott-Schwartz, and H. F. Hess, *Imaging Intracellular Fluorescent Proteins at Nanometer Resolution*, Science **313**, 1642 (2006). — p.71, 77.

[4] M. J. Rust, M. Bates, and X. Zhuang, *Sub-diffraction-limit imaging by stochastic optical reconstruction microscopy (storm)*, Nat. Meth. **3**, 793 (2006). — p.71, 77.

[5] S. W. Hell, *Far-Field Optical Nanoscopy*, Science **316**, 1153 (2007). — p.71.

[6] L. Novotny and B. Hecht, *Principles of nano-optics* (Cambridge Univ. Press, Cambridge, 2006). — p.71.

[7] H. Eghlidi, K. G. Lee, X.-W. Chen, S. Gotzinger, and V. Sandoghdar, *Resolution and enhancement in nanoantenna-based fluorescence microscopy*, Nano Letters **9**, 4007 (2009), pMID: 19886647. — p.71.

[8] J. B. Pendry, *Negative refraction makes a perfect lens*, Phys. Rev. Lett. **85**, 3966 (2000). — p.71.

[9] N. Fang, H. Lee, C. Sun, and X. Zhang, *Sub-diffraction-limited optical imaging with a silver superlens*, Science **308**, 534 (2005). — p.71, 77.

[10] Z. Liu, H. Lee, Y. Xiong, C. Sun, and X. Zhang, *Far-field optical hyperlens magnifying sub-diffraction-limited objects*, Science **315**, 1686 (2007). — p.71, 77.

[11] M. I. Stockman, S. V. Faleev, and D. J. Bergman, *Coherent control of femtosecond energy localization in nanosystems*, Phys. Rev. Lett. **88**, 067402 (2002). — p.72, 77.

[12] M. Aeschlimann, M. Bauer, D. Bayer, T. Brixner, F. J. Garcia de Abajo, W. Pfeiffer, M. Rohmer, C. Spindler, and F. Steeb, *Adaptive subwavelength control of nano-optical fields*, Nature **446**, 301 (2007). — p.72, 77.

[13] T. S. Kao, S. D. Jenkins, J. Ruostekoski, and N. I. Zheludev, *Coherent control of nanoscale light localization in metamaterial: Creating and positioning isolated*

subwavelength energy hot spots, Phys. Rev. Lett. **106**, 085501 (2011). — p.72, 77.

[14] I. M. Vellekoop and A. P. Mosk, *Focusing coherent light through opaque strongly scattering media*, Opt. Lett. **32**, 2309 (2007). — p.72, 74, 78.

[15] E. N. Leith and J. Upatnieks, *Holographic imagery through diffusing media*, J. Opt. Soc. Am. **56**, 523 (1966). — p.72.

[16] M. Fink, D. Cassereau, A. Derode, C. Prada, P. Roux, M. Tanter, J.-L. Thomas, and F. Wu, *Time-reversed acoustics*, Rep. Prog. Phys. **63**, 1933 (2000). — p.72.

[17] Q. Wu, G. D. Feke, R. D. Grober, and L. P. Ghislain, *Realization of numerical aperture 2.0 using a gallium phosphide solid immersion lens*, Appl. Phys. Lett. **75**, 4064 (1999). — p.72, 73, 76.

[18] D. Axelrod, T. P. Burghardt, and N. L. Thompson, *Total internal reflection fluorescence*, Annu. Rev. Biophys. Bioeng. **13**, 247268 (1984). — p.72.

[19] I. M. Vellekoop, A. Lagendijk, and A. P. Mosk, *Exploiting disorder for perfect focusing*, Nat. Photon. **4**, 320 (2010). — p.73.

[20] S. Feng, C. Kane, P. A. Lee, and A. D. Stone, *Correlations and fluctuations of coherent wave transmission through disordered media*, Phys. Rev. Lett. **61**, 834 (1988). — p.73.

[21] I. Freund, M. Rosenbluh, and S. Feng, *Memory effects in propagation of optical waves through disordered media*, Phys. Rev. Lett. **61**, 2328 (1988). — p.73.

[22] I. Vellekoop and C. Aegerter, *Scattered light fluorescence microscopy: imaging through turbid layers*, Opt. Lett. **35**, 1245 (2010). — p.73, 74.

[23] D. E. Aspnes and A. A. Studna, *Dielectric functions and optical parameters of Si, Ge, GaP, GaAs, GaSb, InP, InAs, and InSb from 1.5 to 6.0 eV*, Phys. Rev. B **27**, 985 (1983). — p.73.

[24] F. J. P. Schuurmans, D. Vanmaekelbergh, J. van de Lagemaat, and A. Lagendijk, *Strongly photonic macroporous gallium phosphide networks*, Science **284**, 141 (1999). — p.73.

[25] S. M. Popoff, G. Lerosey, R. Carminati, M. Fink, A. C. Boccara, and S. Gigan, *Measuring the transmission matrix in optics: An approach to the study and control of light propagation in disordered media*, Phys. Rev. Lett. **104**, 100601 (2010). — p.74.

[26] C.-L. Hsieh, Y. Pu, R. Grange, G. Laporte, and D. Psaltis, *Imaging through turbid layers by scanning the phase conjugated second harmonic radiation from a nanoparticle*, Opt. Express **18**, 20723 (2010). — p.74.

[27] E. Hecht, *Optics* (Addison Wesley Longman, Inc., 1998). — p.76.

[28] R. K. Tyson, *Principles of adaptive optics* (Academic, 1998). — p.77.

[29] E. Yablonovitch and G. D. Cody, *Intensity enhancement in textured optical sheets for solar cells*, IEEE Trans. Electron Devices **29**, 300 (1982). — p.77.

[30] J. Aulbach, B. Gjonaj, P. M. Johnson, A. P. Mosk, and A. Lagendijk, *Control of light transmission through opaque scattering media in space and time*, Phys. Rev. Lett. **106**, 103901 (2011). — p.77.

[31] O. Katz, E. Small, Y. Bromberg, and Y. Silberberg, *Focusing and compression of ultrashort pulses through scattering media*, Nat. Photon. **5**, 372 (2011). — p.77.

[32] D. J. McCabe, A. Tajalli, D. R. Austin, P. Bondareff, I. A. Walmsley, S. Gigan, and B. Chatel, *Spatio-temporal focussing of an ultrafast pulse through a multiply scattering medium*, Nat. Commun. **2**, 447 (2011). — p.77.

[33] W. Wang, S. G. Hanson, Y. Miyamoto, and M. Takeda, *Experimental investigation of local properties and statistics of optical vortices in random wave fields*, Phys. Rev. Lett. **94**, 103902 (2005). — p.77.

[34] S. Zhang and A. Z. Genack, *Statistics of diffusive and localized fields in the vortex core*, Phys. Rev. Lett. **99**, 203901 (2007). — p.77.

CHAPTER 7

Speckle Correlation Resolution Enhancement

7.1 Introduction

Fluorescence microscopy has proven itself indispensable in the biological sciences[1]. The versatility of labeling target proteins with fluorescent dyes opens ways to visualize specific structures at a subcellular level. Due to the diffraction limit however, conventional lens based systems are not capable of visualizing structures that are smaller than roughly 200 nm. With a specific subset of dyes, that allow for an efficient stimulated depletion, the diffraction limit can be circumvented to yield sub-100 nm resolution.[2–6] However, due to stringent biochemical requirements for specific labeling of organelles, such dyes are not always suited.

A gallium phosphide (GaP) HIRES-lens is capable of offering sub-100 nm optical imaging resolution[7] as was demonstrated in the previous chapter. In that experiment the wave front of the illumination beam was spatially modulated to create a high resolution scanning spot out of the normally speckled transmission. To find the wave front that generates this spot an initial reference measurement is required. Such an approach is less suitable to image fluorescent objects as the dyes experience additional bleaching during the reference measurement. Furthermore, the available field of view is small; of order of the memory range. A much wider field is desired for imaging of cells.

In this chapter we introduce a novel imaging technique for scattering lenses that does not suffer from the aforementioned limitations while it still profits from the resolution enhancement. We name this new technique, which exploits correlations in speckle illumination, Speckle Correlation Resolution Enhancement (SCORE). We first detail the principle of SCORE and show how it is used to retrieve the autocorrelation of the object under study. Then we describe the algorithm that recovers the original object by inverting the autocorrelation using trivial information about the object, such as non-negativity. Both these steps are supported by simulations. To experimentally demonstrate SCORE, we use this technique to acquire high resolution wide-field images of fluorescent nano spheres that reside in the object plane of a GaP HIRES-lens. The last part of this chapter is dedicated to these results.

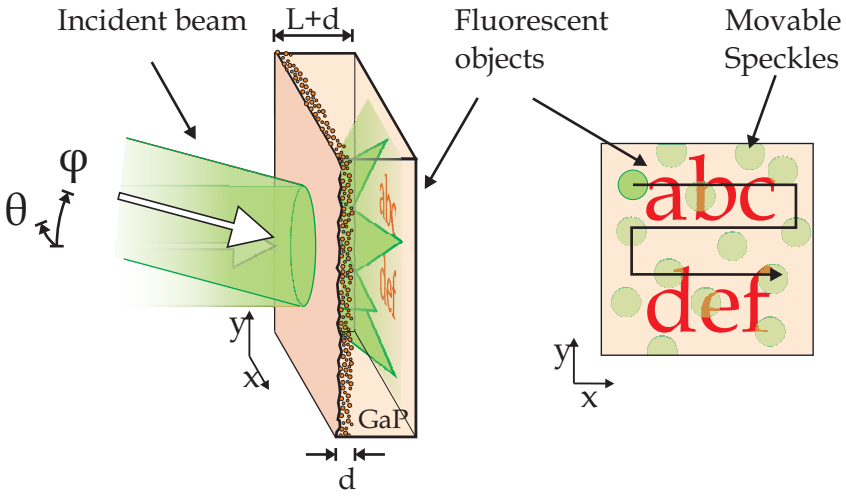

Figure 7.1: Geometry of the SCORE experiment. A beam of coherent light illuminates the scattering porous layer of a GaP HIRES-lens. At the object plane of the lens a speckle pattern is formed. The inset shows a detail of the object plane on which fluorescent objects are placed; in this case a set of letters. By tilting the incident beam over an angle, the speckle pattern is scanned across the objects.

7.2 Retrieving the autocorrelation of an object

The geometry of the experiment is shown in Fig. 7.1. A two dimensional fluorescent object $O(x, y)$ is placed in the object plane of a GaP HIRES-lens. A beam of coherent light incidents onto the porous side and creates a speckled intensity pattern $S(x, y)$ that illuminates random positions of the object. Each speckle by itself is a high resolution focus that can be up to a factor $n = 3.4$ times smaller than the diffraction limit in air. Up to now, the dense random illumination pattern prevents these speckles to be directly used for high resolution imaging as it is impossible to resolve them outside the HIRES-lens.

The optical memory effect[8, 9] enables the speckle pattern to be translated in the object plane by tilting the incident beam over an angle θ. As the inset shows, the speckles can be two dimensionally scanned over the objects. Although the speckles cannot be resolved, it is still possible to record the total amount of emitted fluorescent intensity from the object. Here we show, for the first time, that the autocorrelation function of the object can be retrieved from this limited amount of information.

For conciseness of notation we consider in the derivations a one dimensional case. A generalization of the results into two dimensions is then straightforward.

7.2.1 Theoretical description

The total emitted fluorescent intensity I as function of a shift Δx of the speckle pattern is written as a

$$I(\Delta x) = \int_{-\infty}^{\infty} dx\ O(x)S(x - \Delta x). \tag{7.1}$$

Due to the random nature of the speckle pattern, the spatial function $I(\Delta x)$ does not resemble anything close to the original object. Nevertheless, a lot of information can be retrieved from the seemingly random pattern by looking to the autocorrelation of the function.

Before we proceed to calculate the autocorrelation we recall the definitions of a convolution and a cross correlation between two functions $f(x)$ and $g(x)$. We follow the convention of Ref. [10] in defining a convolution as

$$[f * g](\Delta x) \equiv \int_{-\infty}^{\infty} dx\ f(x)g(\Delta x - x), \tag{7.2}$$

which is often shortened to $f * g$ with the variable x implicit. A cross correlation of two functions, denoted by the $\star$ symbol, is a special case of a convolution

$$[f \star g](\Delta x) \equiv [f^*(-x) * g](\Delta x) = \int_{-\infty}^{\infty} dx\ f^*(x)g(x + \Delta x), \tag{7.3}$$

where f^* is the complex conjugate of f. Just as with a convolution, a cross correlation is often abbreviated to $f \star g$.

The total emitted fluorescent intensity $I(\Delta r)$ defined in Eq. 7.1 is now written more concisely as a convolution product

$$I(\Delta x) = [O * S(-x)](\Delta x). \tag{7.4}$$

In this notation, using the associative property of the convolution, it becomes straightforward to show that the autocorrelation $[I \star I](\delta x)$ of the measured fluorescence intensity is equal to

$$\begin{aligned}[I \star I](\delta x) &= [(O * S(-x)) \star (O * S(-x))](\delta x) \\ &= [(O \star O) * (S(-x) \star S(-x))](\delta x) \\ &= [(O \star O) * (S \star S)](\delta x),\end{aligned} \tag{7.5}$$

where we used the fact that $S \in \mathbb{R}$ because we consider the speckle intensity. Explicitly the autocorrelation is written as

$$[I \star I](\delta x) = \int_{-\infty}^{\infty} d\Delta x \int_{-\infty}^{\infty} dx\ O^*(x)O(x + \Delta x) \int_{-\infty}^{\infty} dx'\ S^*(x')S(x' + \delta x - \Delta x). \tag{7.6}$$

From this result we see that the autocorrelation of $I(\Delta x)$ is equivalent to the autocorrelation of the object convoluted with the autocorrelation of a speckle

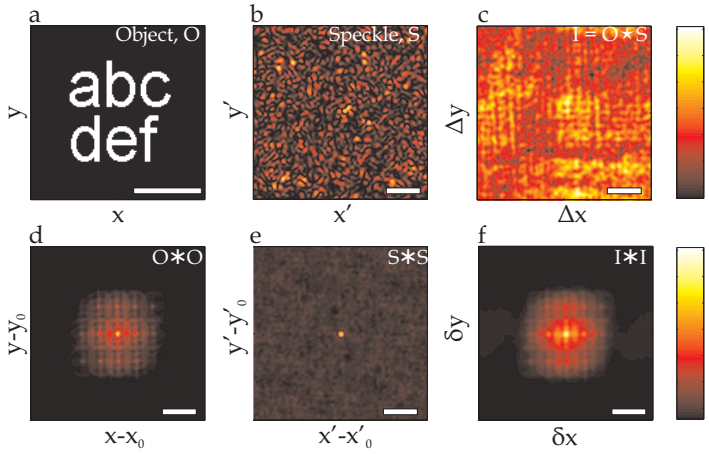

Figure 7.2: Simulated results demonstrating the retrieval of an object's autocorrelation by scanning a speckle pattern across the object. **a:** Original fluorescent object, $O(x, y)$. **b:** Speckle pattern $S(x, y)$ that is scanned across the object. **c:** Convolution $I(\Delta x, \Delta y)$ between the object and the speckle pattern. **d:** Autocorrelation of the object shown in panel a. **e:** Autocorrelation of the speckle pattern. **f:** Autocorrelation of the intensity $I(\Delta x, \Delta y)$ averaged over 1000 different realizations of the speckle pattern. By comparing panels d, e, and f it is seen that $[I \star I](\delta x, \delta y)$ equals the autocorrelation of the object O at the resolution of typical speckle size. The scale bars represent 50 pixels.

pattern. Due to the random nature of speckle, its autocorrelation is sharply peaked and the width of the peak is determined by the size of the speckles[11]. The function $[I \star I](\delta x)$ is therefore equivalent to the objects autocorrelation at the resolution of the average speckle size.

In conclusion we see that this proposed approach makes it possible to retrieve the autocorrelation of the object at a resolution given by the size of the speckles at the position of the object, which in case of a HIRES lens is far below the resolution of the detection optics.

7.2.2 Simulation

In Fig. 7.2 we show the results of a simulation to elucidate the retrieval of the autocorrelation of an object. In panel a and b the object and a speckle pattern are plotted. The convolution of the two is plotted in panel c. In the lower panels we plotted the autocorrelations of the object (d) and the speckle pattern (e) together with the autocorrelation function of I (f). The autocorrelation of the speckle patten, $S \star S$, contains only one sharp peak with a width equal to the typical speckle size. As a result, $I \star I$ represents the autocorrelate of the object, $O \star O$, at the resolution of the speckles.

The speckle pattern in Fig. 7.2b only has a finite extent. Therefore the au-

tocorrelation of this speckle pattern contains not only one sharp peak but also some remaining structure away from the center, which influences the quality of the retrieved autocorrelation $[I \star I](\delta x)$. To improve the quality of the autocorrelation, one can measure the autocorrelation for different realizations of the speckle pattern and average each of them. The retrieved function $[I \star I](\delta x)$ in Fig. 7.2f is the result of an averaging over 1000 different realizations of the speckle pattern.

7.2.3 Influence of speckle decorrelation

Until now we implicitly assumed that a speckle pattern preserves its spatial shape while it is being translated. However, when the speckle pattern is shifted in a HIRES-lens it will slowly lose correlation due to the finite angular range of the memory effect. Therefore, when the shift is not small compared to the memory range in Eq. 2.51, the shifted speckle pattern is actually different from the unshifted one. To calculate how the finite memory range affects the retrieval of the autocorrelation $[I \star I](\delta x)$ we have a closer look at the cross correlation that arises in Eq. 7.6 between the original speckle intensity pattern $S(x)$ and the shifted version $S_{\delta x}(x) \equiv S(x + \delta x)$ of the speckles

$$\int_{-\infty}^{\infty} dx'\ S^*(x')S(x' + \delta x - \Delta x) = [S \star S_{\delta x}](-\Delta x), \tag{7.7}$$

and connect it to the $C^{(1)}_{aba'b'}$ correlation function that was discussed in Section 2.6.2.

In order to move the speckle pattern over a distance δx we have to tilt the incident beam over an angle θ equal to

$$\delta x = \frac{L \tan\theta}{n}, \tag{7.8}$$

where n is the refractive index and L the thickness of the of the homogenous GaP. Under the small angle approximation, the distance δx can be expressed in terms of the transverse momentum difference $\Delta q_a = k_0 \sin\theta$ of the incident beam

$$\delta x = \frac{L}{k}\Delta q_a, \tag{7.9}$$

where $k = nk_0$ is the wave number inside the GaP slab. For a given shift δx the intensity-intensity speckle correlation function spatially depends on Δx, which in a similar way can be written in terms of the transverse momentum difference Δq_b inside the GaP slab

$$\Delta x = \frac{L}{k}\Delta q_b. \tag{7.10}$$

In section 2.6.2 we calculated the short-range intensity-intensity correlation $C^{(1)}_{aba'b'}$ in terms of Δq_a and Δq_b. We can now use Eq. 7.9 and Eq. 7.10 to find an expression for the cross correlation

$$[S \star S_{\delta x}](-\Delta x) = g\big((\delta x - \Delta x)\, k/L\big) \left[\frac{\delta x\ kd/L}{\sinh \delta x\ kd/L}\right]^2, \tag{7.11}$$

where d is the thickness of the scattering layer and g is a geometrical function that depends on the illumination. For a circular illuminated area with a width W smaller than L, the function is given by Eq. 2.52 and is equal to

$$g\big(\,(\delta x - \Delta x)\,k/L\big) = \left(\frac{2J_1\left(|\delta x - \Delta x|\;\; kW/L\right)}{|\delta x - \Delta x|\;\; kW/L}\right)^2. \tag{7.12}$$

which is an Airy pattern with a width equal to the average speckle size. In the limit where $W/L \ll 1$ the function g becomes

$$g\big(\,(\delta x - \Delta x)\,k/L\big) = \left(\frac{2J_1\left(|\delta x - \Delta x|\;\; k\sin\theta\right)}{|\delta x - \Delta x|\;\; k\sin\theta}\right)^2, \tag{7.13}$$

with $\theta = \arctan\left(W/2L\right)$.

By substituting Eq. 7.11 into Eq. 7.6 we find the retrievable autocorrelation taken into account the limited angular memory effect

$$\left[I \star I\right](\delta x) = \Big(\left[O \star O\right](\Delta x) * g(\Delta x k/L)\Big)\left[\frac{\delta x\;\, kd/L}{\sinh \delta x\;\, kd/L}\right]^2. \tag{7.14}$$

Here we see that the resolution of the recovered autocorrelate is still only limited by the average speckle size and unaffected by the memory effect. The memory range only enters the equation as a factor that decreases the value of $\left[I \star I\right](\delta x)$ for large values of δx.

7.2.4 Wide field measurement

In the previous subsection we calculated the autocorrelation $\left[I \star I\right](\delta x)$, taken into account the finite angular memory range. When the displacement is small so that $\delta x \ll L/kd$, the last term in Eq. 7.14 is approximately equal to one. For larger displacements this term converges to zero thereby restricting the range over which we are able to recover $O \star O$. In order to perform a wide field measurement of the objects autocorrelation, we employ a camera to monitor the fluorescence. In this subsection we explain how such a wide field measurement works.

An optical imaging system projects the object plane of the HIRES-lens onto a camera. These conventional imaging optics cannot resolve structures smaller than a distance R equal to the resolution. Therefore we divide the camera image up into N individual areas a_n of $R \times R$. For each of these areas the fluorescent intensity $I_n(\Delta x)$ is determined while the speckle pattern is scanned over the objects that reside in the area a_n. Due to this local detection, we can pretend for each intensity function I_n that

$$O_n(x) = \begin{cases} O(x) & \text{for } x \in a_n \\ 0 & \text{otherwise.} \end{cases}$$

The maximum area of an autocorrelation that is nonzero, is twice the size of the original object. Therefore, to measure $O_n \star O_n$ the speckle pattern only has

to stay correlated over an area of $2R \times 2R$. From the last term in Eq. 7.14 we find that this constraint is met when

$$2R \leq L/kd. \tag{7.15}$$

In our GaP HIRES lenses L/kd is in the order of 4 µm. With normal imaging optics it is therefore straightforward to achieve a resolution that is high enough to fulfill this condition.

From each retrieved autocorrelation $[I_n \star I_n](\delta x)$ the original object O_n can be retrieved as we will show in the next section. To form a wide field image, these recovered objects are patched together.

7.3 Recovering an object from its autocorrelation

In general it is impossible to recover an object from its autocorrelate since the calculation of an autocorrelation is a lossy operation. An autocorrelate preserves only the magnitude of the spatial Fourier spectrum while all phase information is lost. This loss is seen by calculating the Fourier transform of an autocorrelation using the convolution theorem[10]

$$\mathcal{F}\{O \star O\} = \mathcal{F}\{O\}\,\mathcal{F}\{O\}^* = |\mathcal{F}\{O\}|^2 . \tag{7.16}$$

In practice however, it is often possible to uniquely infer the lost phase information for objects that have a dimensionality higher than one[12–14]. Fienup[15, 16] pioneered such methods for phase retrieval and demonstrated several iterative algorithms that are capable of retrieving an object from the magnitude of the spatial Fourier spectrum by using a priori information of the object, such as being real or non-negative.[17] These algorithms were quickly adopted in a wide variety of fields, such as astronomy and crystallography[18, 19]. A review by Millane[20] provides an excellent introduction into the subject of phase retrieval and the following discussion is based on this paper.

7.3.1 Phase retrieval algorithms

The basics of Fienup's phase retrieval algorithms are shown in Fig. 7.3. The algorithm starts with an initial guess $g_1(x, y)$ of the object. When a low resolution image of the object is available, this image is a logical choice for the initial guess. Otherwise, a completely random pattern can be used to start the algorithm. The initial guess is entered into an algorithm that performs the following four steps at its k^{th} iteration

$$\begin{aligned} G_k(u,v) &= \mathcal{F}\{g_k(x,y)\} \\ \theta_k(u,v) &= \arg\left(G_k(u,v)\right) \\ G'_k(u,v) &= |\mathcal{F}\{O(x,y)\}|\, e^{i\theta_k(u,v)} \\ g'_k(x,y) &= \mathcal{F}^{-1}\left\{G'_k(u,v)\right\}, \end{aligned}$$

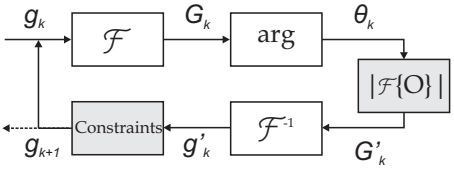

Figure 7.3: Block diagram for an iterative phase recovery algorithm. $\mathcal{F}\{\}$: Fourier transform. Arg: argument. $|\mathcal{F}\{O\}|$: Magnitude of the measured spatial spectrum of the object O, which is retrieved from the autocorrelation of O. $\mathcal{F}\{\}^{-1}$: inverse Fourier transform. Constraints: real space constraints to calculate g_{k+1} out of g'_k.

where we use the information from the measured autocorrelation in the third step.

At this point the algorithm requires real space constraints on the object. In our case, where we look at fluorescence, the object has to be positive. We define a set Γ that contains all the points in g'_k violating this constraint; in our case the points with a negative value. There are multiple ways to implement this constraint into the algorithm. The first implementation is known as the the 'Error-Reduction' algorithm and sets

$$g_{k+1}(x,y) = \begin{cases} g'_k(x,y) & \text{for } (x,y) \notin \Gamma \\ 0 & \text{for } (x,y) \in \Gamma. \end{cases}$$

Another possible implementation is called the 'Hybrid Input-Output' algorithm and defines

$$g_{k+1}(x,y) = \begin{cases} g'_k(x,y) & \text{for } (x,y) \notin \Gamma \\ g_k(x,y) - \beta g'_k(x,y) & \text{for } (x,y) \in \Gamma, \end{cases}$$

where β is a feedback parameter. When $g_{k+1}(x,y)$ is calculated it can be used as the starting point for the $(k+1)^{\text{th}}$ iteration. A single iteration of these algorithms takes only a couple of microseconds on a modern desktop computer allowing for a complete inversion of an autocorrelation within a minute.

The convergence of the algorithms is monitored by calculating the squared error E_k^2 between the autocorrelation of the retrieved image with the measured one

$$E_k^2 = \left[|\mathcal{F}\{g'_k\}| - |\mathcal{F}\{O\}| \right]^2. \tag{7.17}$$

We found the best convergence by starting with the Hybrid Input-Output algorithm and gradually lowering β in small steps from 2 to 0. Then a couple of iterations with the Error-Reduction algorithm reduces any residual noise from the image.

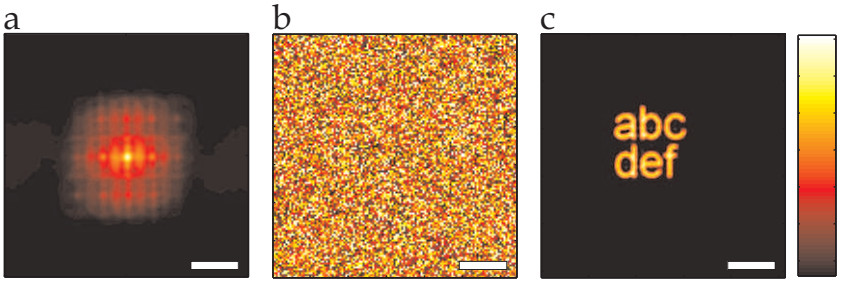

Figure 7.4: Retrieval of a simulated object from its autocorrelate. **a:** The autocorrelation of an object that is acquired with the speckle correlation method detailed in section 7.4 . The original object is shown in Fig. 7.2a and contains the letters 'abcdef'. **b:** Initial guess g_1 of the object that is used to start the algorithm. This guess is a completely random pattern with values between 1 and 0. **c:** The result of the inversion using an iterative algorithm. Apart from a positional shift, the image containing six letters is excellently reconstructed having an overlap of 67% with the original object. The missing overlap is only caused by the limited resolution of the reconstructed image. The resolution of the image is given by the average speckle size with which the data in panel a was acquired. The scale bars represent 50 pixels.

7.3.2 Simulation

In Fig. 7.4 the results are shown for an inversion of an autocorrelate. The autocorrelate we use is plotted in Fig. 7.4a and is equal to the simulated result from section 7.4 (see also Fig. 7.2f). We start with a completely random initial guess, which is shown in Fig. 7.4b. The 'Hybrid Input-Output' algorithm is employed for β ranging from 2 to 0 in steps of 0.1. For each value of β the algorithm runs 100 iterations. Finally, 1000 iterations with the 'Error-Reduction' algorithm are used to arrive at the final result, which is plotted in Fig. 7.4c. Apart from a positional shift, the algorithm perfectly reconstructed the original object blurred by the average speckle size.

The fact that the reconstructed image is shifted is caused by the centrosymmetric nature of an autocorrelation. The objects $O(x, y)$, $O(x + x_0, y + y_0)$ and $O(-[x + x_1]), -[y + y_1])$, with x_0, x_1, y_0, and y_1 real constants, all produce the exact same autocorrelate. Therefore the autocorrelation lacks information about the exact position and a possible inversion in the origin. A low resolution image of the object can be employed to find the position and orientation.

7.4 Experiment

For an experimental demonstration of SCORE we prepared a GaP HIRES-lens containing a low density of dye doped fluorescent spheres in the object plane. The spheres have a diameter of 100 nm and have their emission peak at 612 nm.

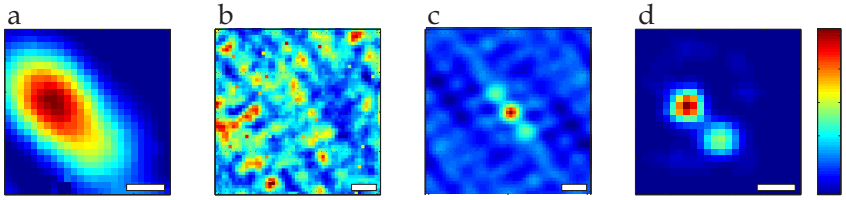

Figure 7.5: Experimental SCORE results on a subcell of the total recorded fluorescent image. **a:** Average fluorescent intensity at the resolution of the conventional imaging optics. **b:** Integrated fluorescent intensity in the subcell as function of speckle displacement. **c:** Autocorrelation of the image plotted in panel b. **d:** Inversion result of the autocorrelation in panel c. This result is an image of the same object as imaged in panel a but at a much higher resolution only by the size of the speckles. The scale bars represents 300 nm.

Details on the fabrication of the lens and the preparation of the spheres are discussed in chapter 3.

The experimental apparatus is based on the setup described in chapter 6 and adjusted on a few minor points to make it suitable for fluorescence measurements. The CCD camera is replaced by a sensitive electron multiplying CCD camera (Andor Luca DL-658M). An air microscope objective (Zeiss infinity corrected 63x, NA = 0.95) images the object plane of the HIRES-lens onto the camera. Multiple bandpass filters (Semrock FF01-620/52-25) in front of the camera ensure that only the fluorescent emission light is detected. The spatial light modulator in the illumination path is only used to generate a parabolic phase correction required for a proper displacement of the scattered light inside the HIRES-lens as was discussed in section 6.A.2.

The optical memory effect allows us to translate the speckle pattern over approximately an area of 2×2 µm^2 without significant loss of correlation. The speckles inside the HIRES-lens are expected to be in the order of 100 nm and determine the resolution at which we can retrieve the autocorrelations. It does not make sense to make the scan steps much smaller than the average speckle size. However, oversampling helps to reduce the noise in our measurements. The speckle pattern is therefore scanned with steps of 40 nm over a range of 2 µm in two dimensions, requiring 2500 measurements per scan. For each measurement the full camera image is stored, which allows us to retrieve the object at any position of the captured field of view.

7.5 Results

After all the scans are measured, the data is ready to be processed. Because the speckle pattern is only scanned over a limited range, we have to divide every camera image up into smaller subcells. The dimensions of these subcells can be at most half the scan range in order to capture the whole autocorrelation of the

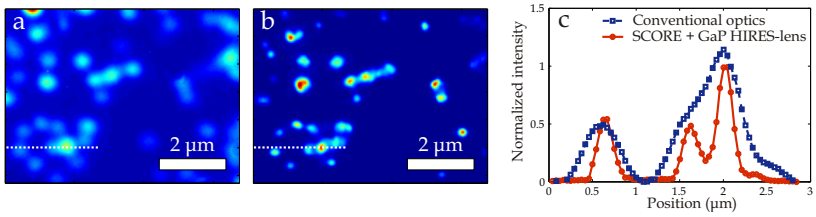

Figure 7.6: Comparison of a wide field image acquired with conventional optics and with a GaP HIRES-lens using SCORE. **a:** Image taken with conventional optics (NA = 0.95). **b:** Image taken with a GaP HIRES-lens using SCORE. **c:** Intensity of the images in panels a and b at the position of the dotted white lines. To acquire the SCORE image we used a threshold. Every sphere that has an average intensity lower than this threshold will not show up in the SCORE image.

object that resides inside the area of the subcell. In our case we choose the height and width equal to 1 µm. This partitioning of the camera images allows us to process each subcell individually and in parallel.

Figure 7.5 shows the typical results for one of the subcells. In panel a the average intensity from all measurements is plotted. The resolution in this image is limited by the conventional optics behind the HIRES-lens. Now we integrate the intensity in the subcell for each displacement of the speckle pattern to find the two dimensional function $I(\Delta x, \Delta y)$, which is plotted in panel b. This function seems completely random but contains lots of information about the original object. This information becomes visible once we calculate the autocorrelation of $I(\Delta x, \Delta y)$. In panel c, where the autocorrelation is plotted, three bright dots are visible together with some low intensity structures around them. By averaging over data from 4 individual scans this background noise is reduced. Subsequently we employ the phase retrieval algorithms that were discussed in section 7.3. The low resolution image was used as a first guess in the algorithms and is later used to find the absolute position and orientation of the inversion result, which is shown in panel d. The image clearly shows two spheres that were not resolved in the original image. This result convincingly shows that the resolution of the final image is not limited by the imaging optics.

To acquire a wide field image, the aforementioned method is applied to every subcell. By using overlapping subcells, the results of each subcell can be joined together to yield a larger high resolution image. In Fig. 7.6 the result of this 'stitching' process is plotted (b) together with the standard resolution image (a). The image in panel b is composed out of 4000 subcells to yield a image of 7.0×5.2 µm^2. By taking more subcells into account the maximum size of the image is only limited by the recorded field of view on the camera, which can easily span an area of several hundreds of square micrometers.

In Fig. 7.6c we plotted two horizontal cross section taken along the white dotted lines in images a and b. From this plot the resolution increase of SCORE

is obvious. The two spheres on the right that are normally not resolvable, are clearly resolved by the use of SCORE. In the SCORE image, the spheres have a full width half max (FWHM) of 173 nm. The real diameter of the spheres is specified at 100 nm. When the optical spotsize would be in the order of 100 nm, as we measured in the previous chapter with a similar HIRES-lens, we would expect the spheres to have a FWHM of approximately 122 nm. From the fact that they appear larger in our image, we can conclude that the resolution of our system is slightly worse than the resolution reported in chapter 6.

There are a few possible reasons for the difference in resolution, which deserve further investigation. First of all, the fluorescent objects we try to image are on the same order of the expected resolution. To truly quantify the resolution, smaller objects should be imaged. The second reason might lie in the stitching of the individual subcells. Small repositioning errors introduce broadening of the image thereby degrading the resolution.

7.6 Conclusions

In this chapter we introduced a novel wide field high resolution imaging technique called Speckle Correlation Resolution Enhancement (SCORE). SCORE allows for imaging with speckle illumination and is therefore excellently suited to be used in combination with scattering lenses[7, 21–23] without the need of a reference measurement that characterizes the lens.

We experimentally demonstrated SCORE in combination with a gallium phosphide HIRES-lens to acquire wide field images of 7.0×5.2 µm^2 at high resolution of fluorescent nano spheres. The field of view is easily expanded to yield an area of several hundreds of square micrometers. The resolution is slightly worse than reported in the previous chapter with a similar HIRES-lens. The exact cause of this difference remains, for now, an open question.

Bibliography

[1] J. R. Lakowicz, *Principles of fluoresence spectroscopy, 3rd edition* (Springer, 2006). — p.85.

[2] S. W. Hell and J. Wichmann, *Breaking the diffraction resolution limit by stimulated emission: stimulated-emission-depletion fluorescence microscopy*, Opt. Lett. **19**, 780 (1994). — p.85.

[3] M. Dyba and S. W. Hell, *Focal spots of size $\lambda/23$ open up far-field florescence microscopy at 33 nm axial resolution*, Phys. Rev. Lett. **88**, 163901 (2002). — p.85.

[4] E. Betzig, G. H. Patterson, R. Sougrat, O. W. Lindwasser, S. Olenych, J. S. Bonifacino, M. W. Davidson, J. Lippincott-Schwartz, and H. F. Hess, *Imaging Intracellular Fluorescent Proteins at Nanometer Resolution*, Science **313**, 1642 (2006). — p.85.

[5] M. J. Rust, M. Bates, and X. Zhuang, *Sub-diffraction-limit imaging by stochastic optical reconstruction microscopy (storm)*, Nat. Meth. **3**, 793 (2006). — p.85.

[6] S. W. Hell, *Far-Field Optical Nanoscopy*, Science **316**, 1153 (2007). — p.85.

[7] E. G. van Putten, D. Akbulut, J. Bertolotti, W. L. Vos, A. Lagendijk, and A. P. Mosk, *Scattering lens resolves sub-100 nm structures with visible light*, Phys. Rev. Lett. **106**, 193905 (2011). — p.85, 96.

[8] S. Feng, C. Kane, P. A. Lee, and A. D. Stone, *Correlations and fluctuations of coherent wave transmission through disordered media*, Phys. Rev. Lett. **61**, 834 (1988). — p.86.

[9] I. Freund, M. Rosenbluh, and S. Feng, *Memory effects in propagation of optical waves through disordered media*, Phys. Rev. Lett. **61**, 2328 (1988). — p.86.

[10] A. Papoulis, *The fourier integral and its applications* (New York: McGraw-Hill, 1962). — p.87, 91.

[11] J. Goodman, *Statistical optics* (Wiley, New York, 2000). — p.88.

[12] R. H. T. Bates, *Fourier phase problems are uniquely solvable in more than one dimension. i: underlying theory*, Optik **61**, 247 (1982). — p.91.

[13] R. H. T. Bates, *Uniqueness of solutions to two-dimensional fourier phase problems for localized and positive images*, Computer Vision, Graphics, and Image Processing **25**, 205 (1984). — p.91.

[14] R. Barakat and G. Newsam, *Necessary conditions for a unique solution to two-dimensional phase recovery*, Journal of Mathematical Physics **25**, 3190 (1984). — p.91.

[15] J. R. Fienup, *Reconstruction of an object from the modulus of its fourier transform*, Opt. Lett. **3**, 27 (1978). — p.91.

[16] J. R. Fienup, *Phase retrieval algorithms: a comparison*, Appl. Opt. **21**, 2758 (1982). — p.91.

[17] J. W. Goodman, *Speckle phenomena in optics* (Roberts & Company, Englewood, 2006). — p.91.

[18] J. Miao, P. Charalambous, J. Kirz, and D. Sayre, *Extending the methodology of x-ray crystallography to allow imaging of micrometre-sized non-crystalline specimens*, Nature **400**, 342 (1999). — p.91.

[19] B. Abbey *et al.*, *Lensless imaging using broadband x-ray sources*, Nat. Photon. **5**, 420 (2011). — p.91.

[20] R. P. Millane, *Phase retrieval in crystallography and optics*, J. Opt. Soc. Am. A **7**, 394 (1990). — p.91.

[21] I. M. Vellekoop and A. P. Mosk, *Focusing coherent light through opaque strongly scattering media*, Opt. Lett. **32**, 2309 (2007). — p.96.

[22] S. Popoff, G. Lerosey, M. Fink, A. C. Boccara, and S. Gigan, *Image transmission through an opaque material*, Nat. Commun. **1**, 81 (2010). — p.96.

[23] Y. Choi, T. D. Yang, C. Fang-Yen, P. Kang, K. J. Lee, R. R. Dasari, M. S. Feld, and W. Choi, *Overcoming the diffraction limit using multiple light scattering in a highly disordered medium*, Phys. Rev. Lett. **107**, 023902 (2011). — p.96.

CHAPTER 8
Reference Free Imaging Through Opaque Layers

8.1 Introduction

Optical scattering dominates over absorption in many materials of technological and medical relevance. Examples include paints, paper, and ceramics, as well as teeth, bone, and tissue. Scattering is what makes these materials opaque because light is not able to propagate freely but changes direction at each scattering event. Especially in imaging, scattering is experienced as a nuisance that strongly limits the use of conventional optical methods to depths of about one mean free path.

Driven by the great relevance to biomedical imaging, transportation safety, and detection of concealed weapons, several optical techniques have been developed to improve imaging in turbid materials.[1] Gated imaging methods, such as optical coherence tomography, quantum coherence tomography[2], time gated imaging[3], and polarization gated imaging[4] use the small amount of unscattered (ballistic) light to improve the imaging depth. As the fraction of ballistic light exponentially decreases with increasing depth, these techniques are limited to a few mean free paths.

More recently, the use of scattered light for imaging has gained increasing interest. Advances in technology now enable a precise characterization of the light propagation through disordered scattering materials[5, 6]. With such information at hand, it becomes possible to detect objects that are later placed behind them[7–9] or manipulate the light to form a scanning probe[10, 11]. While many news reporters[12–15] saw these experiments as a proof of 'See-Through vision', the necessity of a reference measurement that requires optical access behind the opaque material defies the purpose of the application.

True see-through vision should not require any physical access to the object but should place the observer only on the other side of the screen that separates him or her from the object. To achieve the first true reference measurement free imaging through opaque materials, we propose the setup that is sketched in Fig. 8.1. A fluorescent object is placed at some distance behind an opaque layer. The scattering in the layer makes it impossible to see the object. By illuminating the layer with a coherent beam of light, speckles are formed at random positions behind it. The optical memory effect allows the speckles to be translated by tilting the incident beam. The speckled intensity pattern will illuminate different (and unknown) positions of the object simultaneously. The fluorescent emission coming from the illuminated regions cannot be resolved because the scattering layer is blocking the view. The only measurable quantity is the amount of flu-

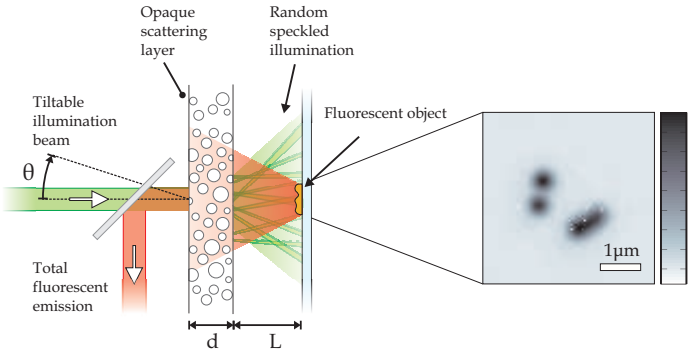

Figure 8.1: Proposed setup for reference free imaging through opaque layers. A tiltable coherent beam is projected onto an opaque scattering layer and creates a speckled illumination pattern behind the layer. These speckles can be moved across a fluorescent object, which is hidden behind the layer. From the front of the opaque layer total emitted fluorescence is measurable. This information turns out to be enough to recover the shape of the original object. Due to fabrication limitations, we are currently forced to use a bucket-detector at the back of the sample to monitor the total amount of emitted light. The inset shows a recorded image of the object.

orescent intensity that diffuses through the layer, which is proportional to the total amount of emitted fluorescence. As we will show, this information is enough to recover the spatial information of the object hidden behind the layer.

8.2 Theory

The amount of fluorescent emission I that is detected from the front side of the layer is proportional to the overlap between the object and the speckle intensity

$$\begin{aligned} I(\Delta\mathbf{r}) &= \int_{-\infty}^{\infty} O(\mathbf{r}) S(\mathbf{r} - \Delta\mathbf{r})\, d^2\mathbf{r} \\ &= [O * S(-\mathbf{r})]\,(\Delta\mathbf{r}), \end{aligned} \tag{8.1}$$

where $*$ denotes a convolution product, $\mathbf{r}$ a position (x, y) in the plane of the object, and $\Delta\mathbf{r}$ the position of the speckle pattern S relative to the object O. It is readily shown (see Eq. 7.5) that the autocorrelation of I is equal to the autocorrelation of the object convoluted with a sharply peaked function given by the autocorrelation ($\star$) of the random speckle pattern

$$[I \star I]\,(\delta\mathbf{r}) = [(O \star O) * (S \star S)]\,(\delta\mathbf{r}) \tag{8.2}$$

The exact shape of $S \star S$ depends strongly on the illumination and several geometrical parameters. We calculated this term in the previous chapter for a circular beam with width W illuminating an opaque slab with a thickness d (see

Eqs. 7.11 and 7.14). At a distance L behind the slab we found

$$[I \star I](\delta\mathbf{r}) = \left[[O \star O](\Delta\mathbf{r}) * \left[\frac{2J_1(k_{\max}\ |\Delta\mathbf{r}|)}{k_{\max}\ |\Delta\mathbf{r}|} \right]^2 \right](\delta\mathbf{r}) \times \left[\frac{|\delta\mathbf{r}|\ kd/L}{\sinh|\delta\mathbf{r}|\ kd/L} \right]^2, \tag{8.3}$$

where J_1 is a Bessel function of the first kind and $k_{\max}$ is the highest transversal wave vector that reaches the object given by $k\sin(\arctan(W/2L))$, with $k = 2\pi/\lambda$. The term that contains the Bessel function is equal to the average speckle shape and determines the resolution at which the objects autocorrelation is retrieved. The achievable resolution is increased by just illuminating a wider part of the scattering layer. The last term accounts for the limited range over which the speckles hold their correlation during a translation by the optical memory effect.

When the width W of the illumination spot is larger than the thickness d of the scattering layer, it is possible to resolve the autocorrelation $O \star O$ of an object with a maximum width of L/kd. This information about the object can be retrieved just from the fluorescent intensity that diffuses through the layer.

Once the autocorrelation is found, the original object is uniquely[16–18] retrieved with iterative algorithms[19, 20] described in section 7.3, combined with the trivial constraint that the object should be real and positive. We first used the 'Hybrid Input-Output' algorithm with the feedback parameter β ranging from 2 to 0 in steps of 0.1. For each value of β the algorithm runs 100 iterations. Finally, 1000 iterations with the 'Error-Reduction' algorithm are used to arrive at the final result.

The retrieval algorithms require a starting guess, for which we use a completely unbiased random pattern that has no information about the object. We found that for approximately 70% of the random starting guesses, the algorithm converged in a reasonable amount of iterations to the correct image. By monitoring the difference between the measured autocorrelation and the autocorrelation of the retrieved image, we can clearly discriminate these successful cases in which the algorithm converged to the correct solution from the unsuccessful attempts. There exist furthermore several approaches to overcome the stagnation of the algorithm[21] that are encountered in the unsuccessful attempts.

8.3 Experimental details

The experimental apparatus is conceptually straightforward. A two dimensional scan mirror is employed to carefully change the angle of incidence of a continuous wave laser beam ($\lambda = 561$ nm), which is projected onto an opaque layer of disordered zinc oxide (ZnO) pigment. The ZnO layer has a thickness of $d = 10$ µm and a transport mean free path of $\ell = 0.6$ µm, which makes the layer optically thick so that there are no transmitted ballistic photons. It is therefore impossible to resolve any object that is placed behind the scattering layer. A substrate with

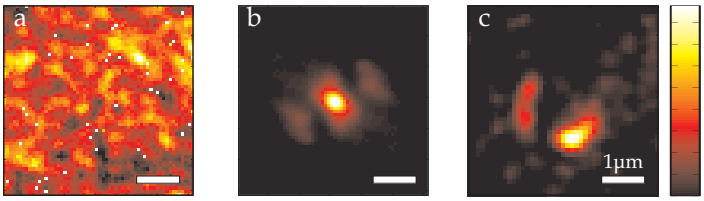

Figure 8.2: Experimental results. **a:** Total fluorescent emission I as function of the speckle pattern's position. The random white pixels arise from an artifact of the used detector. **b:** Autocorrelation of I averaged over 4 scans with different speckle patterns. **c:** Image retrieved from the autocorrelation in panel b. The scale bars represent 1 µm.

a thickness $L = 160$ µm supports the ZnO layer. At the back of this substrate a random configuration of dye doped fluorescent spheres (Thermo Scientific, R100) with a diameter of 100 nm is placed.

Due to the limited angular range of the optical memory effect, the imaging method requires a flurescent object with limited support. The upper limit is given by the last term in Eq. 8.3, which goes exponentially to zero for distances $\delta\mathbf{r}$ larger than L/kd. The geometry of our sample determines that the objects therefore have to be in a circular area with a diameter of approximately 2 µm. Any other object areas should be placed at a distance far enough so that its emission from each area can be resolved separately through the scattering layer.

With our present sample fabrication method we cannot achieve such a selective deposition of fluorescent objects. For that reason we placed our detector at the back of the sample and used an iris to spatially filter the fluorescence of a single area. The detector is a sensitive EMCCD camera that is used as a pure bucket-detector; no spatial information is used what so ever, only the total amount of emission that is detected. There is in principle no difference between this signal and the signal that would be detected from the front of the sample because both are proportional to the total emitted fluorescence from the area under study.

8.4 Results

The results of the measurement are plotted in Fig. 8.2. In the first panel (a) we see the fluorescent intensity I as function of the speckle pattern's position. The intensity is corrected for any bleaching during the scan. The second panel (b) shows the autocorrelation of I averaged over 4 individual scans. From this autocorrelation we retrieved the image shown in the third panel (c). This retrieved image shows a good correspondence with the original object that is seen in Fig. 8.1.

In the retrieved image, there are some spatial intensity fluctuations that are not visible in the reference image. These fluctuations are likely to be caused by an incomplete averaging of the autocorrelation. By scanning the object with more speckle patterns, a better averaging of the autocorrelation is feasible.

8.5 Conclusions

We demonstrated a proof of principle for a reference measurement free imaging technique capable of reconstructing a fluorescent object that is hidden behind a completely opaque scattering layer. The random nature of speckle patterns was exploited to retrieve the autocorrelation of the object by scanning the speckles over the object. With the use of iterative phase retrieval algorithms, the original object was reconstructed at high quality. The resolution of the reconstructed object can be made arbitrarily close to the diffraction limit by illuminating a wider area of the opaque layer. The field of view is given by the optical memory range.

For now, challenges in the sample fabrication enforced us to use a bucket-detector at the back of the sample. Conceptually we are measuring the same quantity as one would measure in front of the opaque layer. The results presented in this chapter therefore convincingly proved the working of the proposed technique and provide an important step towards true 'See-Through vision'.

While the technique was demonstrated to work with two dimensional fluorescent objects, it is certainly not limited to such samples. Any signal that depends on the speckle intensity, such as Raman scattering, second harmonic generation, or even absorption, could be used to retrieve the object. Furthermore, by adding a parabolic phase pattern to the incident beam, the speckles can also be translated into the third direction allowing for three dimensional imaging through opaque materials.

The possibility to optically image through opaque materials promises exciting applications in various fields including biological imaging. One could think for example of studying intravascular biological processes, possibly combined with endoscopy, in a extravascular way. In several other imaging areas, our method could possibly replace X-rays with safer optical photons. From the information we gain with our technique it should be feasible to reconstruct the shape of the random speckle patterns. Combining this information with spatial wave front shaping[5], light could then be directed to specific regions of the imaged object, which is highly relevant to photodynamic therapy[22].

Bibliography

[1] P. Sebbah, *Waves and imaging through complex media* (Kluwer Academic Publishers, 1999). — p.99.

[2] M. B. Nasr, B. E. A. Saleh, A. V. Sergienko, and M. C. Teich, *Demonstration of dispersion-canceled quantum-optical coherence tomography*, Phys. Rev. Lett. **91**, 083601 (2003). — p.99.

[3] N. Abramson, *Light-in-flight recording by holography*, Opt. Lett. **3**, 121 (1978). — p.99.

[4] S. Mujumdar and H. Ramachandran, *Imaging through turbid media using polarization modulation: dependence on scattering anisotropy*, Optics Communications **241**, 1 (2004). — p.99.

[5] I. M. Vellekoop and A. P. Mosk, *Focusing coherent light through opaque strongly scattering media*, Opt. Lett. **32**, 2309 (2007). — p.99, 103.

[6] S. M. Popoff, G. Lerosey, R. Carminati, M. Fink, A. C. Boccara, and S. Gigan, *Measuring the transmission matrix in optics: An approach to the study and control of light propagation in disordered media*, Phys. Rev. Lett. **104**, 100601 (2010). — p.99.

[7] Z. Yaqoob, D. Psaltis, M. S. Feld, and C. Yang, *Optical phase conjugation for turbidity suppression in biological samples*, Nat. Photon. **2**, 110 (2008). — p.99.

[8] S. Popoff, G. Lerosey, M. Fink, A. C. Boccara, and S. Gigan, *Image transmission through an opaque material*, Nat. Commun. **1**, 81 (2010). — p.99.

[9] Y. Choi, T. D. Yang, C. Fang-Yen, P. Kang, K. J. Lee, R. R. Dasari, M. S. Feld, and W. Choi, *Overcoming the diffraction limit using multiple light scattering in a highly disordered medium*, Phys. Rev. Lett. **107**, 023902 (2011). — p.99.

[10] I. Vellekoop and C. Aegerter, *Scattered light fluorescence microscopy: imaging through turbid layers*, Opt. Lett. **35**, 1245 (2010). — p.99.

[11] C.-L. Hsieh, Y. Pu, R. Grange, G. Laporte, and D. Psaltis, *Imaging through turbid layers by scanning the phase conjugated second harmonic radiation from a nanoparticle*, Opt. Express **18**, 20723 (2010). — p.99.

[12] C. Barras, 'Superman' vision penetrates opaque glass, `http://www.newscientist.com/article/dn18445-superman-vision-penetrates-opaque-glass.html`, 2010. — p.99.

[13] C. Choi, See-Through Vision Invented, `http://news.nationalgeographic.com/news/2010/03/100310-see-through-vision-opaque-scitech-physical/`, 2010. — p.99.

[14] Editorial, *See through tissue*, Nature **465**, 12 (2010). — p.99.

[15] M. Campbell, Why skin is a better lens than glass, `http://www.newscientist.com/article/mg21128193.800-why-skin-is-a-better-lens-than-glass.html`, 2011. — p.99.

[16] R. H. T. Bates, *Fourier phase problems are uniquely solvable in more than one dimension. i: underlying theory*, Optik **61**, 247 (1982). — p.101.

[17] R. H. T. Bates, *Uniqueness of solutions to two-dimensional fourier phase problems for localized and positive images*, Computer Vision, Graphics, and Image Processing **25**, 205 (1984). — p.101.

[18] R. Barakat and G. Newsam, *Necessary conditions for a unique solution to two-dimensional phase recovery*, Journal of Mathematical Physics **25**, 3190 (1984). — p.101.

[19] J. R. Fienup, *Reconstruction of an object from the modulus of its fourier transform*, Opt. Lett. **3**, 27 (1978). — p.101.

[20] J. R. Fienup, *Phase retrieval algorithms: a comparison*, Appl. Opt. **21**, 2758 (1982). — p.101.

[21] J. R. Fienup and C. C. Wackerman, *Phase-retrieval stagnation problems and solutions*, J. Opt. Soc. Am. A **3**, 1897 (1986). — p.101.

[22] T. J. Dougherty, C. J. Gomer, B. W. Henderson, G. Jori, D. Kessel, M. Korbelik, J. Moan, and Q. Peng, *Photodynamic therapy*, Journal of the National Cancer Institute **90**, 889 (1998). — p.103.

Algemene Nederlandse samenvatting

Licht is essentieel voor vele chemische, biologische en fysische processen en het belang van licht voor de mensheid weerspiegelt zich in eeuwenoude en uitgebreide inspanningen om het ontstaan en voortplanting ervan te beheersen. Waar oude beschavingen met water gevulde glazen en gepolijste metalen gebruikten om licht van de zon en van vuur te manipuleren, zijn lenzen en spiegels van zeer hoge kwaliteit tegenwoordig gemeengoed. Deze optische componenten stellen ons in staat om met nanometer precisie afstanden te meten, objecten af te beelden over een immens bereik van lengteschalen - van cellen tot sterren - en wereldwijd te communiceren met de snelheid van licht. Wellicht de meest aansprekende toepassing van licht is haar vermogen om ruimtelijke informatie over te brengen.

Afbeelden met lenzen

Een object dat belicht wordt zal, afhankelijk van de lokale samenstelling, licht reflecteren, absorberen, verstrooien of uitzenden. Deze interactie codeert informatie over het object in het licht. Door dit licht op een andere positie weer op te vangen en op de juiste manier te sturen ontstaat een afbeelding van het originele object. Onze ogen kunnen licht op precies deze juiste manier sturen en stellen ons daarmee in staat de wereld om ons heen te zien.

Hoewel we dagelijks van de kleurrijke wereld genieten, zijn onze ogen toch sterk

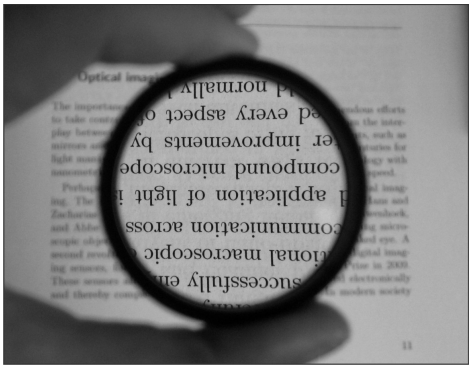

Figuur 1: Het manuscript van dit proefschrift afgebeeld met een positieve lens. Op het moment dat u naar deze figuur kijkt, zullen uw ogen voor een scherpe afbeelding op uw netvlies zorgen.

Figuur 2: Een foto afgebeeld op drie verschillende resoluties. Door de resolutie te verhogen worden steeds meer details van de foto zichtbaar.

gelimiteerd in wat ze kunnen zien. Zo kunnen we de dikte van een haar nog net onderscheiden, maar we zijn niet in staat om de individuele cellen te zien die haar vormen. Lenzen kunnen hier gebruikt worden om onze ogen te helpen; bekende voorbeelden zijn brillenglazen en contactlenzen.

Lenzen vervormen licht op een welbepaalde manier die gegeven wordt door zijn vorm en de brekingsindex van het gebruikte materiaal. Zo zal een positieve lens een evenwijdige lichtbundel focusseren tot een kleine vlek in zijn brandpunt. De kleinste lichtvlek die een lens kan creëren is gelijk aan de kleinste structuur die je met die lens kan zien; de optische resolutie. Door de resolutie te verhogen worden fijne structuren zichtbaar die daarvoor onzichtbaar waren. Dit effect is goed zichtbaar in Figuur 2 waar dezelfde foto op drie verschillende resoluties is afgebeeld. De tekst die op de linker afbeelding nog onleesbaar is, is op een hogere resolutie prima leesbaar.

De optische resolutie wordt bepaald door de golflengte van het gebruikte licht en de hoeken waaronder dit licht door de lenzen opgevangen kan worden. Hoe kleiner de golflengte en hoe groter de ruimtehoek, hoe beter de resolutie. In microscopen, waar met hoge resolutie kleine structuren worden onderzocht, gebruikt men gecompliceerde lenzenstelsels om licht onder een zo groot mogelijke hoek op te vangen. Door de ruimte tussen het object en de lens op te vullen met een materiaal dat een hoge brekingsindex heeft, zoals olie of water, kan de resolutie vervolgens nog verder worden vergroot. Dit komt omdat licht zich in zo'n materiaal langzamer voortplant waardoor de golflengte effectief kleiner wordt (zie Figuur 3).

Een perfect werkend optisch afbeeldingssysteem wordt alleen nog door diffractie gelimiteerd; door golfeigenschappen van licht is de kleinst mogelijke lichtspot gelijk aan ongeveer een halve golflengte. Voor zichtbaar licht ligt deze limiet op ongeveer 200 nm, zo'n 400 keer kleiner dan de dikte van een menselijke haar.

Licht verstrooiing

In de praktijk zorgen imperfecties in de lenzen er voor dat de diffractielimiet erg lastig te behalen valt. Imperfecties verstrooien licht in een willekeurige richting en

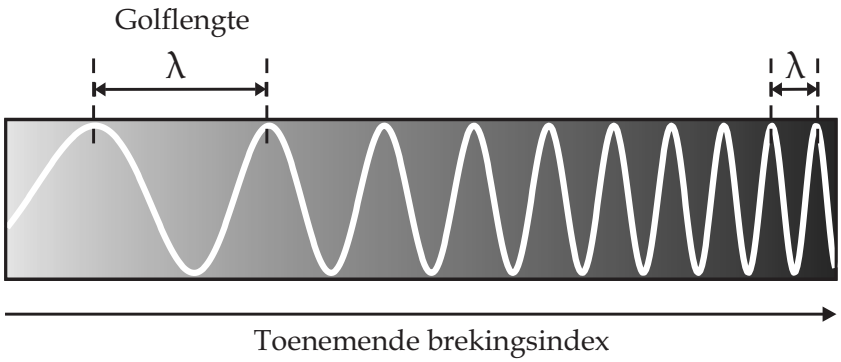

Figuur 3: De brekingsindex bepaalt hoe snel licht zich voortplant door een materiaal. Onafhankelijk van haar snelheid zal licht met dezelfde frequentie blijven trillen. Wanneer de brekingsindex groter wordt, zal licht langzamer gaan en zal haar golflengte daardoor korter worden.

verslechteren daarmee de resolutie van het systeem. Iedereen weet uit ervaring dat het zicht op een mistige dag significant slechter is. Dit komt doordat het licht meerdere malen verstrooid wordt door kleine waterdeeltjes in de lucht. Als licht vele malen wanordelijk verstrooit, lijkt het onmogelijk om nog iets over zijn oorspronkelijke positie te zeggen.

In je directe omgeving zijn tal van voorbeelden te vinden waar wanordelijke verstrooiing van licht ervoor zorgt dat objecten verborgen blijven. Denk hierbij aan een laag witte verf die een betonnen muur verbergt of je huid waarin licht voornamelijk heen en weer kaatst. Het mag duidelijk zijn dat voor vele medische en technologische toepassingen het van enorm belang is om door zulke ondoorzichtige materialen heen te kunnen kijken.

Indien we echter lichtbronnen gebruiken met een hoge coherentie, zoals een laser, valt er heel wat te leren over objecten die verborgen worden door verstrooiende lagen. Licht van deze bronnen behoudt haar coherentie zelfs na meer dan duizenden botsingen. Hierdoor zal het licht ook achter de verstrooiende laag nog interfereren. Het licht neemt echter veel verschillende paden door het materiaal waarbij ieder pad een andere lengte heeft. Als resultaat zal licht op sommige punten constructief interfereren en op andere destructief zodat er een zogeheten wanordelijk spikkelpatroon ontstaat wat de verborgen objecten belicht. En hoewel deze interferentie nog niet direct tot een afbeelding leidt, blijkt het wel de sleutel te zijn tot verstrooiende lenzen.

Verstrooiende lenzen

Op het eerste gezicht lijken ondoorzichtige verstrooiende materialen, zoals papier, verf of huid, compleet verschillend van heldere en zorgvuldig gepolijste lenzen. In wanordelijke materialen lijkt alle informatie verloren te gaan door verstrooiing. Het feit dat licht nog steeds interfereert wanneer het het materiaal verlaat laat

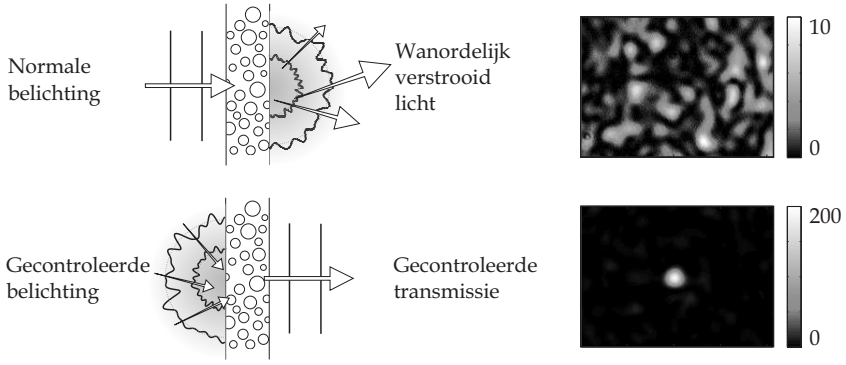

Figuur 4: Een wanordelijke ondoorzichtige laag verstrooit licht in willekeurige richtingen. Wanneer zo'n laag belicht wordt door een laser bundel, zal het doorgelaten een wanordelijk spikkelpatroon vormen. Door de belichting op de juiste wijze aan te passen, kan het verstrooide licht worden gecontroleerd. Het is nu mogelijk om een scherp focus te creëren achter de ondoorzichtige laag, die daardoor als verstrooiende lens fungeert.

echter zien dat het licht alleen flink door elkaar wordt geschud maar dat informatie behouden blijft.

In onze groep hebben we een techniek ontwikkeld die precies kan meten op welke manier het licht door een wanordelijk materiaal gemixt wordt. Met deze informatie bij de hand kan de belichting zo worden aangepast dat het verstrooide licht precies op een gecontroleerd punt bij elkaar komt, net zoals bij een normale lens. Figuur 4 laat dit principe zien. Onder normale belichting zal licht verstrooid worden en ontstaat er een wanordelijk spikkelpatroon. Wanneer de belichting op de juiste manier aangepast wordt, kan het verstrooide licht gecontroleerd worden. Het is nu bijvoorbeeld mogelijk om een scherp focus te maken achter of zelfs in de ondoorzichtige laag (Hoofdstuk 4). De intensiteit in het focus van een verstrooiende lens is erg gevoelig voor verplaatsing van de verstrooiende laag. Dit maakt deze lenzen tevens zeer geschikt voor nauwkeurige optische positiebepaling zoals we in Hoofdstuk 5 laten zien.

Afbeelden met verstrooiende lenzen

In Hoofdstuk 6 laten we zien dat verstrooiing van licht niet noodzakelijk hoeft te leiden tot een verlies van resolutie maar dat we het zelfs kunnen uitbuiten om de resolutie enorm te verbeteren. Zo hebben we verstrooiende lenzen ontwikkeld uit een materiaal met een zeer hoge brekingsindex. Deze verstrooiende lenzen hebben daardoor een ongekende resolutie die veel beter is dan zelfs de beste commerciële lenzen. Zowel nationaal (o.a. NRC Handelsblad) als internationaal (o.a. Science, Nature Nanotechnology en Wired) heeft deze lens veel belangstelling gewekt.

Hoewel deze lens een zeer hoge resolutie bereikt, is zijn beeldveld beperkt. Om

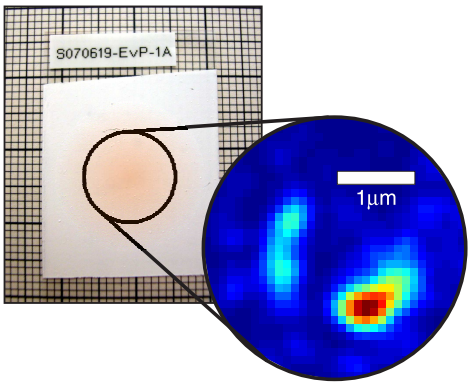

Figuur 5: Een laag witte verf verbergt een groepje fluorescerende bollen. Aan de voorkant van de verflaag kunnen we alleen de totale hoeveelheid uitgezonden licht van de bollen bepalen. Door de verf op een speciale manier met een laser te belichten kunnen we de oorspronkelijke configuratie van de bollen echter achterhalen en een afbeelding maken dwars door de ondoorzichtige laag heen.

de lens ook over een wijd beeldveld te kunnen gebruiken hebben we een nieuwe afbeeldingsmethode bedacht die direct gebruik maakt van spikkelbelichting. We laten theoretisch en experimenteel zien dat deze methode, gecombineerd met de hogeresolutie verstrooiende lens, in staat is om structuren op hoge resolutie af te beelden over een groot beeldveld. Deze resultaten staan beschreven in Hoofdstuk 7.

De ontwikkelde afbeeldingstechniek voor spikkelbelichting kan naast microscopie ook worden gebruikt in een andere configuratie, welke geschetst staat in Figuur 5. In deze geometrie worden fluorescerende objecten verborgen door een laag witte verf. Door een laser bundel op de verflaag te schijnen zal een wanordelijk spikkelpatroon de fluorescente objecten belichten. Aan de voorkant van de verflaag kunnen we alleen de totale hoeveelheid uitgezonden licht van de bollen bepalen. Maar dit blijkt genoeg te zijn om de oorspronkelijke configuratie van de bollen te achterhalen en een afbeelding te maken dwars door de ondoorzichtige laag heen. Deze techniek is de eerste optische methode die door een materiaal heen kan kijken zonder dat het enige toegang nodig heeft tot de ruimte achter het materiaal. In Hoofdstuk 8 hebben we experimenteel laten zien dat deze techniek werkt.

Dankwoord

Dit proefschrift geldt als een geschreven afsluiting van mijn promotie traject. En hoewel mijn naam op de voorkant staat, hebben vele mensen een onmisbare bijdrage geleverd aan het resultaat. Ik ben hen stuk voor stuk zeer dankbaar en dit hoofdstuk, wat compleet gewijd is aan deze personen, is daarom wellicht het belangrijkste deel van dit proefschrift.

Als eerste wil ik mijn begeleiders Allard en Ad bedanken. Allard, je briljante ideeën, ongekend brede kennis en je aanstekelijke enthousiasme hebben in hoge mate bijgedragen aan dit mooie eindresultaat. Ad, je hebt me veel inzicht gegeven in hoe de (wetenschappelijke) wereld werkt. Ik heb me vaak verbaasd over de ongekende snelheid waarmee je problemen analyseert om me vervolgens vanuit een heel ander perspectief naar het vraagstuk te laten kijken. Het was iedere keer weer een groot plezier om naar AMOLF te gaan.

Willem, als groepsleider van Complex Photonic Systems heb jij een grote stempel gedrukt op mijn promotie. Ik bewonder je gedrevenheid, inzicht en je oprechte streven om het beste uit je mensen te halen. Je komst naar Twente en de bijbehorende groei van de groep heb ik zeer gewaardeerd. Verder wil ik je bedanken dat je lid wil zijn van mijn promotie commissie. I also greatly acknowledge the other committee members, professors Kobus Kuipers, Carlo Beenakker, and Vahid Sandoghdar for taking the time to carefully read the manuscript of my thesis.

Mijn promotie bouwt voort op eerder onderzoek uit onze groep. Ivo, zonder jouw geweldige werk waren de experimenten in dit proefschrift niet mogelijk geweest. Ik heb veel van je geleerd en heb onze samenwerking altijd erg op prijs gesteld. At this point I would also like to acknowledge Jacopo for his great scientific insights and ideas that were indispensable for particularly the results of chapters 7 and 8. With great pleasure I look back at the intense daily discussions we had during the development of the required theory and in a later stage the actual experiments.

De omvang van onze onderzoeksgroep vertoonde de afgelopen jaren sterke fluctuaties. Het vertrek van vele gewaardeerde collega's zoals Tijmen, Philip, Danang, Alex, Rajesh, Bart, Bernard, Karen, Ivan, Raymond, Tom, Willem, Léon, Wouter, Merel, Frerik, Edwin en Niels, werd gecompenseerd door de komst van nieuwe collega's waaronder Pepijn, Duygu, Hasan, Elahe, Jacopo, Simon[1], Emre, Naser, Bas, Georgios, Rob, Marcel, Thomas en Kurt in Twente en Sanli, Ramy, Patrick, Paolo, Ronald, Bergin en Jochen in Amsterdam. I would like to thank you all for the incredibly inspiring and motivating atmosphere combined

[1] Bedankt voor het solderen.

with the heated discussions that pushes our research to a higher level. In het bijzonder wil ik Frerik bedanken. Het was enorm leuk om je te mogen begeleiden en ik heb veel van je geleerd.

Onze groep heeft de afgelopen jaren de uitmuntende ondersteuning mogen genieten van Karen, Marscha, Nilda, Bas, Marlon, Charles, Robin, Cock en Hannie. Ik wil jullie bedanken voor jullie gezelligheid en alle hulp tijdens de afgelopen jaren. Cock, bedankt voor je talloze inventieve technische oplossingen en je bijdrage aan de cohesie van de groep. Het was een groot plezier om een kamer met je te delen. Hannie, je opgewekte humeur fleurde de groep behoorlijk op. Verder bracht je de hoognodige chemische kennis met je mee die onder natuurkundigen nog wel eens ontbreekt.

Ieder promotie traject kent zijn pieken en dalen. Het is daarom geweldig om terug te kunnen vallen op dierbare vrienden die het belang van een promotie weten te relativeren. De weekenden weg met 'de Mannen' Henk, Sjoerd, Rogier, Renee, Laurens, Michael, Roy, en Aart, maar ook de vele feesten met Tara, Shannon, Jeanine, Sandra, Julie, Nicole en Elize brachten de hoognodige ontspanning. Ik koester de vele leuke momenten die we hebben beleefd en kijk uit naar degene die nog komen. In Enschede stonden Erik, Koen en Christian altijd klaar en ik zal de gezellige avonden met jullie niet snel vergeten. Verder wil ik Rogier en Henk in het bijzonder bedanken voor de dappere toezegging mij bij te willen staan als paranimf tijdens de verdediging (ik neem aan dat jullie het proefschrift inmiddels uit het hoofd hebben geleerd).

Naast vrienden is familie minstens zo belangrijk. Ik bedank mijn ouders, Henri, Elles en Marco voor hun steun en interesse in mijn werk, ongeacht welke kant ik ook op ging. Ook bedank ik Gerrit, Lida, Danny en Niels die ik na al die jaren alvast als mijn familie ben gaan beschouwen.

Ten slotte bedank ik de bijzonderste vrouw in mijn leven. Lieve Vera, het is niet in woorden uit te drukken hoeveel je voor me betekent. Zonder jouw onvoorwaardelijke steun en liefde waren we niet zover gekomen. Bedankt dat je er iedere dag weer voor me bent. Samen gaan we op weg naar ons volgende avontuur.

- Elbert